**DESIGN OF V-BAND BEAM-SWITCHING SUBSTRATE INTEGRATED WAVEGUIDE FED APERTURE COUPLED MICROSTRIP PATCH ARRAYS WITH BEAM-SWITCHING CAPABILITIES FOR OFF-BODY COMMUNICATIONS IN BODY CENTRIC WIRELESS NETWORKS.** By:

Carlos A. Mulero Hernández

A Thesis Submitted in Partial Fulfillment of the Requirements for the Degree of:

MASTER OF SCIENCE

In

Electrical Engineering

UNIVERSITY OF PUERTO RICO
MAYAGUEZ CAMPUS

July 2016,

Approved By:

_____________________________ _____________
José G. Colom-Ustariz, Ph.D Date
Member, Graduate Committee

_____________________________ _____________
Dejan S. Filipovic, Ph.D Date
Member, Graduate Committee

_____________________________ _____________
Rafael Rodríguez Solís, Ph.D Date
President, Graduate Committee

_____________________________ _____________
Omar Colon Reyes, Ph.D Date
Representative, Graduate School

_____________________________ _____________
José G. Colom-Ustariz, Ph.D Date
Director, Electrical and Computer Engineering Department

Abstract of Thesis Presented to the Graduate School
Of the University of Puerto Rico in Partial Fulfillment of the
Requirements for the Degree of Master of Science

**DESIGN OF V-BAND BEAM-SWITCHING SUBSTRATE INTEGRATED WAVEGUIDE FED APERTURE COUPLED MICROSTRIP PATCH ARRAYS WITH BEAM-SWITCHING CAPABILITIES FOR OFF-BODY COMMUNICATIONS IN BODY CENTRIC WIRELESS NETWORKS**

By

Carlos A. Mulero Hernández

July 2016

Chair: Rafael A. Rodríguez Solís

Major Department: Electrical and Computer Engineering

This work presents the design of a multiport, multilayer 4x4 array for use in 60 GHz body centric wireless networks. The antenna designed operates in a 14.29% -10dB bandwidth, from 56.16 to 64.8 GHz, to target the IEEE 802.11ad standard. The two versions of the presented array achieve 16.63 dBi and 15.76 dBi of gain at the center frequency.

In order to distribute power in this multiport, multilayer array, Vertical Substrate Integrated Waveguide (SIW) T-Junctions were created. These T-Junctions act as 3 dB power dividers throughout the band and are the key elements in the corporate feed. They were designed to match adjacent substrate levels for the RO4350 substrate. The thickness pairs that are matched are: 254 µm and 254 µm, 508 µm and 762 µm, and 254 µm and 508 µm. To provide a means to test the array independently, coaxial to SIW transitions were designed as well. The designed transitions allow coupling from a 1.85mm coaxial connector to 1.5mm wide, 254 µm tall SIW and 1.6mm wide, 762 µm tall SIW; both implemented in RO4350.

The effect of the human body was studied using a human body model created using the electrical parameters of skin at 60 GHz. The skin's effect was not determined to be detrimental to the antenna's intended operation.

Resumen de Tesis Presentado a Escuela Graduada
De la Universidad de Puerto Rico como requisito parcial de los
Requerimientos para el grado de Maestría en Ciencias

**DISEÑO DE ARREGLO DE PARCHO BANDA-V ACOPLADO POR APERTURA Y ALIMENTADO POR GUIA DE ONDA INTEGRADA EN EL SUSTRATO CON ABILIDADES DE RASTREO PARA APLICACIONES DE COMUNICACIÓN INALAMBRICA CENTRADA EN EL CUERPO.**

Por

Carlos A. Mulero Hernández

Julio 2016

Consejero: Rafael A. Rodríguez Solís

Departamento: Ingeniería Eléctrica y de Computadoras

Este trabajo presenta el diseño de un arreglo multipuerto 4x4 de múltiples capas para su uso en redes inalámbricas centradas en el cuerpo operando a 60 GHz. La antena diseñada opera en un ancho de banda -10 dB de 14.29%, de 56.16 a 64.8 GHz, con el fin de ser compatible con el estándar IEEE 802.11ad. Las dos versiones del arreglo presentado alcanzan 16,63 dBi y 15,76 dBi de ganancia medido a la frecuencia central.

Con el fin de distribuir el poder en este arreglo multipuerto de múltiples capas, Intersecciones-T Verticales implementadas con guía de onda integrada en sustrato (SIW por sus siglas en ingles). Estas uniones en T actúan como divisores de potencia de 3 dB en toda la banda y son los elementos clave en la alimentación paralela. Fueron diseñados para acoplar los niveles de sustrato adyacentes para el sustrato RO4350. Los pares de espesor que se corresponden son: 254 µm y 254 µm, 508 µm y 762 µm y 254 µm y 508 µm. Para medir el arreglo, transiciones de SIW a coaxial fueron diseñados. Las transiciones diseñadas permiten el acoplamiento de un conector coaxial de 1.85mm a SIW de 1.5mm de ancho con 254 µm de altura, y 1.6 mm de ancho con 762 µm de altura; tanto implementado en RO4350.

El efecto del cuerpo humano se estudió usando un modelo de cuerpo humano creado usando los parámetros eléctricos de la piel a los 60 GHz. Se determinó que el efecto de la piel no era perjudicial para la operación prevista de la antena.

# TABLE OF CONTENTS

# LIST OF TABLES

# List of Figures

# CHAPTER 1

# INTRODUCTION

Body Area Networks (BAN), also sometimes referred to as Body-Centric Wireless Communication Systems (BWCS), are networks composed of wireless devices placed on the body. The antennas used in BAN devices must be designed to cope with the different environment found in close proximity to the human body. Interactions with the human body change the antenna's electrical parameters when compared to performance in free space or air. Examples of parameters affected by the interaction between human body and antennas are the antenna's gain, input impedance, and efficiency [1].

Various countries have allocated unlicensed frequency space around 60 GHz [1]. The range of systems operating at 60 GHz is severely reduced since the atmospheric attenuation is 16 dB/km [2]. Together with the free space losses in this band, the distance for low power applications is very limited. This is less of a problem for BANs, which operate over short distances. Because of the strong attenuation, devices operating in the V-band would only receive interference from nearby devices. This allows them to more fully utilize the complete band for data transfer and provides security through better point to point isolation.

## 1.1 Objectives

The goal of this work is to design an antenna to be used for off body communications in BANs. The antenna will be designed to operate in V-band, allowing high capacity data transfer in medical, military or civilian applications, and will meet the bandwidth requirements for the IEEE 802.11ad standard. Meeting this requirement allows the antenna to be easily integrated with commercial transmitters.

## 1.2 Work Organization

This work is organized into 3 main sections. Chapter 2 will cover the literature review which explores the state of current 60 GHz array research and antennas for body area networks. Chapter 3 presents the different elements of the array along with the desing considerations and the methodology for validating the antenna against a human body model. Chapter 4 presents the results for the final 4x4 arrays as well as the results for the human body modeling. Chapter 5 concludes this work.

# CHAPTER 2

# LITERATURE REVIEW AND BACKGROUND

## 2.1 Antennas for off-body communications

There are not many studies of BANs at 60 GHz; [4], however, is a good example of a study of the effects of skin on a broad-side radiating antenna for use in off body communications. Their results are encouraging evidence for the resistance of broadside radiating antennas to the effects of the human body. In their antenna the ground plane acts as a shield which helps isolates the microstrip line and patch elements from the skin. Conversely, this also reduces the incident power density (IPD) on the skin. IPD is the dosimetric quantity that the International Commission of Nonionizing Radiation Protection limits to 20 mW/cm$^2$. The antenna shown in [4] complies with this standard at all separations from the phantom.

Effective and accurate models of human body are needed to simulate antennas on the human body. The work presented in [2] summarizes the major finds of millimeter-wave interactions with the human body. Particularly important for work in the 60 GHz band is their demonstration of incident power dissipating within the top layer of skin. This allows models to be homogeneous skin models which are simpler to design. In this work a homogeneous skin model will be used to validate a broadside radiating antenna for use in BANs.

## 2.2 60 GHz Arrays

60 GHz arrays are a very active area of research. In order to achieve longer distances, antennas working at V-Band must compensate for the increased attenuation with greater directivity. Broadside radiating arrays at millimeter wave frequencies can contain many elements while still being only a few centimeters in size. Examples of a 2x2 arrays for 60 GHz can be seen in [4], [5], and [6]. The work in [5] uses microstrip lines in order to feed a dual-

resonant slot and patch structure. Microstrip lines have a reduced efficiency at millimeter-wave frequencies and their potential for radiative losses makes them a potential detriment to the antenna's performance [7]. A technology that isolates the fields and possesses fewer losses is Substrate Integrated Waveguide (SIW) [8]. The work in [6] uses this waveguide like technology but also demonstrates one of the difficulties in developing a corporate fed array using SIW. The spacing of the elements along the E plane is greater than the spacing along the H plane causing unwanted grating lobes in the E plane.

An example of a 2x4 array is shown in [9]. The arrangement used in that work permits a more uniform spacing along both planes but their corporate feed structure occupies a very large area on the board and limits the possible arrays to $2x2^n$ element arrays. A possible way to expand this to a 4x4 array is seen in [10]. Designed for lower millimiter-wave frequencies, [10] combines parallel and series feeding structures to construct a 4x4 element array. However, the bandwidth between their single element and array changes considerably from 15% to 8.7%. [11] shows a completely corporate-fed 4x4 element array. This work uses Aperture Coupled Microstrip Patch Antennas (ACMPA) contained within a cavity. Including the cavity, the radiating element is less than 1 $cm^2$ while still containing 16 ACMPAs to achieve a gain of 18.2dBi. Their entire corporate feed network can be easily contained within a single layer because it is implemented using microstrip. The work in [7] implements a complete 1-to-16 SIW corporate feed on a single layer. Due to the limited space they had to specially design three different T-junctions that could share vias with adjacent sections of the feed network. Unlike the work in [11], each element in [7] has its own cavity. Another 4x4 element array can be seen in [12]. [12] did not squeeze the feeding network into a single layer. Instead, the first layer contains a 1-to-8 corporate power divider while the second layer uses coupling slots to create vertical T-junctions which finally feed the 16 elements in parallel. A similar feeding structure can be seen in [13] only this time it is to feed an 8x8 element array in order to achieve a higher gain. Utilizing ridge gap waveguide, the work in [14] also feeds an 8x8 element array, however their sub-elements are 2x2 elements arrays which use a coupling slot to couple between layers. This coupling is similar to [13] and [12]; however, the slot coupling in [14] is a 1-to-4 coupling.

Rectangular planar arrays are by no means the only method available to achieve the higher gains needed to combat the atmospheric attenuation at 60 GHz. Other methods found in the literature include Circular Arrays [15], Microstrip Grid Arrays [16], Multilayer Parasitic Microstrip Array [17], and Dielectric Flat Lenses [18]. This work will present a beam steerable method that will create an antenna with a Gain comparable to the work found in the literature while achieving a substantially higher effective beamwidth.

## 2.3 Rotman Lens

Introduced in the 1963 paper by W. Rotman and RF Turner [19], the Rotman lens is a passive beamforming element which introduces phase delays and amplitude tapers to achieve the desired beam forming. The lenses have been constructed in various technologies geared towards millimeter wave applications, including microstrip line [20], asymmetric double ridge waveguide [21], and SIW [22]. The SIW lens presented in [22] reports a scan angle from -40° to 40°. The angle and bandwidth within which the lens can perform is dependent on the antenna array that it is attached to along with the technology used to implement it. Because of the inclusion of dummy ports to reduce reflections that would otherwise result in undesired excitation coefficients, Rotman lenses suffer from low efficiencies. The SIW lens presented in [22] reports a maximum efficiency of 56.4% at broadside and 19.8% on its furthest off-center beam. This work seeks to develop the SIW Rotman lens at 60 GHz over a 14.29% bandwidth centered at 60.48 GHz.

# CHAPTER 3

# METHODOLOGY

## 3.1 Antenna

### 3.1.1 Antenna's Desired Operation

The antenna to be designed would operate in the 56.16 GHz to 64.8 GHz band, as specified by IEEE 802.11ad. Because it would be used for short range off-body applications the antenna is expected to count on low power inputs. Friis' equation with the atmospheric attenuation term included was used to determine the Gain required for a typical system. The logarithmic form to this equation is shown in eq. (1) [23].

$$P_r = P_t + G_t + G_r + 20log_{10}(\frac{\lambda}{4\pi R}) - \alpha R log_{10}(e) \qquad (1)$$

Solutions to this equation are shown in fig. 3.1.1.1 for different received Signal to Noise Ratios (SNR). In order to generate fig. 3.1.1.1 values were assigned to some of the variables. The power transmitted ($P_t$) was set as 0 dBm; $\alpha$ was set to -16 dB/km [2]; and $\lambda$ is 5mm, which is the wavelength at 60 GHz. It was assumed that the receiving antenna and the transmitting antenna both have the same gain ($G_t$, $G_r$). In order to detect a signal it must be possible to discern it from the undesirable background noise. For a bandwidth of 8.64 GHz the background noise power is -74.61 dBm [24]. In order to achieve a SNR of 10, 20, and 30 dB the power received ($P_r$) of eq (1) must be -64.61, -54.61, and -44.61 dBm respectively. The SNR of 0 dB is included in fig. 3.1.1.1as a reference for the theoretically ideal limit for the range($R$) at which the signal can be detected.

From fig. 3.1.1.1, with all the above conditions, it was determined that an antenna with a gain of 17dBi would suffice to cover the use cases within 100 meters. An array can be used to achieve this gain but it would have a reduced beamwidth. The reduced beamwidth would require the user more carefully aim the antenna when operating near the edge of the usable range. In order to allow a more lax aim, the array would be designed with beam-switching capabilities. This way the reduced beamwidth is offset by having the antenna scan across various angles, creating a wider effective beamwidth. For applications involving communication between users on the ground only the horizontal antenna plane needs scanning capabilities. This simplifies the vertical plane to be any configuration which behaves like a broad-side radiating array.

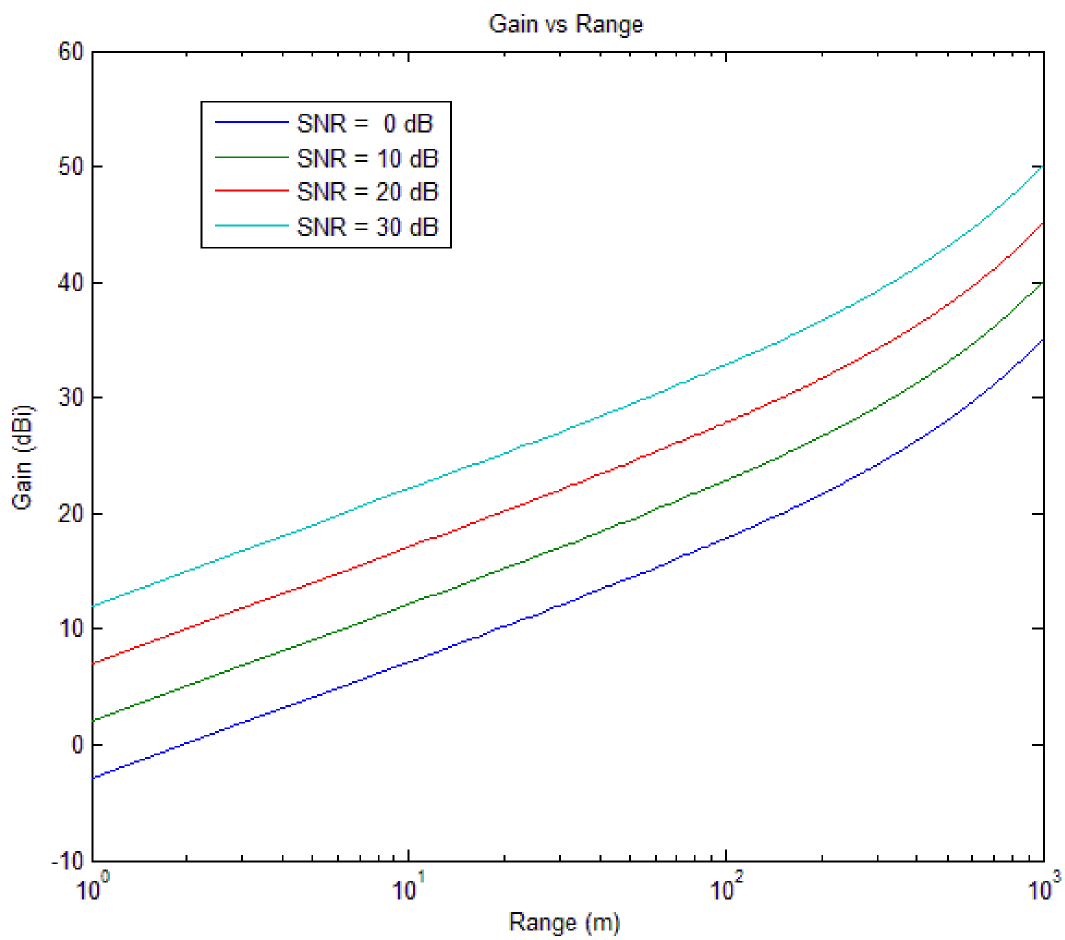


Fig 3.1.1.1 Plot showing the antenna Gain required to achieve various SNR's between 1meter and 1km

## 3.1.2 Single Radiating Element

The initial design for the radiating element comes from [11]. The design in [11] was chosen as launch point due to their wideband impedance match and high gain result. The array single element's -10 dB impedance bandwidth in [11] was 11.05%, from 57.3 GHz to 64 GHz.

The array's Gain was 18.2 dBi with a -3 dB beamwidth of 19.2°. As is, the design in [11] would suffer if it is deployed in contact with the skin. To isolate the fields in the feed line the design in [11] was modified to use an SIW feeding network instead of microstrip lines, thus making the single element an SIW fed Aperture Coupled Microstrip Patch Antenna (ACMPA) with cavity. The substrate has been replaced with RO4350 ($\varepsilon_r$=3.66) and the dimensions have been adjusted accordingly to accommodate the available substrate thicknesses. Fig. 3.1.2.1 shows the model for the SIW fed ACMPA and table 3.1.2.1 summarizes the different design parameters.

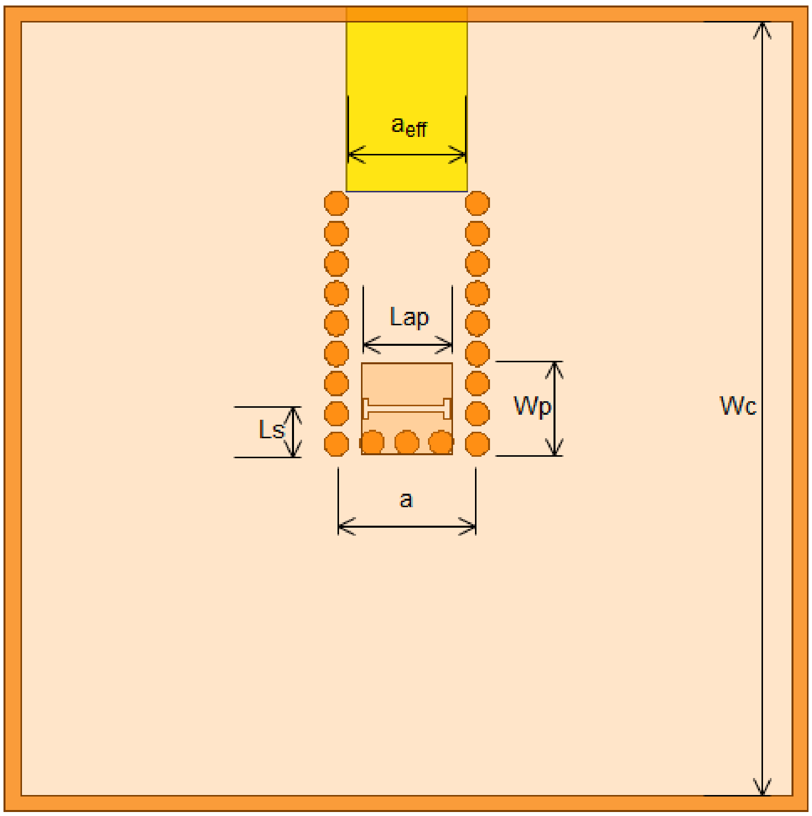


(a)

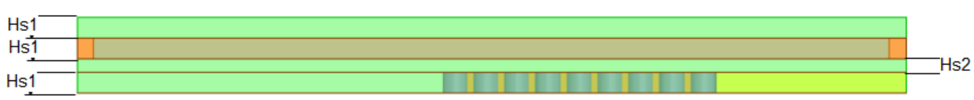


(b)

Fig. 3.1.2.1 . (a) Top and (b) side view for the single radiating element for the SIW fed ACMPA with Cavity. The parameters shown are summarized in Table 3.1.2.1

The SIW feed is designed using the design rules presented in [25] and is found in the lowest substrate level which contained the microstrip line in [11]. Equation (2) which relates the effective width of the SIW, $a_{eff}$, and the SIW's width measured from the vias' center, $a$,using the via radius, $r$, and their separation, $p$. This relationship allows designing and exciting the SIW using the same principles as a solid rectangular waveguide of width $a_{eff}$ [25].

$$a_{eff} = a - \frac{4r^2}{0.95p} \qquad (2)$$

The SIW leads to a coupling aperture whose length and width are specified by *Lap* and *Wap* respectively. This is an 'H' shaped aperture where the bar's length is *Lap* and the H's cap height is 3 times the bar's width. The aperture is found a distance *Ls* from the shorting post wall at the end of the SIW. *Ls* is measured from the center of the aperture to the center of the vias that make up the post wall. The aperture couples the SIW to the layer above which is made of a thinner substrate. Above this thinner substrate lies and air filled cavity. The cavity may be realized using a metallic core, or a hollowed, metalized, substrate. The cavity height is set equal to *Hs1* to allow the flexibility of using substrate of the same width as the first layer when building the antenna. The cavity is a square cavity with length and width *Wc*. The square patch is found on the underside of the last layer which length and width are given by *Wp*.

TABLE 3.1.2.1 SIW FED ACMPA PARAMETERS

| **Parameter** | **Value** |
|---|---|
| Hs1 | 0.254mm |
| Hs2 | 0.168mm |
| Wp | 1.12mm |
| Lap | 1.1mm |
| Wap | 0.08mm |
| Ls | 0.343mm |
| a | 1.5mm |
| $a_{eff}$ | 1.753mm |
| r | 0.15mm |
| p | 0.374mm |
| Wc | 4.8mm |

The reflection coefficient for this structure can be seen in fig. 3.1.2.2. It shows that a -10 dB matching was achieved throughout bandwidth of interest and beyond. The radiation pattern at 56.16, 60.48 and 64.8 GHz can be seen in figures 3.1.2.3, 3.1.2.4, and 3.1.2.5 respectively. The radiation patterns show a slight lobing and have a very wide beamwidth. This is a desired property, especially along the H-Plane, in order to cover a wider effective beamwidth once the beam-scanning array is formed. The results are summarized in table 3.1.3.1. Fig 3.1.2.6 shows the cross polarization. The cross polarization remains below the -30dB along the band and across all angles.

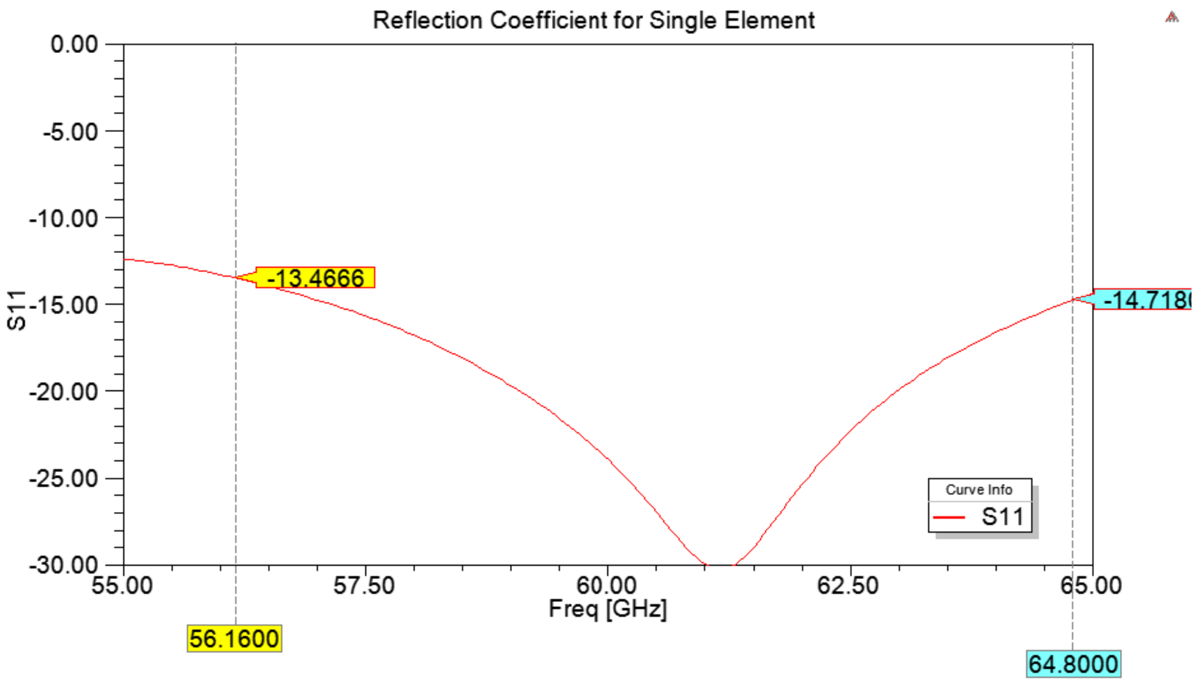


Fig. 3.1.2.2 . Reflection coefficient for the single element.

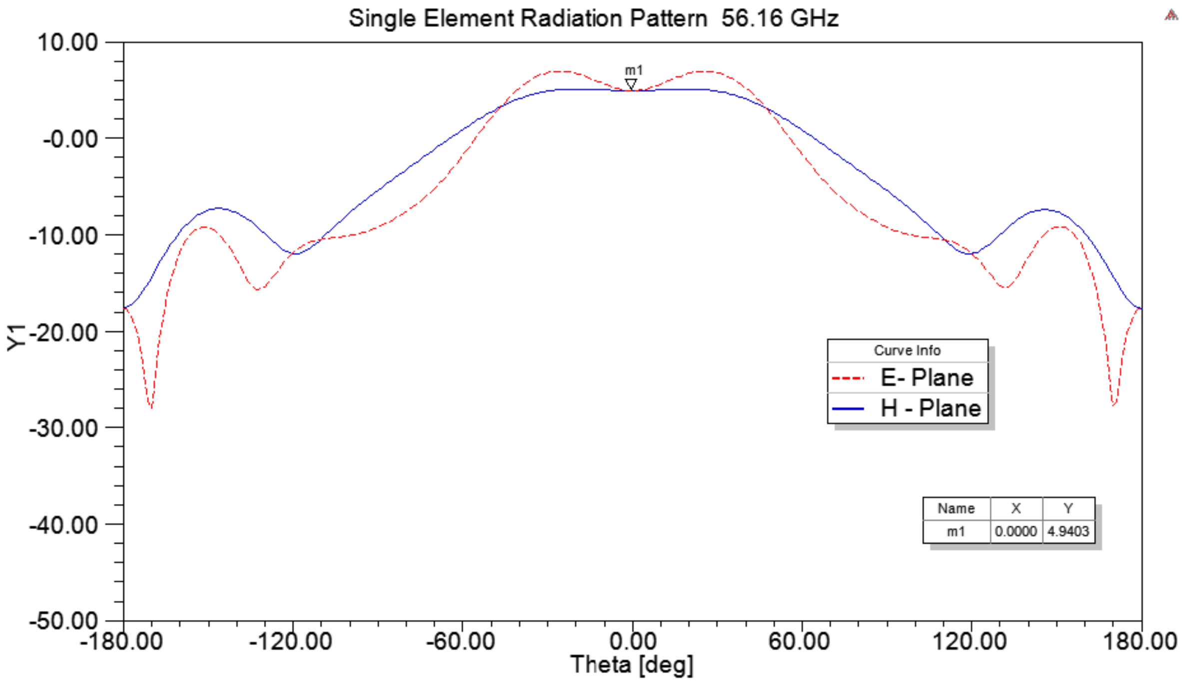


Fig. 3.1.2.3 Radiation pattern for the single element at the high frequency in the band of interest, 64.8 GHz. Gain is 4.94dBi at zenith.

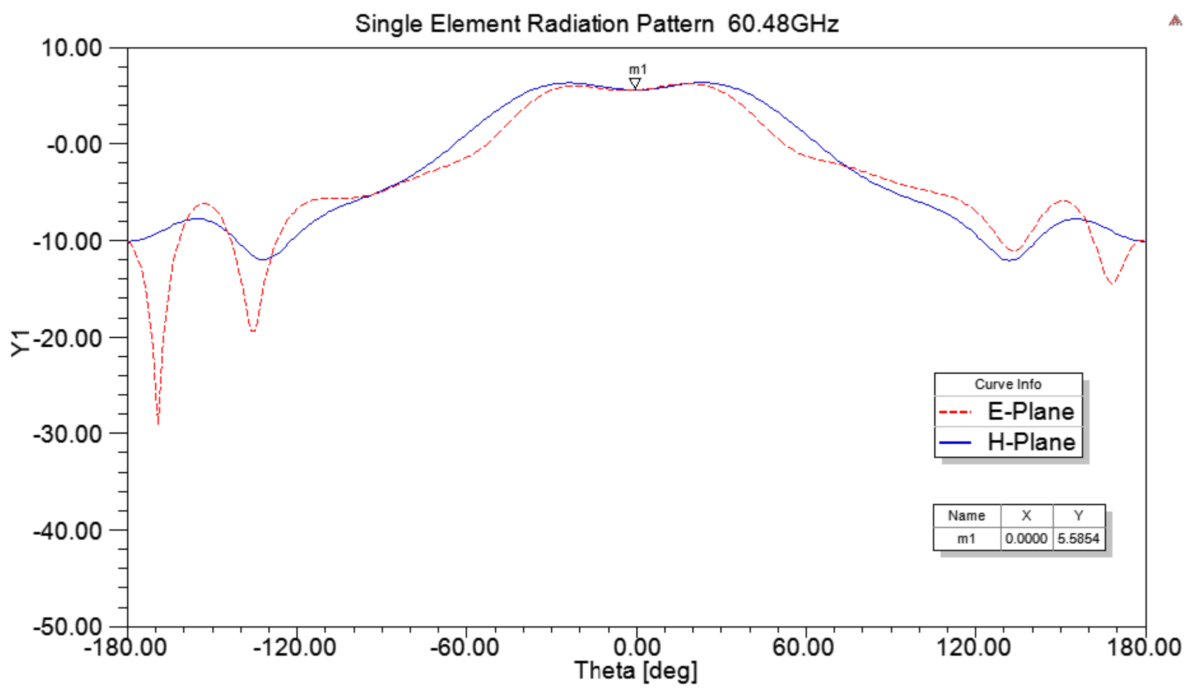


Fig. 3.1.2.4 Radiation pattern for the single element at the center frequency, 60.48 GHz. Gain is 5.58dBi at zenith.

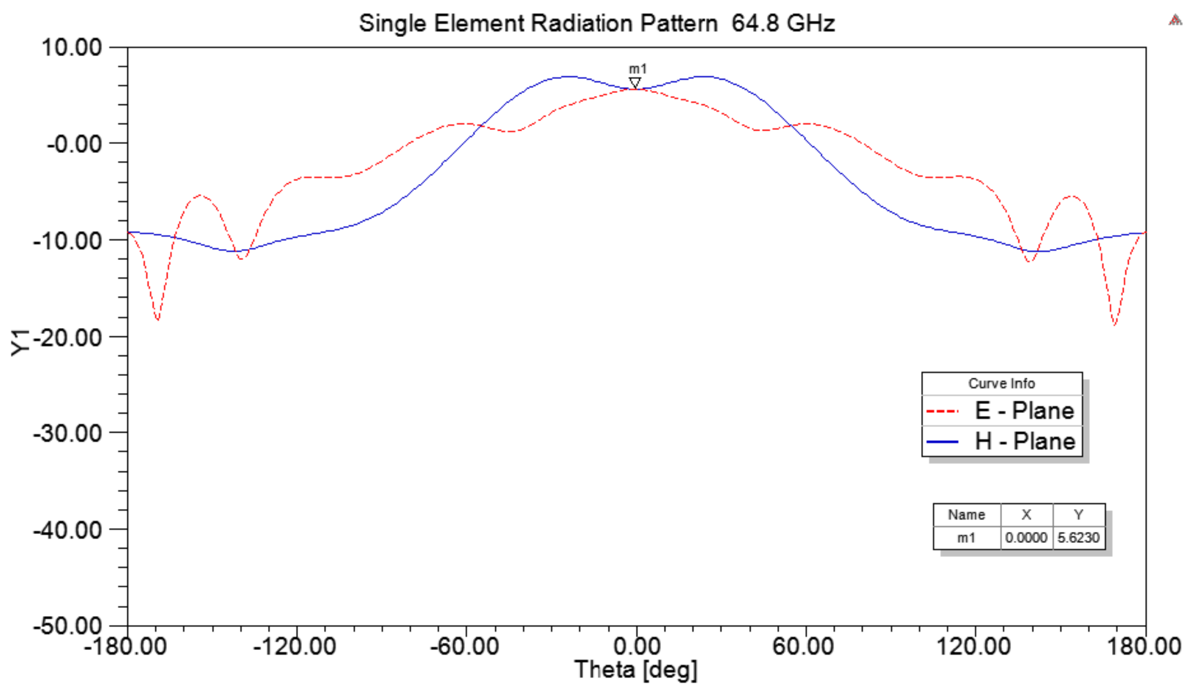


Fig. 3.1.2.5 Radiation pattern for the single element at the high frequency in the band of interest, 64.8 GHz. Gain is 5.62dBi at zenith.

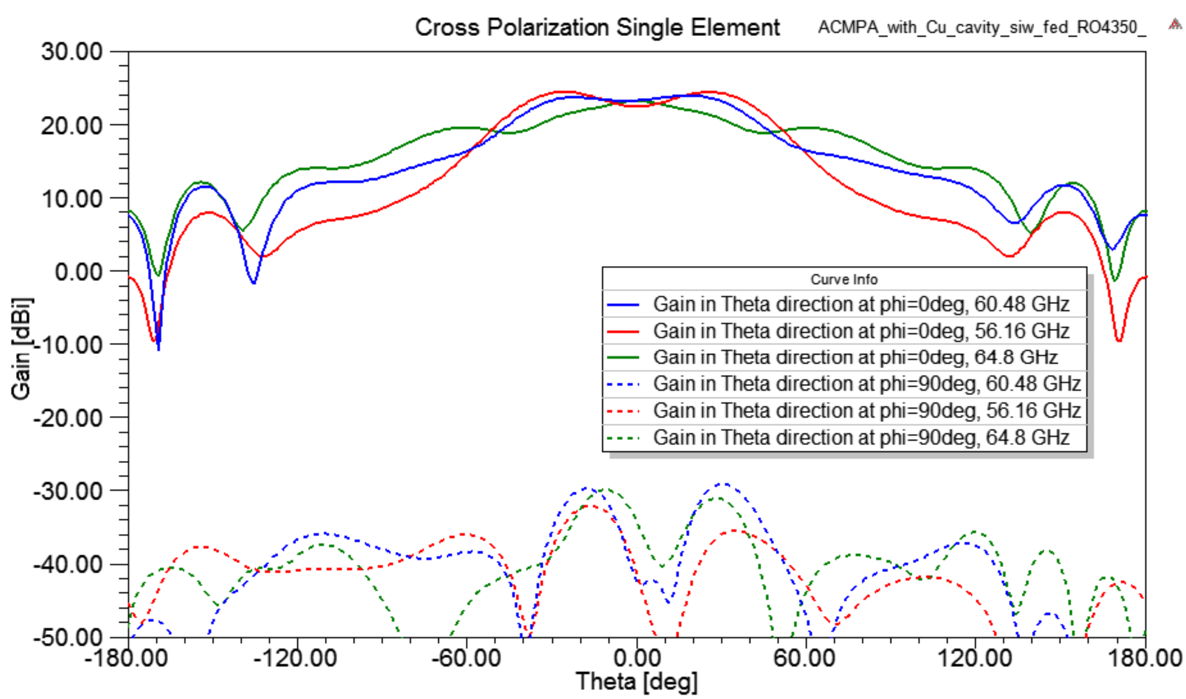


Fig. 3.1.2.6 Cross Polarization for Single Element showing very good linear polarization across all frequencies and angles

TABLE 3.1.3.1 SINGLE ELEMENT PATTERN SUMMARY

| | | | |
|---|---|---|---|
| **Frequency (GHz)** | 56.16 | 60.48 | 64.8 |
| **Gain (dBi)** | 4.94 | 5.58 | 5.62 |
| **Max Gain (dBi)** | 6.96 | 6.34 | 6.89 |
| **Directivity (dBi)** | 5.63 | 6.08 | 6.11 |
| **Efficiency (%)** | 93.32 | 95.12 | 95.22 |
| **E-Plane-3 dB Beamwidth (deg)** | 101.12 | 86.37 | 66.4 |
| **H-Plane -3 dB Beamwidth (deg)** | 108.97 | 106.53 | 103.76 |

### 3.1.3 Four Element Array H-Plane

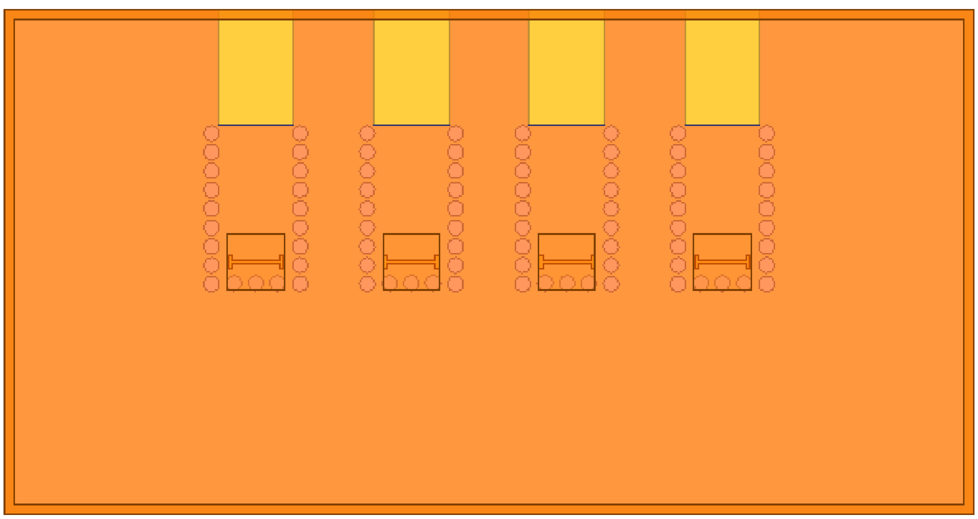

Fig. 3.1.3.1. Top view for the four element array. The elements are positioned along the H - Plane

Fig 3.1.3.1 shows the intermediate array used to evaluate the feasibility of this radiating element in a bigger array. Evaluating in such a small array allows for quicker design identifying potential problems early. Using eq (3) it was determined that separation(*d*) of 3.08mm was appropriate for a ±40° scan angle without introducing grating lobes at the maximum inclination. Accommodating a ±40° scan angle would allow integration with a Rotman lens such as that reported in [22] for the beamforming network. The wavelength ($\lambda$) used was the wavelength of the highest frequency in the band of interest since this would ensure no grating lobes incurring throughout the bandwidth.

$$d = \frac{\lambda_{64.8GHz}}{1+\sin(\theta)} \tag{3}$$

The array is excited by 4 independent ports. Placing the independently fed elements along the H-plane means that this will be the beam-switching, horizontally aligned plane. Because of the shape of the single element, this configuration avoids twisting and cramming the SIW feed lines. A configuration along the E-plane with this SIW fed radiating element may be possible but due to the difficulty in arranging the SIW feed lines in the limited space, such an arrangement is not explored in this work. All the elements are found within the same cavity which requires resizing this cavity along the H-plane from 4.8 mm to 9.43 mm to accommodate the extra elements.

The impedance match for this array is shown in fig. 3.1.3.2. It is seen that there was no noticeable change with the single element's reflection coefficient, shown in figure 3.1.2.2. The isolation between the ports is shown in fig 3.1.3.3. The mutual coupling is below -20 dB for all port combinations. The radiation patterns can be found in figures 3.1.3.4, 3.1.3.5, and 3.1.3.6. The results are summarized in table 3.1.3.1

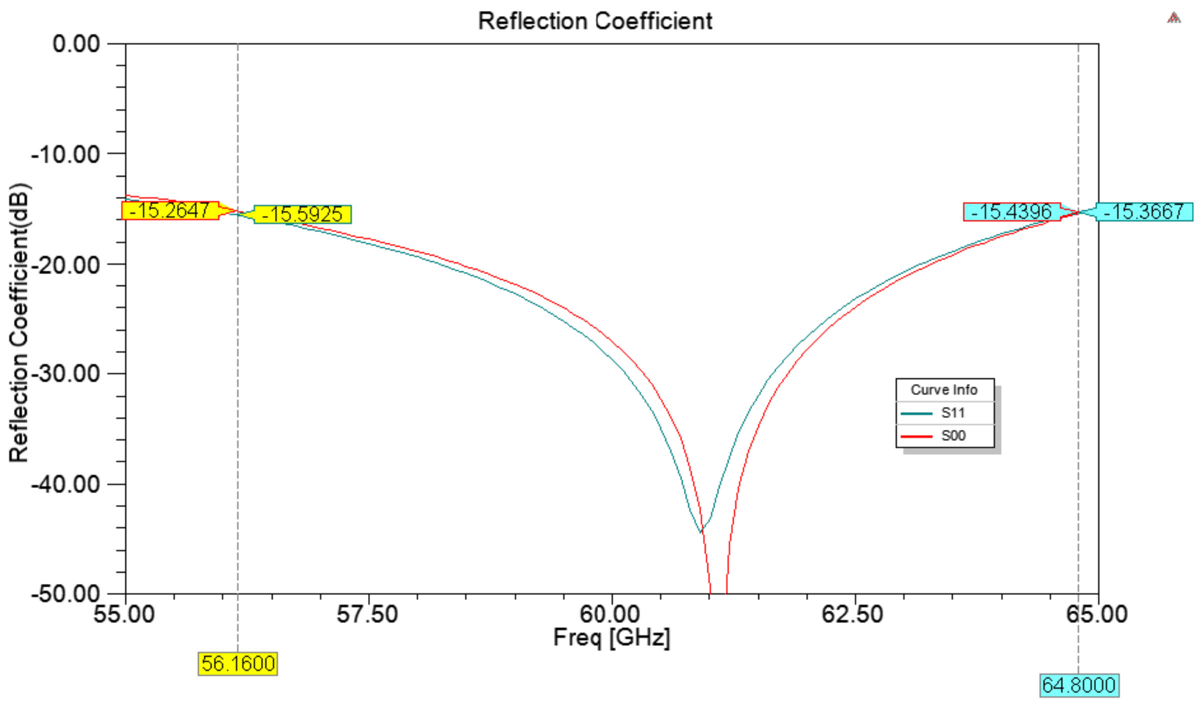


Fig. 3.1.3.2. Reflection Coefficient for the H-Plane Array. Only the first two ports need to be shown due to the structure's symmetry.

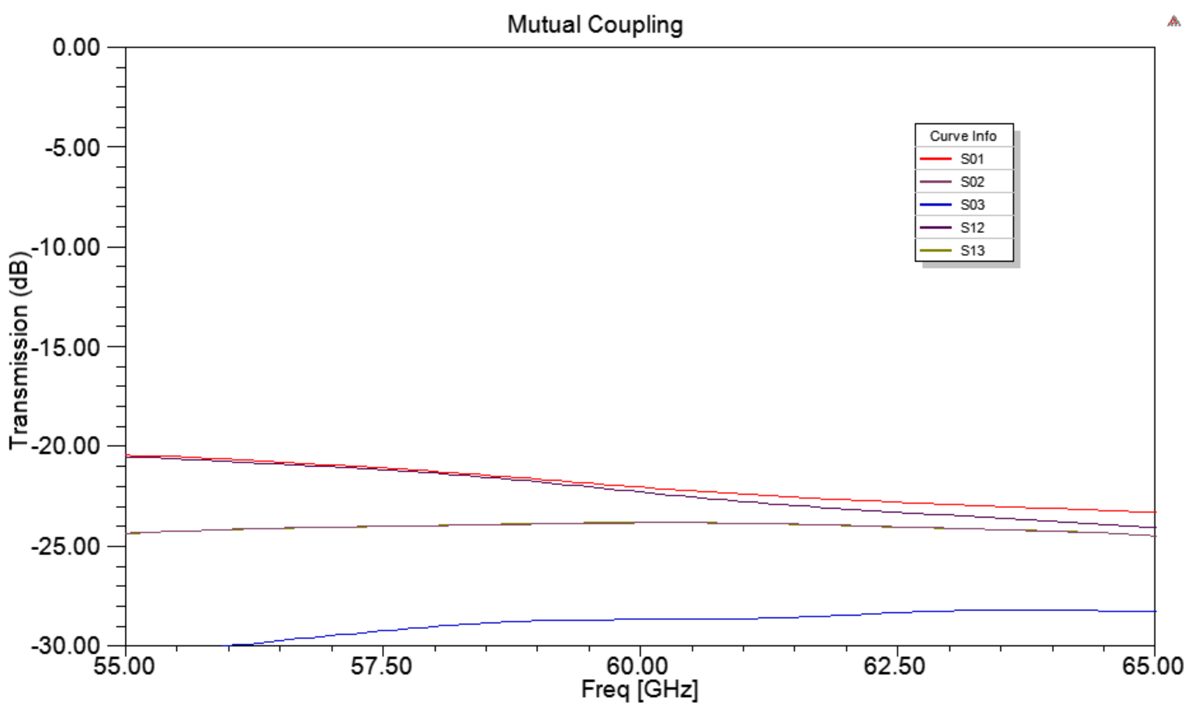


Fig. 3.1.3.3. Transmission coefficient between each port. Only 5 need to be shown; the rest may be inferred from symmetry and reciprocity.

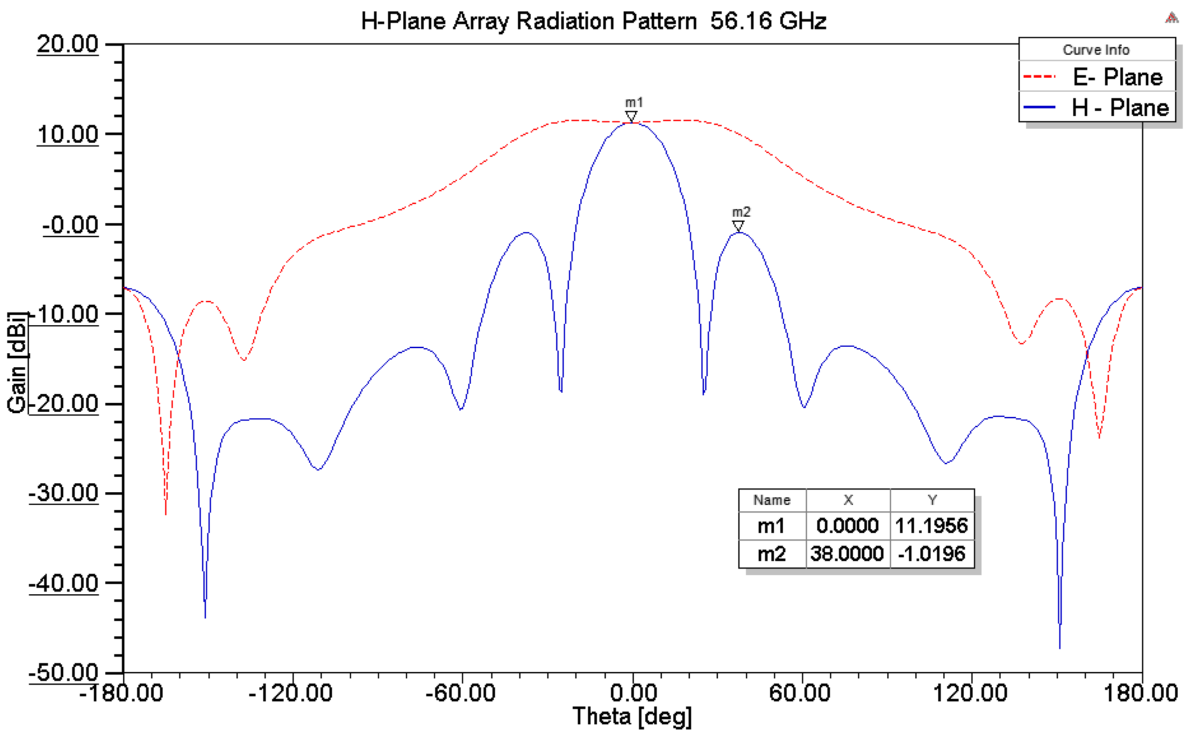


Fig. 3.1.3.4. –Radiation pattern for the H-Plane array at 56.16 GHz. The maximum gain is 11.20 dB. The H-plane -3 dB beamwidth is 22.85° and the side lobes are 12.22 dB below the main lobe

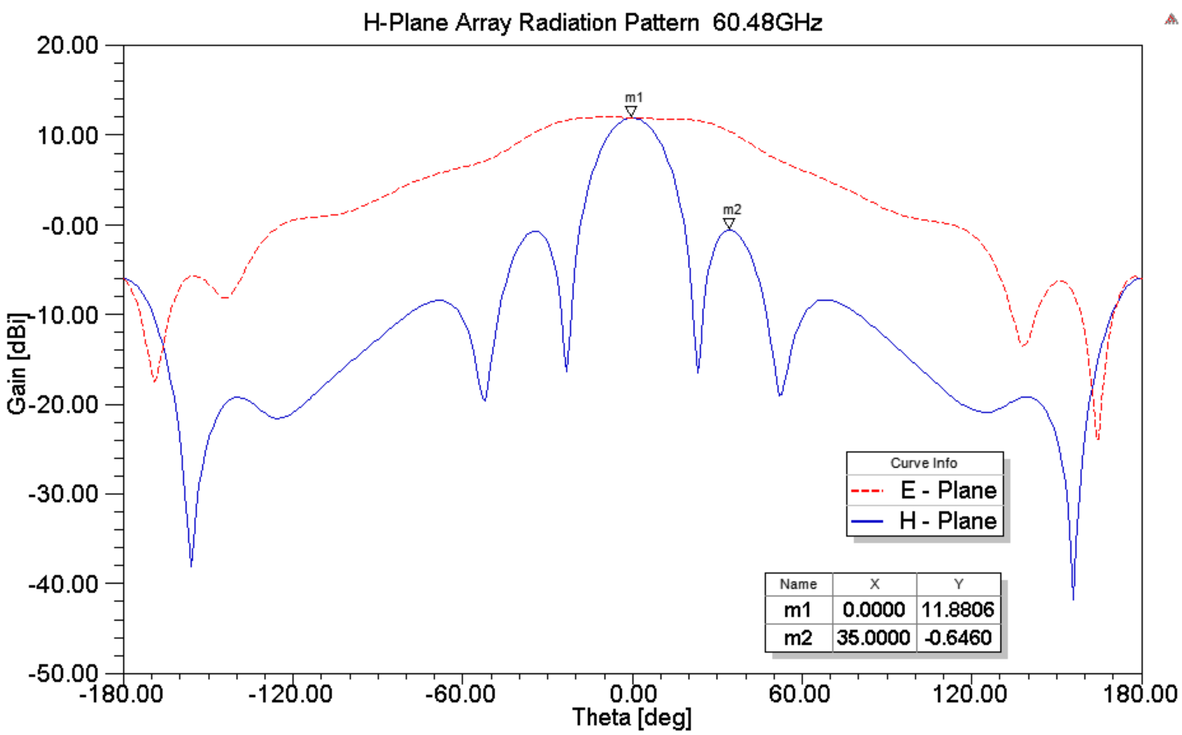


Fig. 3.1.3.5. Radiation pattern for the H-Plane array at 60.48 GHz. The maximum gain is 11.88 dB. The H-plane -3 dB beamwidth is 20.49° and the side lobes are 12.53 dB below the main lobe

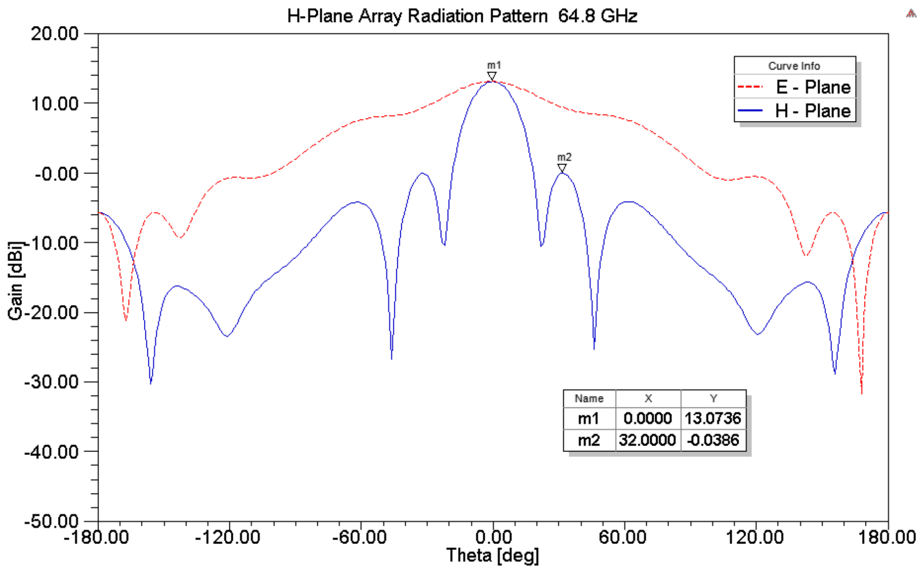


Fig. 3.1.3.6. Radiation pattern for the H-Plane array at 64.8 GHz. The maximum gain is 13.07 dB. The H-plane -3 dB beamwidth is 20.01° and the side lobes are 13.11 dB below the main lobe

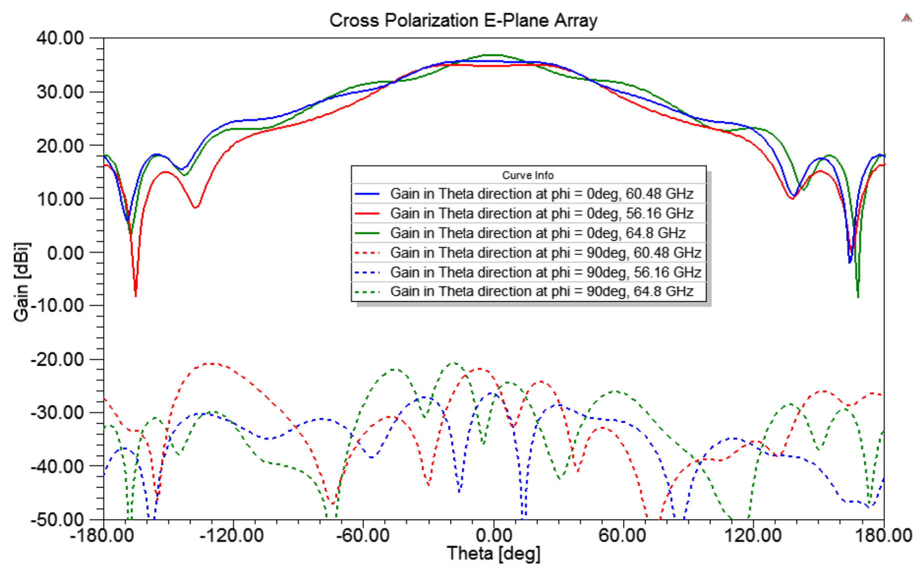


Fig. 3.1.3.7 Cross polarization for the H-Plane array

TABLE 3.1.3.1 H-PLANE ARRAY PATTERN SUMMARY

| **Frequency (GHz)** | **Gain (dBi)** | **Side Lobe Level (dB)** | **H-Plane -3 dB Beamwidth (deg)** |
|---|---|---|---|
| 56.16 | 11.20 | 12.22 | 22.85 |
| 60.48 | 11.88 | 12.53 | 20.49 |
| 64.80 | 13.07 | 13.11 | 20.01 |

## 3.1.4 Four Element Array E-Plane

Following the idea from the previous section, a 1x4 element array was designed by aligning the elements along the E-plane. This would allow testing the T-junctions designed in section 3.3. This array was originally designed only using 254 μm thick layers. A second design was required to accommodate the second coaxial-SIW transition presented in section 3.4. Both arrays are presented in the following sections.

### 3.1.4.1 Array With 254 μm Thick Layers

The array can be seen in fig. 3.1.4.1.1. and fig 3.1.4.1.2. The layers shown in figs 3.1.4.1.2a, 3.1.4.1.2.b, and 3.1.4.1.2.c contain the details for the single radiating element whose dimensions are detailed in fig. 3.1.2.1. Like the H-plane array in section 3.1.3, the cavity was resized to 9.43 mm to accommodate four elements with a separation of 3.08 mm. The resize this time occurs along the E-plane. In fig 3.1.4.1.2.c it can be seen that the elements are oriented in alternating fashion and that SIW for each pair of elements leads to a common H-slot.. These two slots coupling into the layer bellow found in fig 3.1.4.1.2.d. The SIWs in this layer also combine into a mutual H-slot. This slot in turn couples to the lowest level seen in fig. 3.1.4.1.2.e. This last layer contains an SIW which leads to the excitation; a rectangular waveport for the purpose of the design.

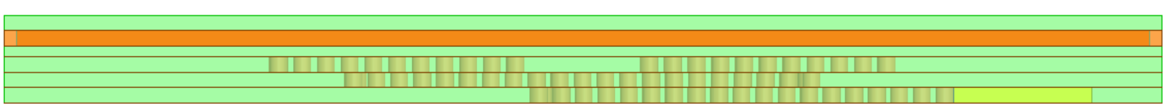

Fig. 3.1.4.1.1 . Side view of the 1x4 E-plane array constructed using 254 μm thick substrates for the vertical corporate feed

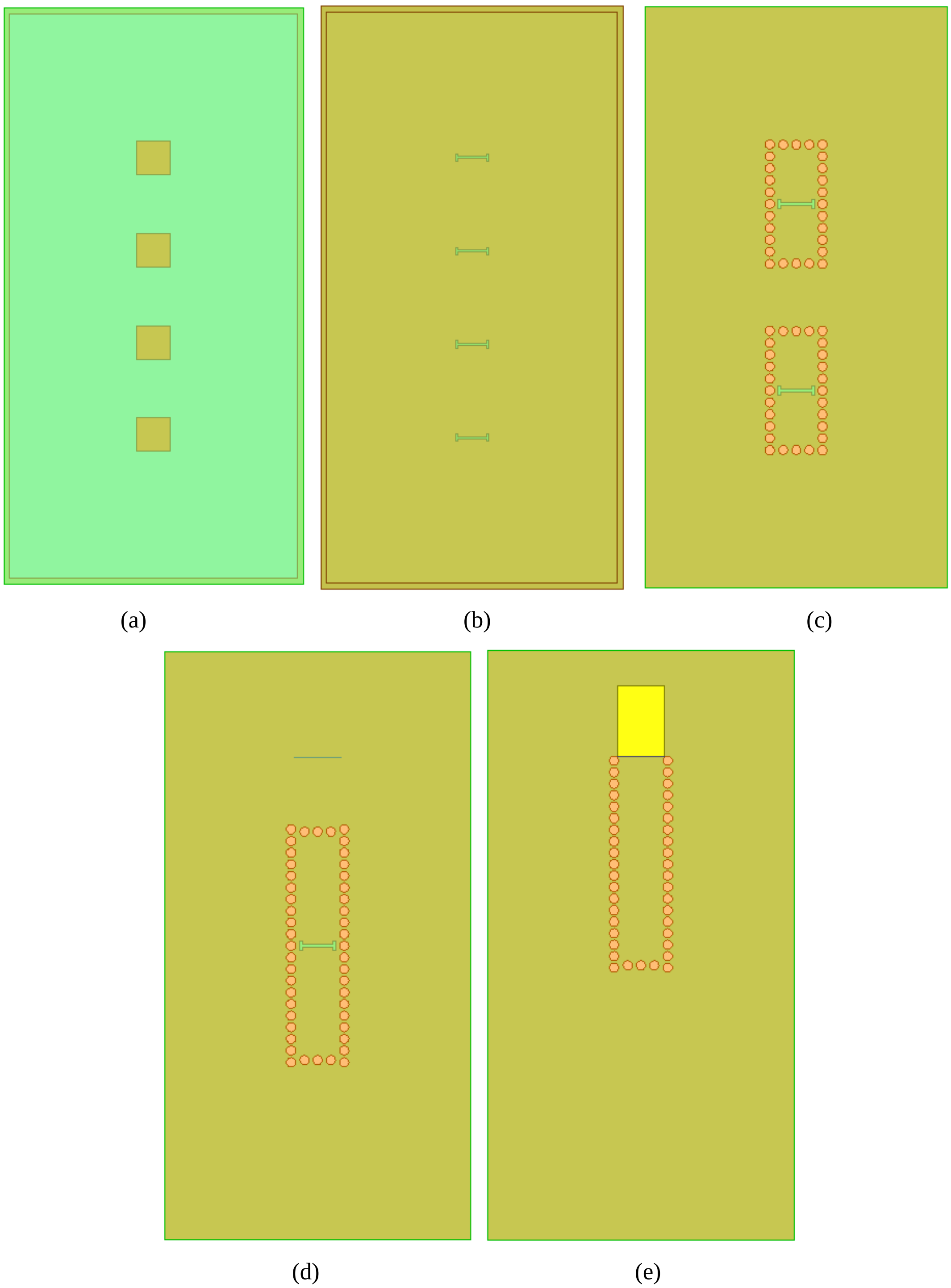

Fig. 3.1.4.1.2. Top view of the layers starting at the uppermost layer (a) all the way to the lower level (e)

The reflection coefficient can be seen in fig. 3.1.4.1.3 and it shows that the array with the corporate feed meets the -10 dB bandwidth throught the bandwidth of interest and meets the 14.29% bandwidth. The radiation pattern can be seen in figures 3.1.4.1.4 throught 3.1.4.1.5.

Table 3.1.4.1.1 summarizes the results. Table 3.1.4.1.1 includes the directivity for each frequency. This allows seeing the losses incurred by the vertical corporate feed. As seen in table 3.1.4.1.1, the difference between the gain and the directivity translate to 80.57%, 84.54, and 85.4% efficiency at 56.16, 60.48, and 64.8 GHz respectively. It is worth noting that the radiation patterns are not perfectly symetrical, unlike those shon in section 3.1.3. This is not unexpected as there is a slight asymetry in the power dividers used. More on this can be found in section 3.3.1. No attempt was made to offset this as it does not significatly move the main lobe away from 0°. The most significant difference is seen in the 1.01 dB difference between the sidelobes at 56.16 GHz in fig. 3.1.4.1.4

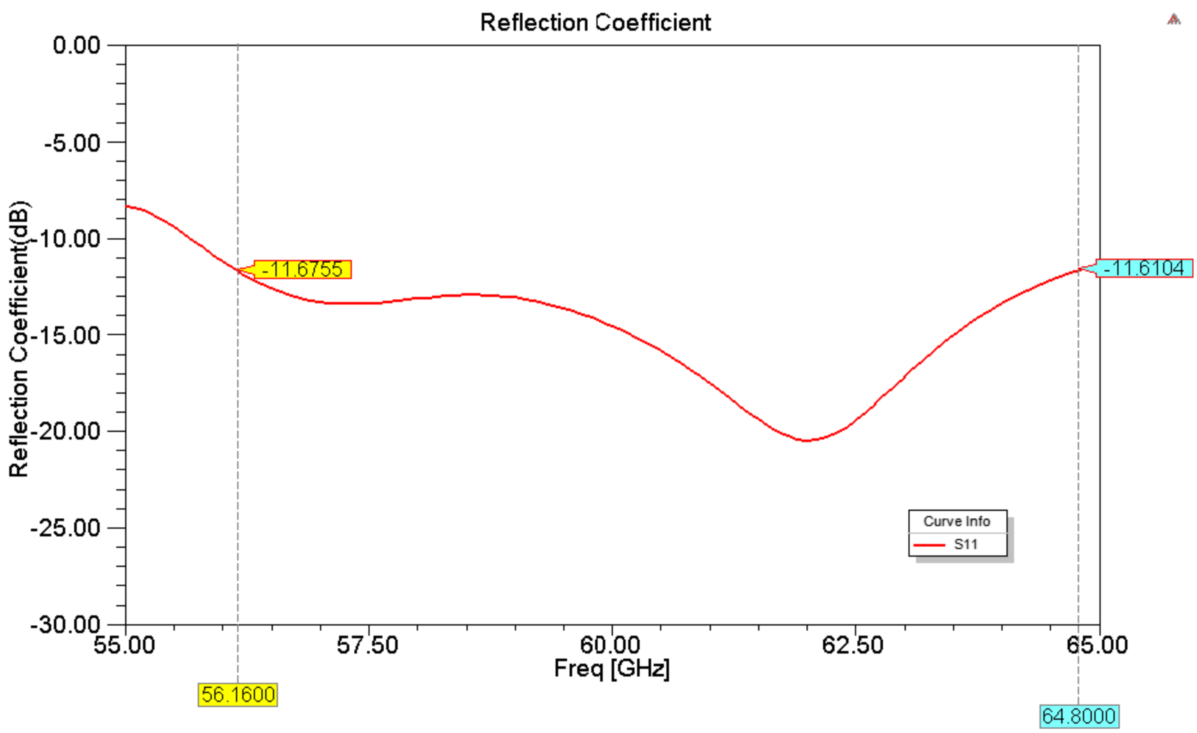


Fig. 3.1.4.1.3. Reflection Coefficient for the E-Plane Array. .

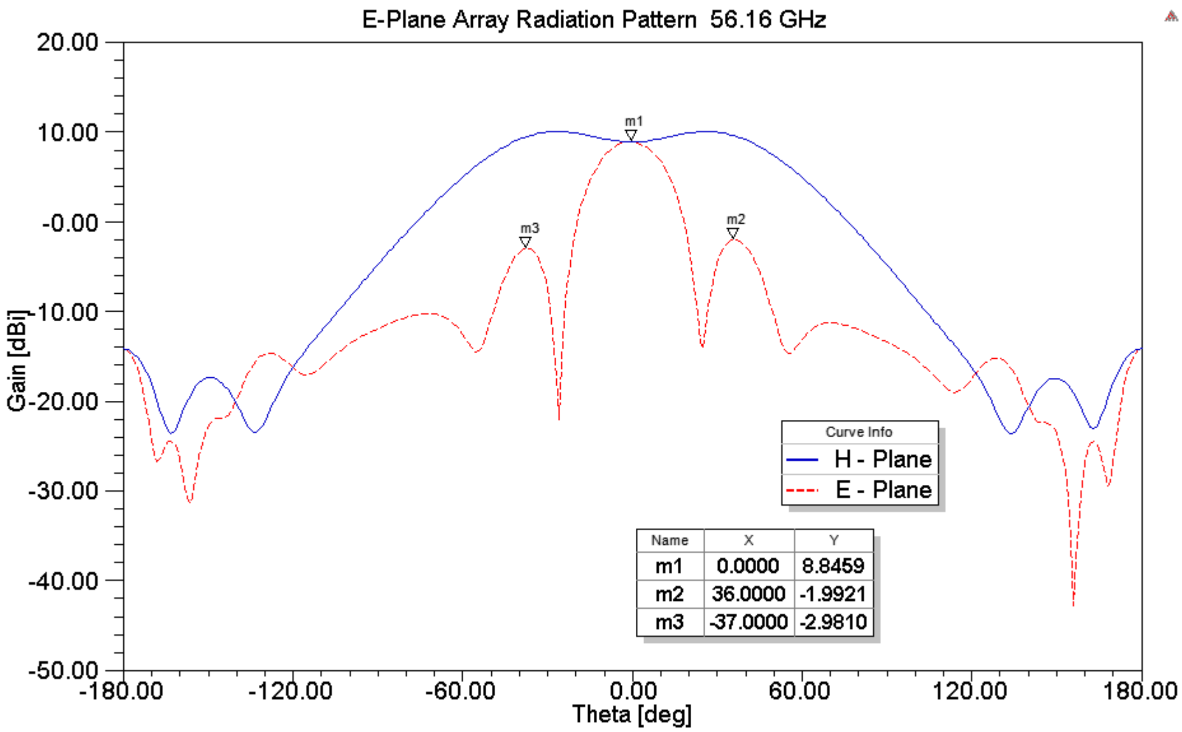


Fig. 3.1.4.1.4. Radiation pattern for E-plane array at 56.16 GHz

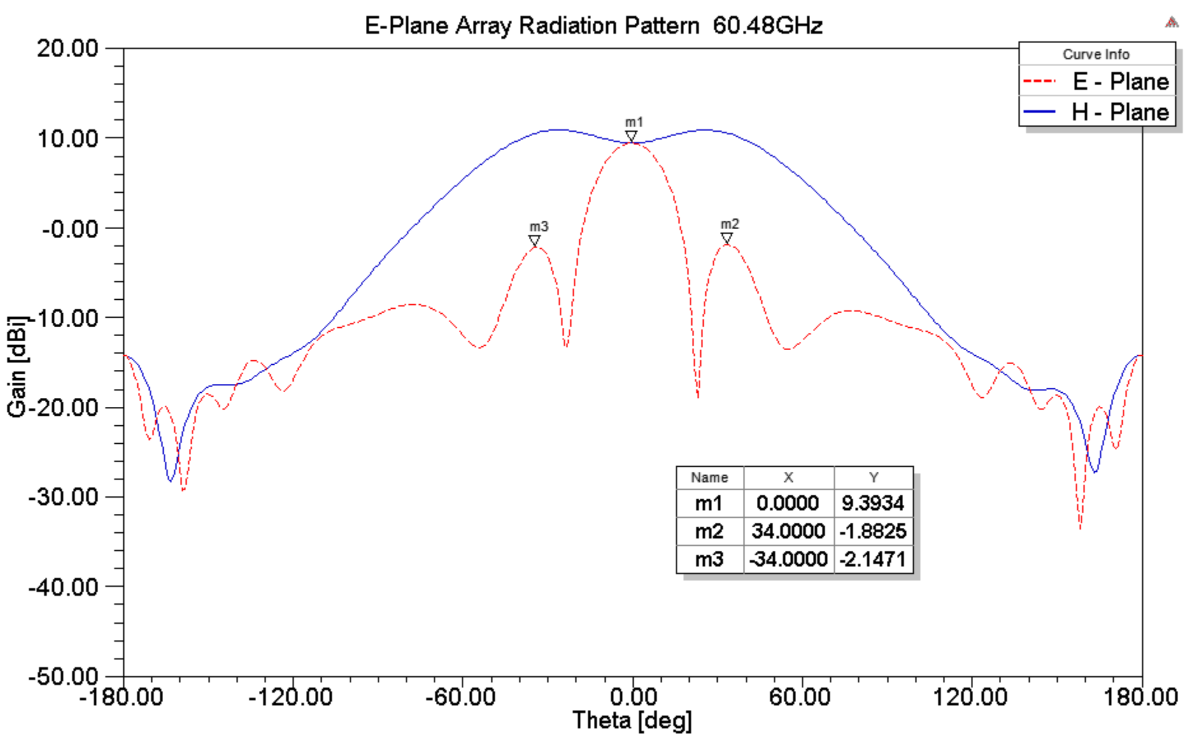


Fig. 3.1.4.1.5. Radiation pattern for E-plane array at 60.48 GHz

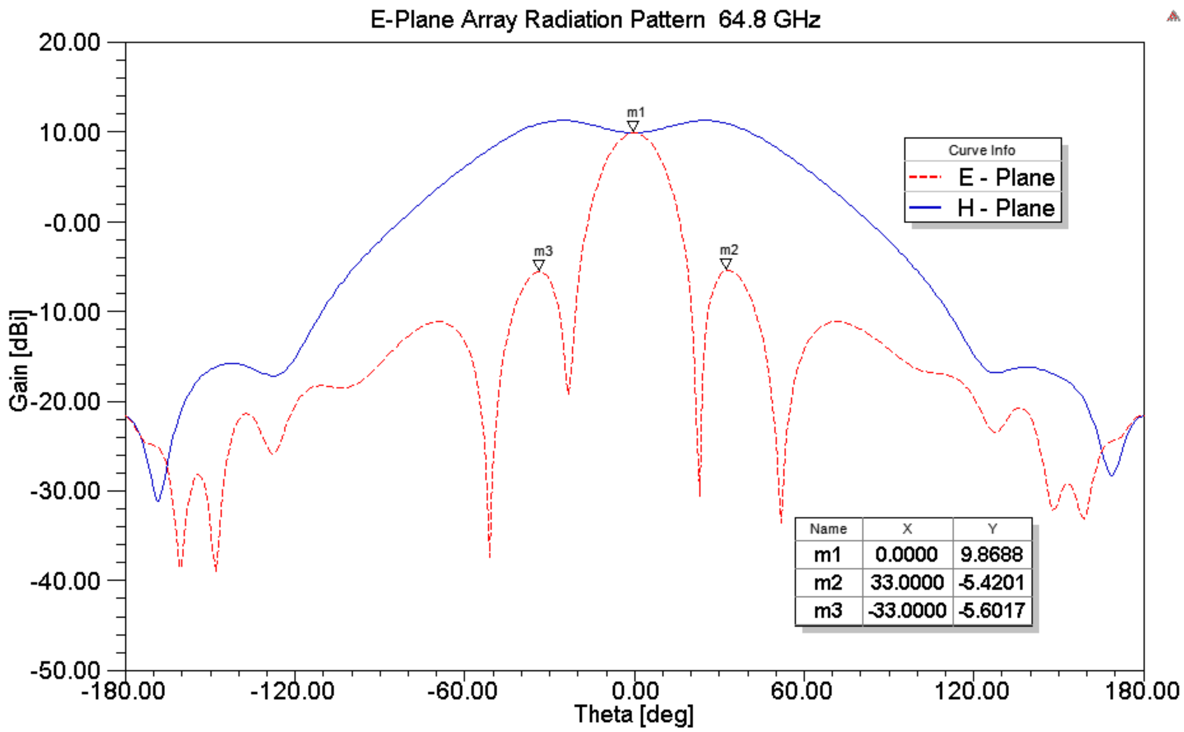


Fig. 3.1.4.1.6 Radiation pattern for E-plane array at 64.80 GHz

TABLE 3.1.4.1.1 E-PLANE ARRAY PATTERN SUMMARY

| **Frequency (GHz)** | **Gain (dBi)** | **Directivity (dBi)** | **Efficiency (%)** | **Side Lobe Level (dB)** | **E-Plane -3 dB Beamwidth (deg)** |
|---|---|---|---|---|---|
| 56.16 | 8.85 | 11.01 | 80.57 | 10.84 | 24.61 |
| 60.48 | 9.39 | 11.07 | 84.54 | 11.27 | 21.62 |
| 64.80 | 9.87 | 11.49 | 85.04 | 15.29 | 19.08 |

Because this array incorporates the vertical corporate feed it was also a computationally economical model to modify in order to see the effects of the adhesive on the array. FR4 no flow prepeg was chosen because the manufacturing process being considered would allow creating vias throught this adhesive and because this adhesive would not seep into the cavity during the fabrication. The side view of the antenna with adhesive can be seen in fig 3.1.4.1.7. The vias in the lowermost level, shown in fig 3.1.4.1.5.e, are unaffected by the adhesive. The vias shown in fig 3.1.4.1.5.d and fig 3.1.4.1.5.c now extend through the adhesive to connect to the copper layer bellow.

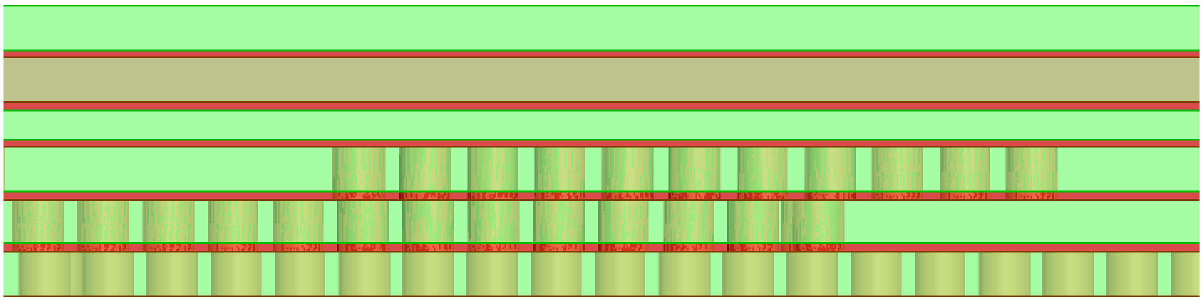

Fig. 3.1.4.1.7. Zoomed side view of the 1x4 E-plane array constructed using 254 µm thick substrates for the vertical corporate feed. The adhesive layers, in red, are each 43.17 µm thick.

This configuration did not have a severely detrimental effect on the array's impedance match. The result can be seen in Fig 3.1.4.1.8. The -10 dB bandwidth is mildly reduced on the lower end of the band of interest and at 59.8 GHz there is a very mild region where it reaches 0.02 dB over the -10 dB bandwidth. A more varied analysis may seek to combine different adhesives and modify the design parameters to better cope with the effect of the adhesive. Such an analysis was considered beyond the scope of this project as its feasibility will vary depending on the materials and methods available to the individual when fabricating the antenna.

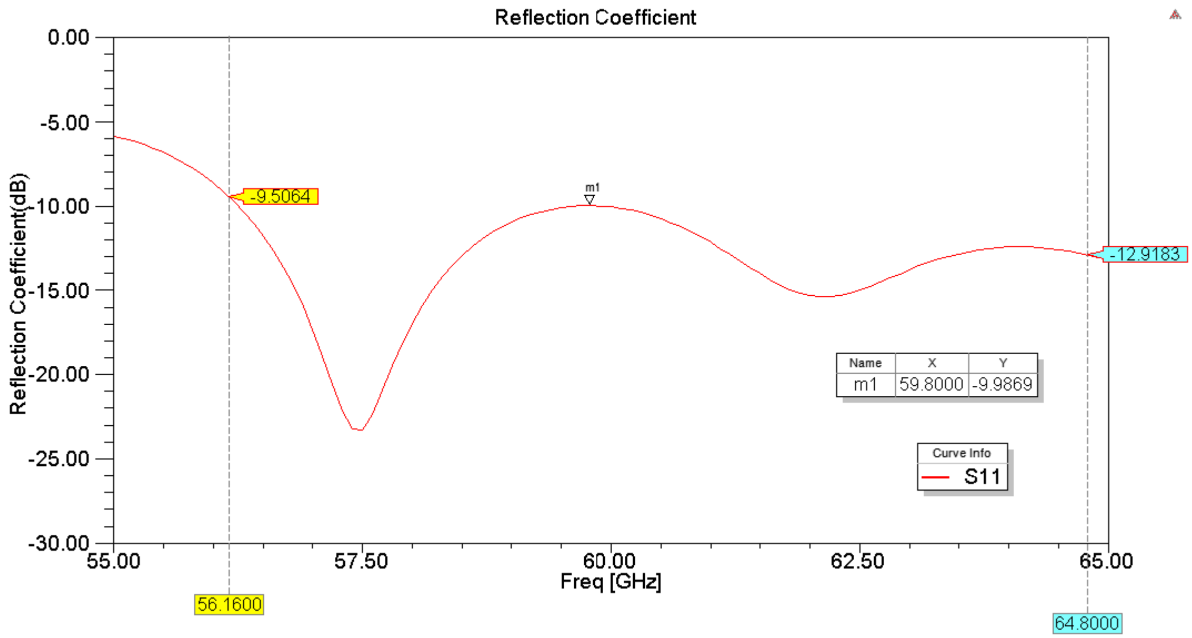


Fig. 3.1.4.1.8. Reflection Coefficient for the E-Plane Array including adhesive.

### 3.1.4.2 Array With 508 µm and 662 µm Thick Layers

The final version of the array uses progressively thinning substrates in order to match the second coax-SIW transition in section 3.D, which uses 762 µm thick substrate, to the radiating elements that use 254 µm thick substrate in their lowermost level. The parameters for the T junctions that allow transitioning between these layers can be found in sections 3.3.3 and 3.3.2. A 1x4 element array aligned along the E-Plane was designed to fully test out the corporate feed using the new transitions. Figure 3.1.4.2.1 shows the side view with the thicker substrates.

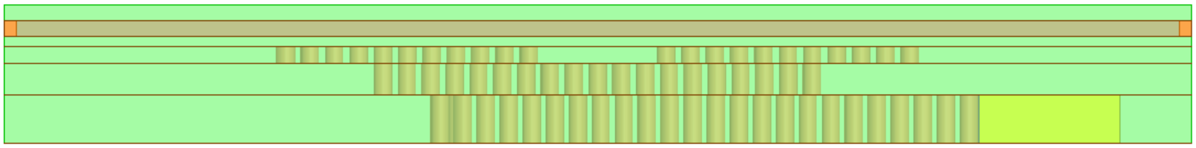

Fig. 3.1.4.2.1 Side view of the array using 762 µm thick substrate in the lowermost layer and 508 µm thick substrate in the following layer.

Fig 3.1.4.2.2 shows the reflection coefficient. Using the parameters that had been obtained for the stand-alone T-Junctions found in sections 3.3.3 and 3.3.2 the array failed to comply with the -10 dB bandwidth in the band of interest. This corresponds to the plot with the *offset* = 0.45 in figure 3.1.4.2.2. A parametric analysis on the value of *offset* was conducted. This *offset* corresponds to the offset of the H-Slot for the transition shown in section 3.3.3. A bandwidth exceeding the 14.28 % desired -10 dB bandwidth was obtained with the *offset* value of 0.4. The results of parametric analysis are shown in figures 3.1.4.2.2 and 3.1.4.2.3; the later in smith chart form.

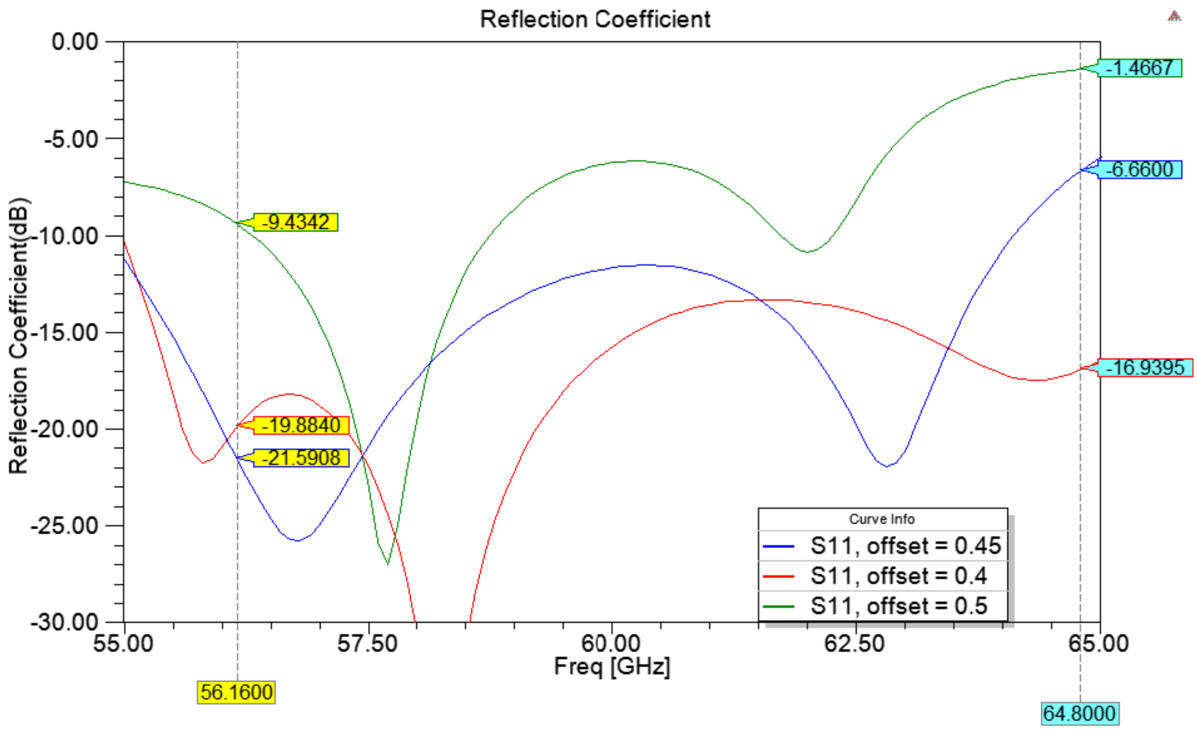


Fig. 3.1.4.2.2. Reflection Coefficients for the E-Plane Array with 762 μm and 508 μm thick substrate.

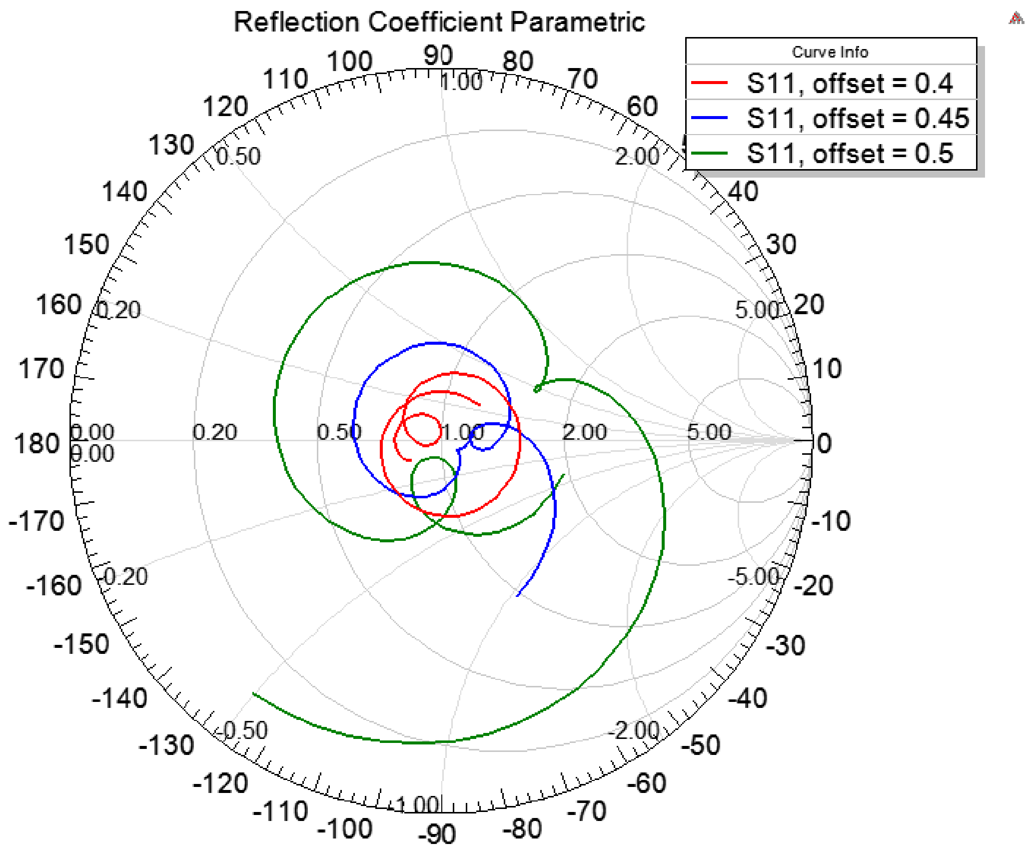


Fig. 3.1.4.2.3. Reflection Coefficients for the E-Plane Array with 762 µm and 508 µm thick substrates.

The radiation patterns are seen in figures 3.1.4.2.4, 3.1.4.2.5, and 3.1.4.2.6. As in the previous section, the patterns show a slight asymmetry. These patterns where created using the parametric variation for which *offset* = 0.4. The results for the individual patterns can be seen in table 3.1.4.2.1. Figure 3.1.4.2.7 shows a very good cross polarization isolation of over 40dB indicating a pure linear polarization along the E-plane

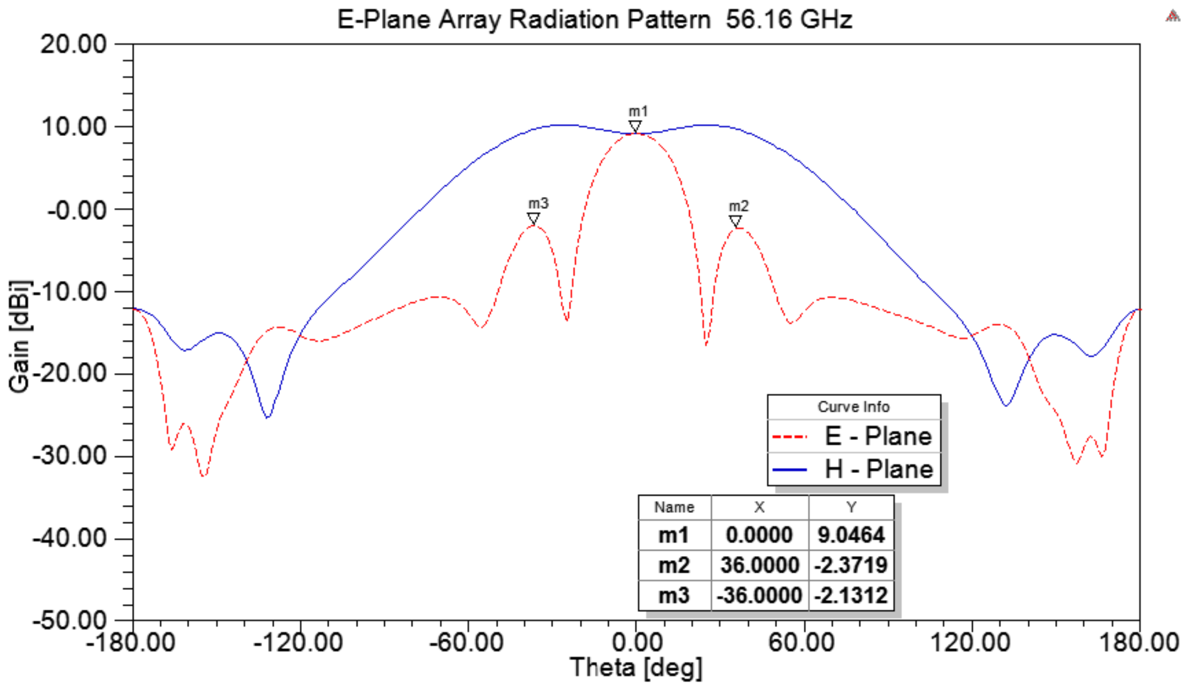


Fig. 3.1.4.2.4. Radiation pattern for E-plane array with 762 μm and 508 μm thick substrates at 56.16 GHz

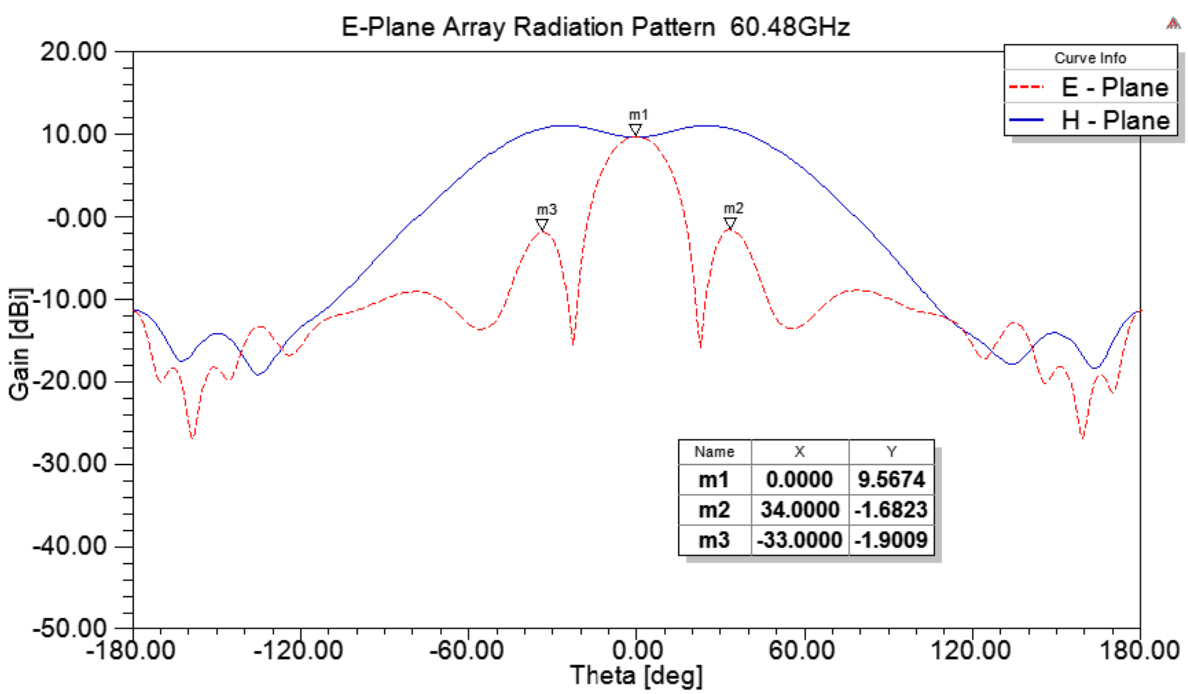


Fig. 3.1.4.2.5. Radiation pattern for E-plane array with 762 μm and 508 μm thick substrates at 60.48 GHz

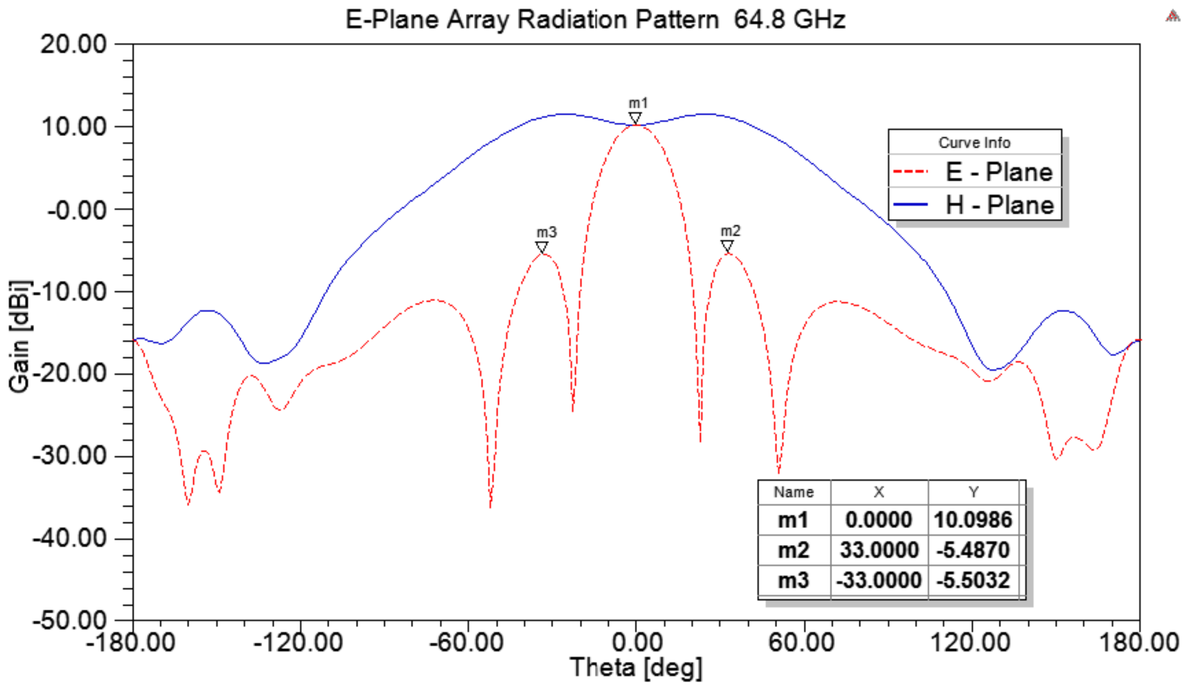


Fig. 3.1.4.2.6. Radiation pattern for E-plane array with 762 µm and 508 µm thick substrates at 64.80 GHz

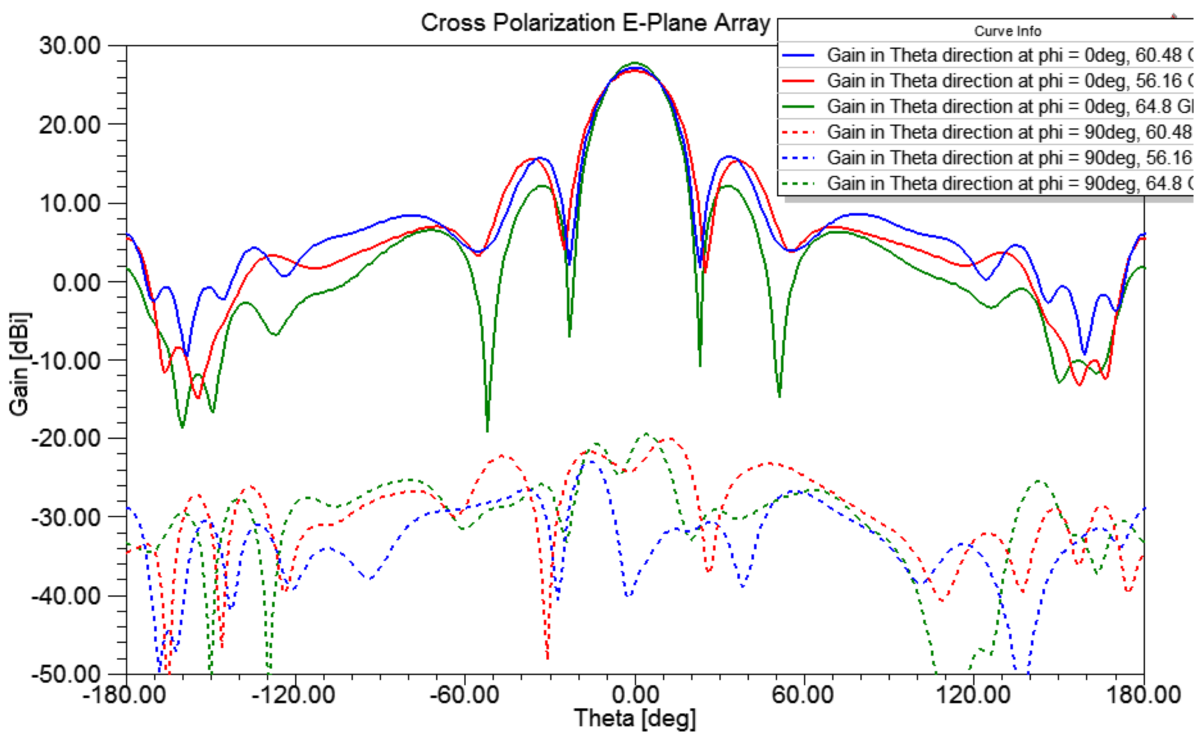


Polarization for E-plane array with 762 µm and 508 µm thick substrates

TABLE 3.1.4.2.1 E-PLANE ARRAY WITH 762 AND 508 THICK SUBSTRATES PATTERN SUMMARY

| **Frequency (GHz)** | **Gain (dBi)** | **Directivity (dBi)** | **Efficiency (%)** | **Side Lobe Level (dB)** | **E-Plane -3 dB Beamwidth (deg)** |
|---|---|---|---|---|---|
| 56.16 | 9.05 | 11.17 | 80.90 | 11.18 | 23.83 |
| 60.48 | 9.55 | 11.18 | 84.96 | 11.24 | 21.51 |
| 64.80 | 10.10 | 11.62 | 85.90 | 15.58 | 18.89 |

A configuration like that shown in fig 3.1.4.1.7 which uses adhesives was created for this array as well. The results are shown in fig. 3.1.4.2.7. The adhesive did not severely affect the -10 dB bandwidth. Only between 60.12 and 61.2 GHz did the reflections rise to -9.62 dB.

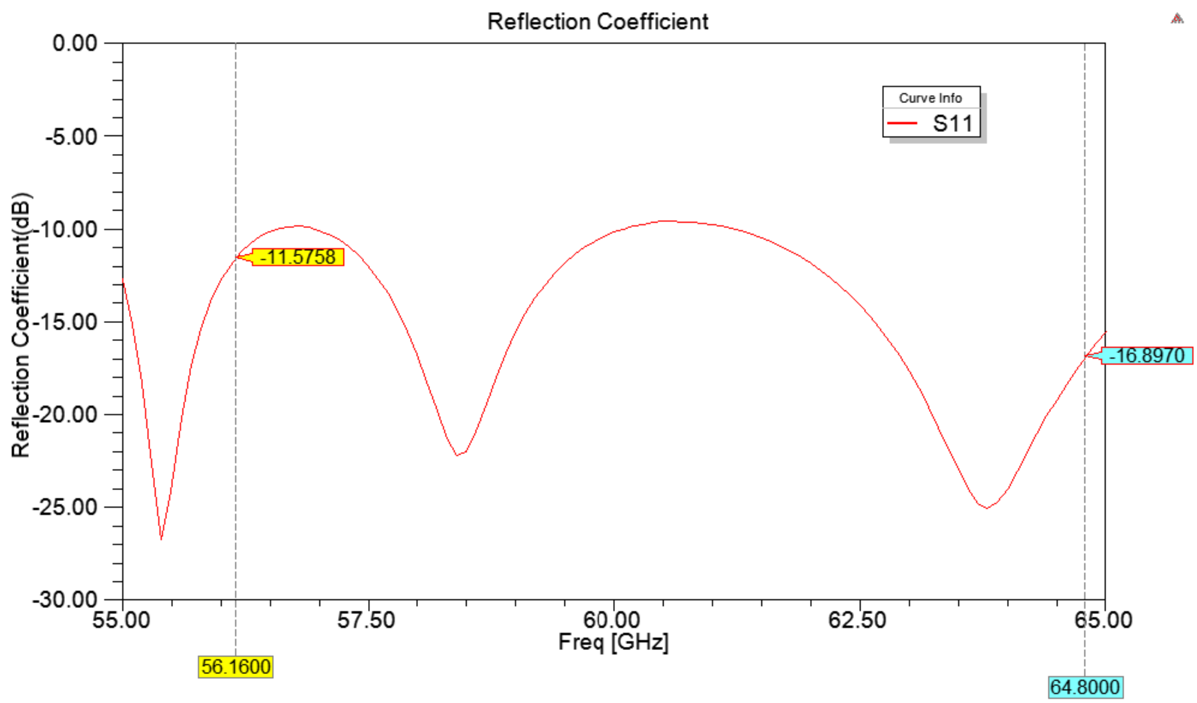


Fig. 3.1.4.2.8. Reflection Coefficients for the E-Plane Array with 762 μm and 508 μm thick substrates using the adhesive.

### 3.1.4.3 Sensitivity study

Before fabricating, a sensitivity study was performed to determine what parameters would be affected by the limits offered by the manufacturer. The manufacturer, SAE circuits, offers a 6.35 µm error in their etching. Thus a sensitivity study was performed using the array presented in sections 3.1.4.2 with the adhesive. The results of varying the Coupling aperture size, patch size and adhesive girth can be seen in figure 3.1.4.3.1. From this image it can be determined that the factor with the strongest effect is the size of the coupling apertures. These results also hint at the possibility of increasing the coupling aperture size to offset the possible fabrication error. A study of the effect of displacing the layers relative to each other was also undertaken and the results are shown in figure 3.1.4.3.2. These results showed that the array was independent to this kind of error with the error constraints provided by the company.

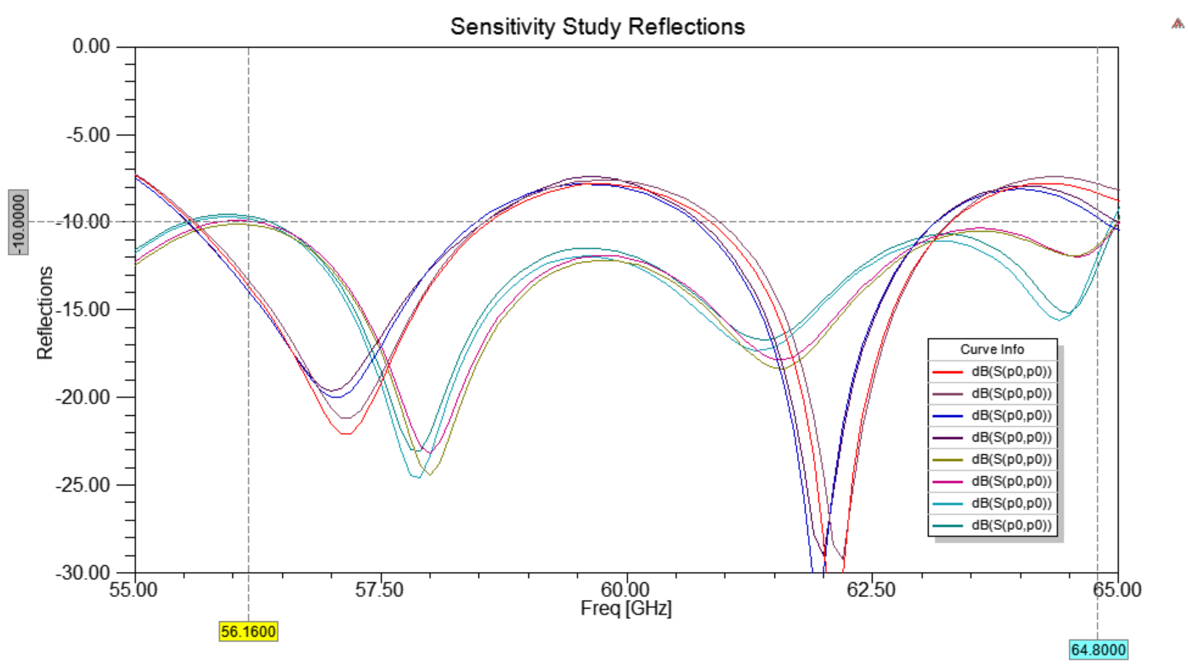


Fig. 3.1.4.3.1. Reflection coefficient for the variation in: coupling aperture size, patch size, and adhesive girth

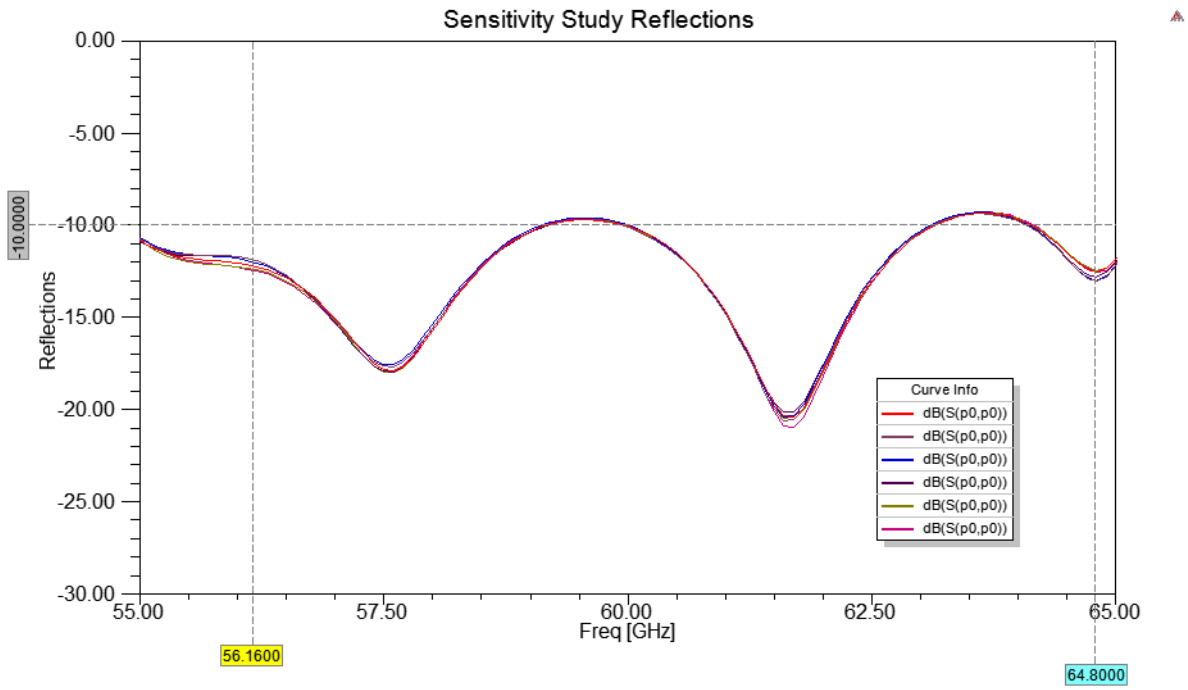


Fig. 3.1.4.3.2. Reflection coefficient for the variation in alignment

## 3.1.5 4x4 Element Array

Once the arrays individual arrays along the E and H planes had been successfully designed and the coaxial-SIW transitions designed, the complete array could be designed. In the 4x4 Array, the square cavity is resized so that the width is 9.43 mm. Figs 3.1.5.1, 3.1.5.2, and 3.1.5.3 show the bottom view for the new layers. The progression of the layers follows the same order as the layers described in section 3.1.4.1 using fig 3.1.4.1.2.

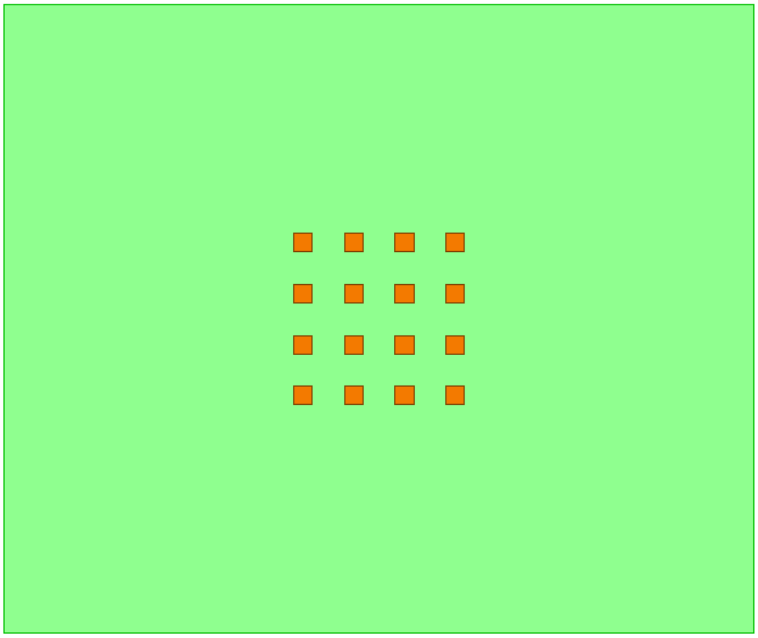

Fig. 3.1.5.1. Layer 1.  The 16 patches that are found within the cavity.

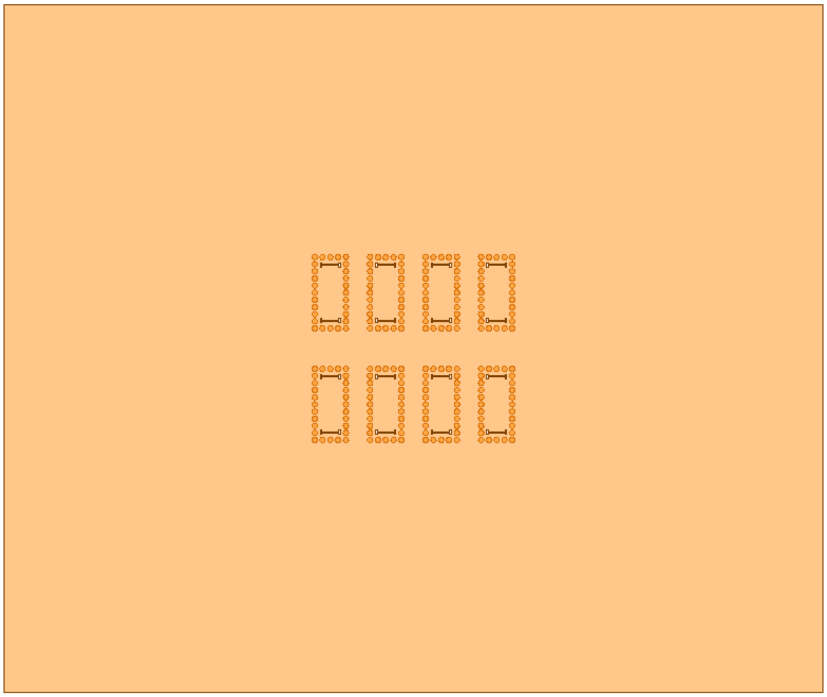

Fig. 3.1.5.2.  Layer 2.

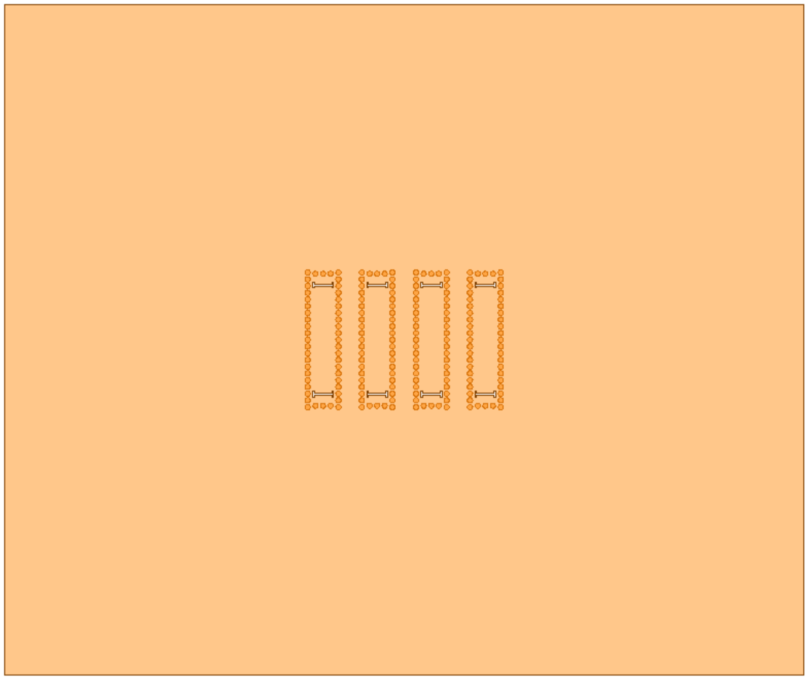

Fig. 3.1.5.3. Layer 3

The final array also includes the appropriate spacing for the coaxial connector required. The spacing was designed with the connector [26] as the connector to be used. This required creating a feed network which could uniformly excite the array while allowing the connectors enough space on the board. As with the previous arrays, two versions where created: one using only 254 µm cores in the feed network and another that incorporated 508µm and 762 µm RO3450 cores. The Layers don't change noticeably between the array. The only layer that has a dramatic change between the versions is layer 4, shown in fig 3.1.5.4 for the array using only 254 µm cores in the feed and in fig 3.1.5.5 for the array using 508 µm and 762 µm cores in the feed. The parameters for the coaxial transitions for these two can be found in section 3.4

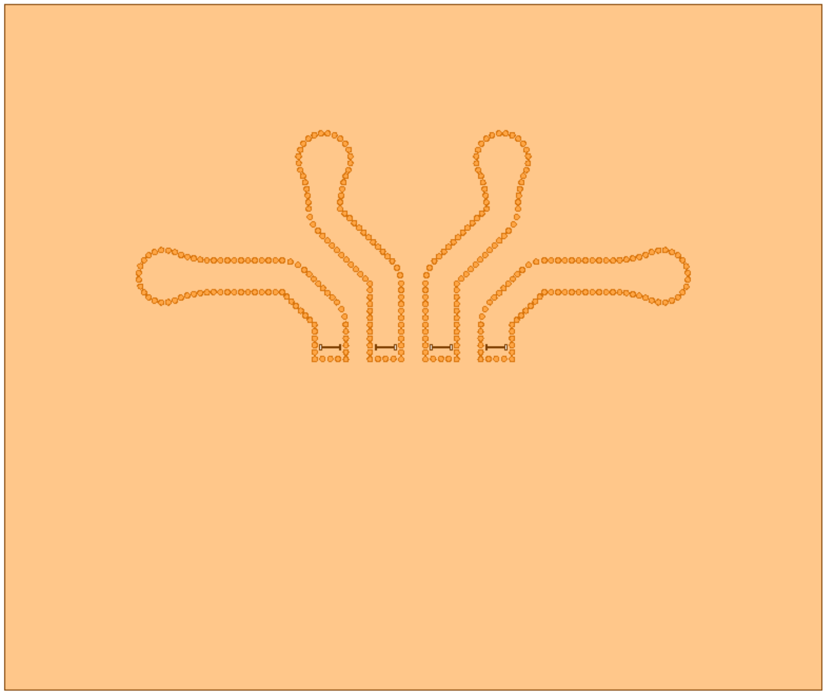

Fig. 3.1.5.4. Layer 4 for the array using 254 µm cores only.

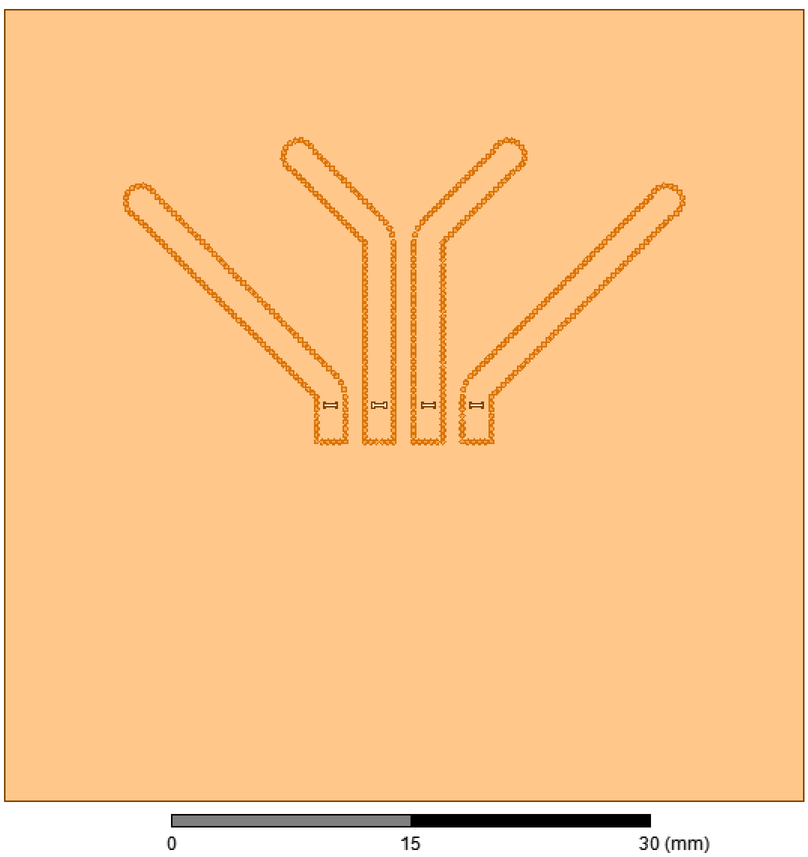


Fig. 3.1.5.5. Layer 4 for the array using 508 µm and 762 µm cores.

## 3.3 Vertical T Junctions

In order to feed the arrays presented in sections 3.1.4 and 3.1.4, a vertical power divider was designed to serve as a T-Junction. Similar to the coupling slots used in [12] and [13] the general layout can be seen in fig. 3.3.2. This T-Junction uses an H-Slot to couple 2, vertically adjacent layers. The bottom layer contains only one port and leads to the H-Slot. It is terminated with a post wall. The upper layer contains two ports. All three ports will be matched to the infinite SIW. Matching to the infinite SIW allows one to design a corporate feed using these T-Junctions without having to take into account any length-dependent impedance transformation.

The T-Junction is designed to ideally behave as a -3 dB power divider. The losses incurred are due to dielectric and conductor losses as well as SIW losses when implemented with SIW. The phase between the two even-power ports will have a 180° difference. This difference is no problem for the arrays presented in sections 3.1.3 and 3.1.5 because the spacial orientation of the radiating elements also alternates, resulting in a uniformly excited array across magnitude and phase. Figure 3.3.1 shows the ideal circuit model for the power divider. All 3 ports are equally matched. The impedance in the circuit is the slot.

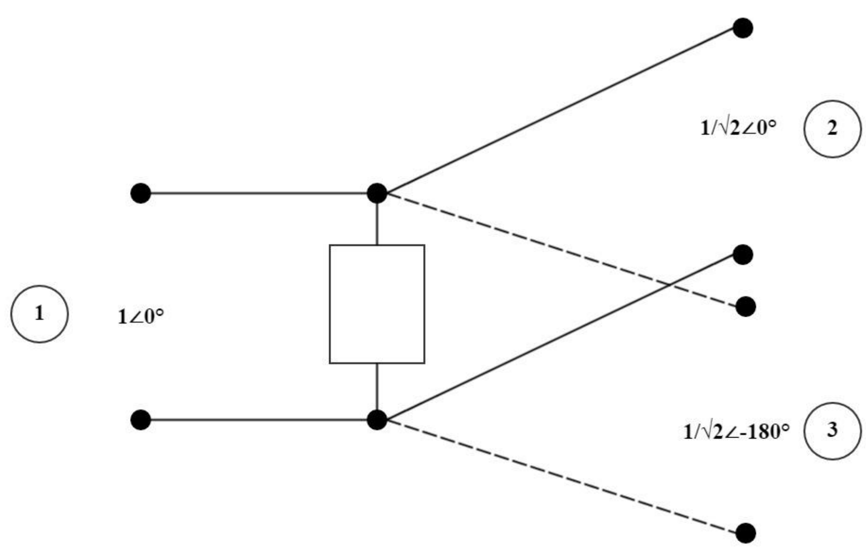


Fig. 3.3.1 Ideal S-Parameter model for this power divider.

The initial array design only required a transition from 254 µm to 254 µm RO4350 substrate. In order to accommodate the second coaxial-SIW transition described in section 3.4, T-Junctions pairing levels with different thicknesses where designed. These thicknesses where chosen from the available standard thicknesses for the substrate [27] The next sections will explain in more detail the parameters for each thickness pairing and the final design parameters can be seen summarized in table 3.3.1. The parameters used by all 4 pairings are the same. The aperture's width (*Wap*) controls the slot's thickness. The length of the slot is controlled by *Lap*. The parameter offset is measured in $\lambda_g$ units and is measured from where a solid waveguide would be sealed off to the center of the slot. $\lambda_g$ is calculated using [28] for the equivalent waveguide at the center frequency of 60.48 GHz. The widths found in table 3.3.1 are the effective widths for the SIWs. Equation (2) is used to find the real widths measured from the center of the vias. The simulation results shown in the coming sections all use solid waveguides in order to expedite simulation time and to allow flexibility when designing parametric analyses on the model.

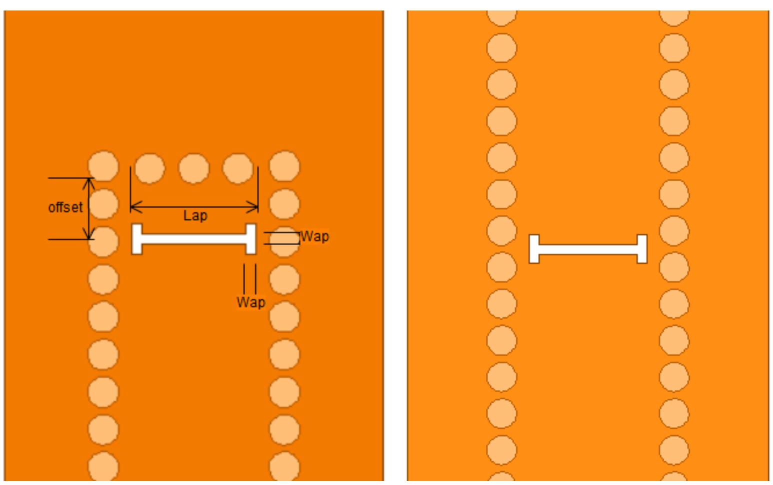


(a) (b)

Fig. 3.3.2. (a) Bottom layer which only contains one port and the aperture. (b) Top layer which contains 2 ports and the aperture.

TABLE 3.3.1 SIW FED ACMPA PARAMETERS

| **Combination** | **Lap (mm)** | **Wap (mm)** | **offset ($\lambda_g$)** | **$a_{top}$ (mm)** | **$a_{bot}$ (mm)** |
|---|---|---|---|---|---|
| 254 to 254 | 1.2 | 0.10 | 0.111 | 1.5 | 1.5 |
| 254 to 508 | 1.0 | 0.14 | 0.050 | 1.5 | 1.5 |
| 508 to 762 | 0.9 | 0.12 | 0.450 | 1.5 | 1.6 |

### 3.3.1 254 µm to 254 µm

Fig. 3. 3.1.1 shows the reflection coefficient and transmission coefficient obtained using the parameters shown in table 3.3.1 for this configuration. It is seen that the impedance is matched below -10 dB in the band of interest. It can be seen in Fig 3.3.1.1 that the transmission to both ports is not perfectly equal. The greatest difference in the band of interest occurs at 64.80 GHz where $S_{21}$ is 0.46 dB greater than $S_{31}$. The losses where worst at 56.16 GHz where they reached 1.25 dB. The phase between the ports should be -180°. The phase error shows how many degrees above or below the ports were. The most significant phase error occurs at 56.16 GHz where the phase error is 2.41°. Table 3.3.1.1 summarizes these three parameters for 56.16, 60.48, and 60.8 GHz.

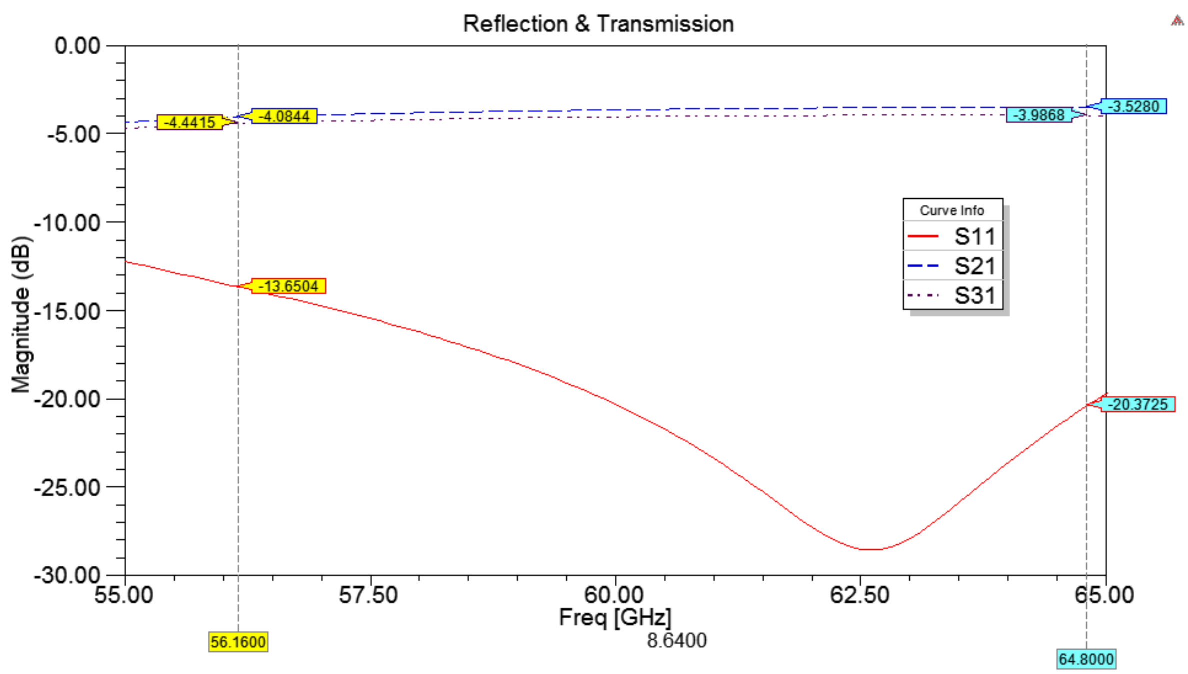


Fig. 3.3.1.1. Reflection and Transmission coefficient for the 254 µm to254 µm T-Junction

TABLE 3.3.1.1 254 TO 254 T-JUNCTION; OTHER RESULTS

| Frequency (GHz) | \|S21\| –\|S31\| (dB) | phase error (deg) | Losses (dB) |
|---|---|---|---|
| 56.16 | 0.36 | 2.41 | 1.25 |
| 60.48 | 0.39 | 0.75 | 0.81 |
| 64.80 | 0.46 | -0.32 | 0.74 |

### 3.3.2 254 µm to 508 µm

Fig. 3.3.2.1 shows the reflection coefficient and transmission coefficient obtained using the parameters shown in table 3.3.1 for this configuration. It is seen that the impedance is matched below -15 dB throughout most of the band of interest. It can be seen in Fig 3.3.2.1 that the transmission to both ports is not perfectly equal. The greatest difference in the band of interest occurs at 56.16 and 64.80 GHz where $S_{21}$ is 0.22 dB greater than $S_{31}$. The losses where worst at 56.16 GHz where they reached 1.02 dB. The most significant phase error occurs at

56.16 GHz where the phase error is 5.13°. Table 3.3.2.1 summarizes these three parameters for 56.16, 60.48, and 60.8 GHz.

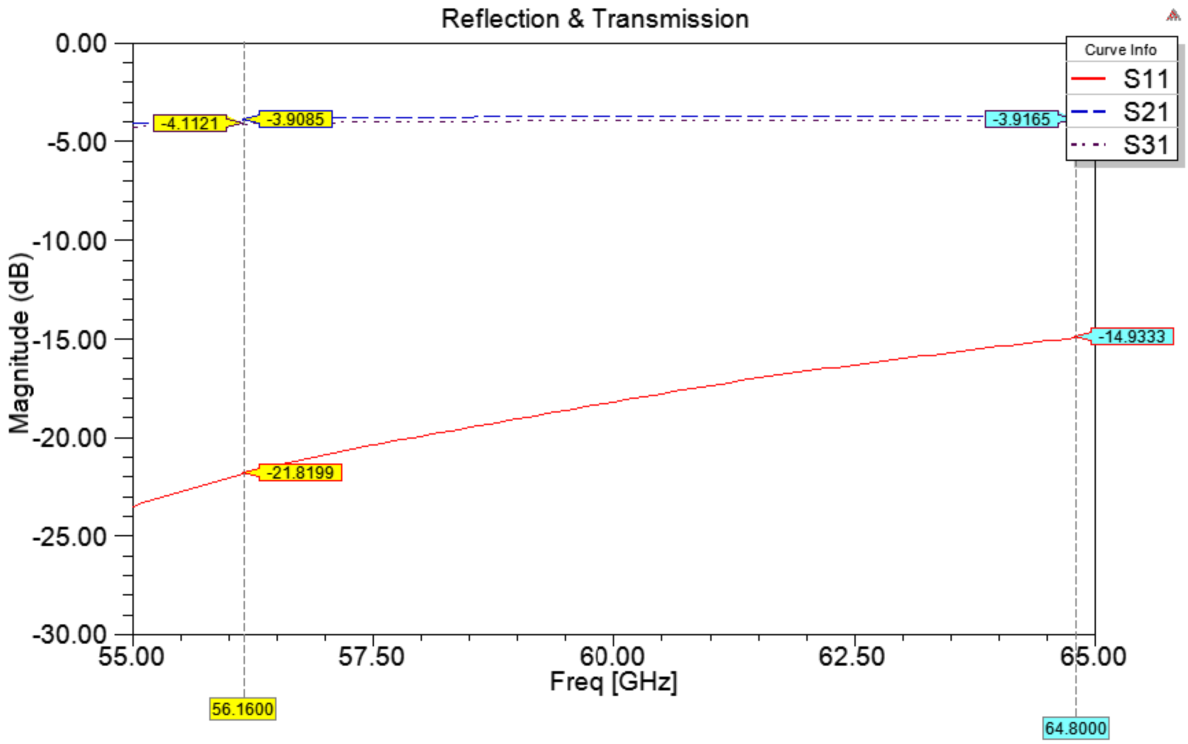


Fig. 3.3.2.1. Reflection and Transmission coefficient for the 254 μm to508 μm T-Junction

TABLE 3.3.2.1 254 TO 508 T-JUNCTION; OTHER RESULTS

| **Frequency (GHz)** | **\|S21\| –\|S31\| (dB)** | **phase error (deg)** | **Losses (dB)** |
|---|---|---|---|
| 56.16 | 0.20 | 5.13 | 1.02 |
| 60.48 | 0.22 | 2.74 | 0.81 |
| 64.80 | 0.22 | 1.60 | 0.79 |

### 3.3.3 508 μm to 762 μm

Fig. 3.3.3.1 shows the reflection coefficient and transmission coefficient obtained using the parameters shown in table 3.3.1 for this configuration. It is seen that the impedance is matched below -15 dB throughout most of the band of interest. It can be seen in Fig 3.3.3.1 that the transmission to both ports is almost equal. The greatest difference in the band of interest occurs at 56.16 GHz where $S_{21}$ is 0.22 dB below $S_{31}$. The losses where worst at 56.16 GHz where they reached 1.37 dB. The most significant phase error occurs at 60.48 GHz where the phase error is 0.95°. Table 3.3.3.1 summarizes these three parameters for 56.16, 60.48, and 60.8 GHz.

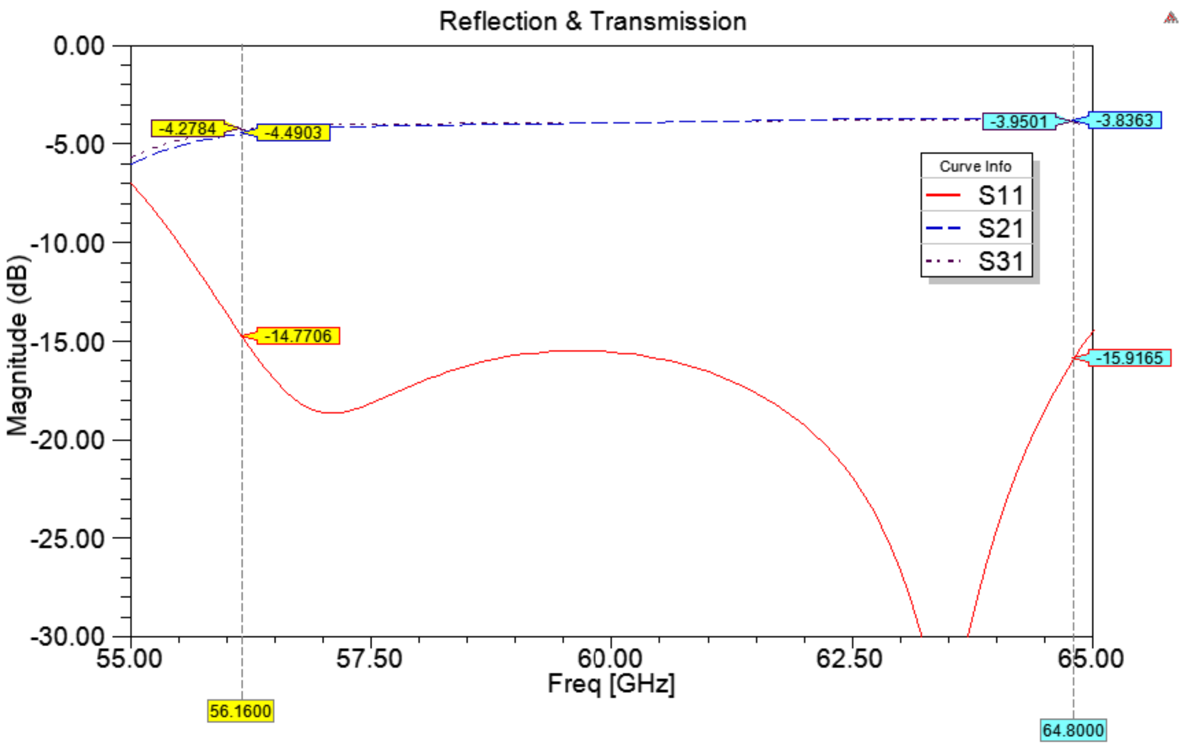


Fig. 3.3.3.1. Reflection and Transmission coefficient for the 508 µm to762 µm T-Junction

TABLE 3.3.3.1 508 TO 762 T-JUNCTION; OTHER RESULTS

| Frequency (GHz) | \|S21\| –\|S31\| (dB) | phase error (deg) | Losses (dB) |
|---|---|---|---|
| 56.16 | -0.21 | -0.14 | 1.37 |
| 60.48 | 0.00 | 0.95 | 0.89 |
| 64.80 | 0.11 | 0.24 | 0.88 |

## 3.4 Coaxial Transition

In order to measure the antennas, a transition between coaxial and SIW was created. The transition uses a circular cavity to impedance match to the SIW. The model, shown in fig 3.4.1 shows the resulting layout of the transition using solid waveguides. The architecture is achieved by combining circles of different radii. The cavity's radius is controlled by the radius *Rc*. To smoothen the transition to the rectangular waveguide, a curve is created using the radius *Rb*. Fig. 3.4.1 shows these circles in red. The mold for the solid waveguide is created by combining the points where the circle of radius *Rb* is tangent to the waveguide of width *a* and the circle of radius *Rc*. The coaxial connector is located a distance *coax_offset* from the center of the cavity. The coaxial connector used is a 1.85mm connector. The 3D view of two transitions with the waveguide converted to SIW can be seen in figures 3.4.2 and 3.4.4

Two transitions where designed; One to 254 µm thick RO4350 and another to 762 µm thick RO4350. In the 254 µm transition, the coaxial connector's pin went only halfway through the substrate. This is difficult to implement. The 762 µm transition was designed to improve on the 254µm by being thicker and allowing easier realization of this requirement, and by having the pin reside in a hole drilled all the way through the substrate instead of having to stop the drilling halfway. In this way controlled depth drilling is avoided.

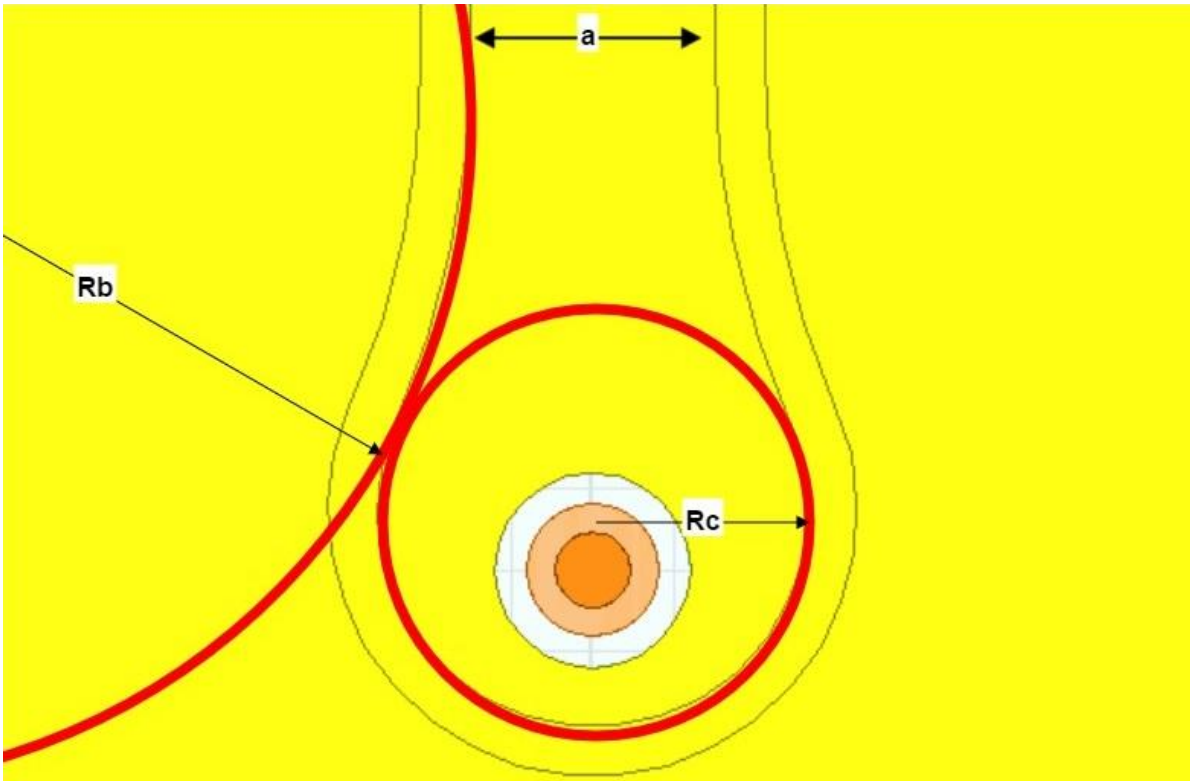


Fig. 3.4.1. Reflection and Transmission coefficient for the 508 μm to762 μm T-Junction

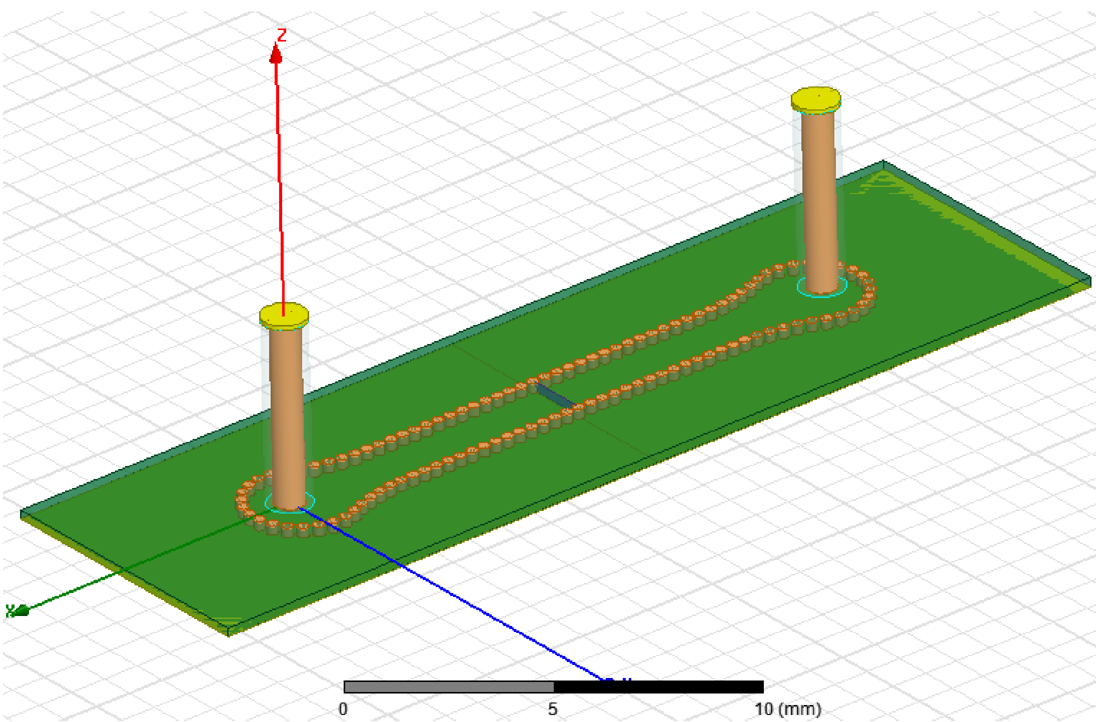


Fig. 3.4.2 Model setup for the transition to 254 μm. thick RO4350

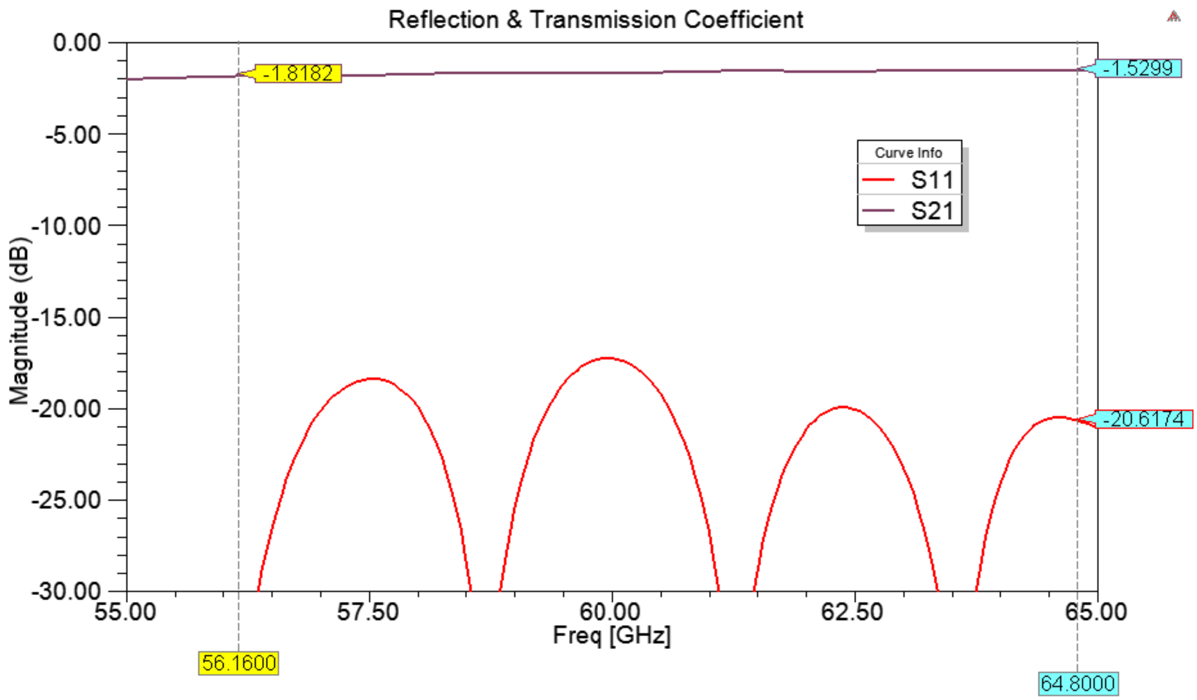


Fig. 3.4.3  Reflection and Transmission coefficient for 254 µm transition

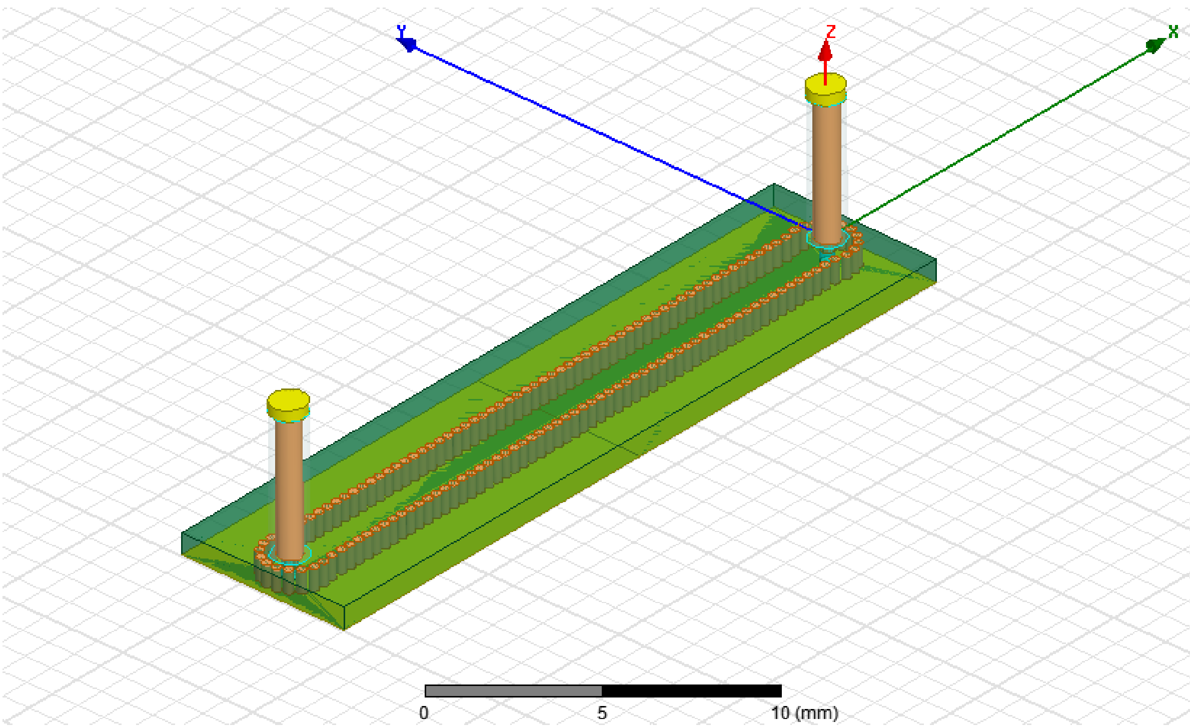


Fig. 3.4.4  Model setup for the transition to 762 µm thick RO4350

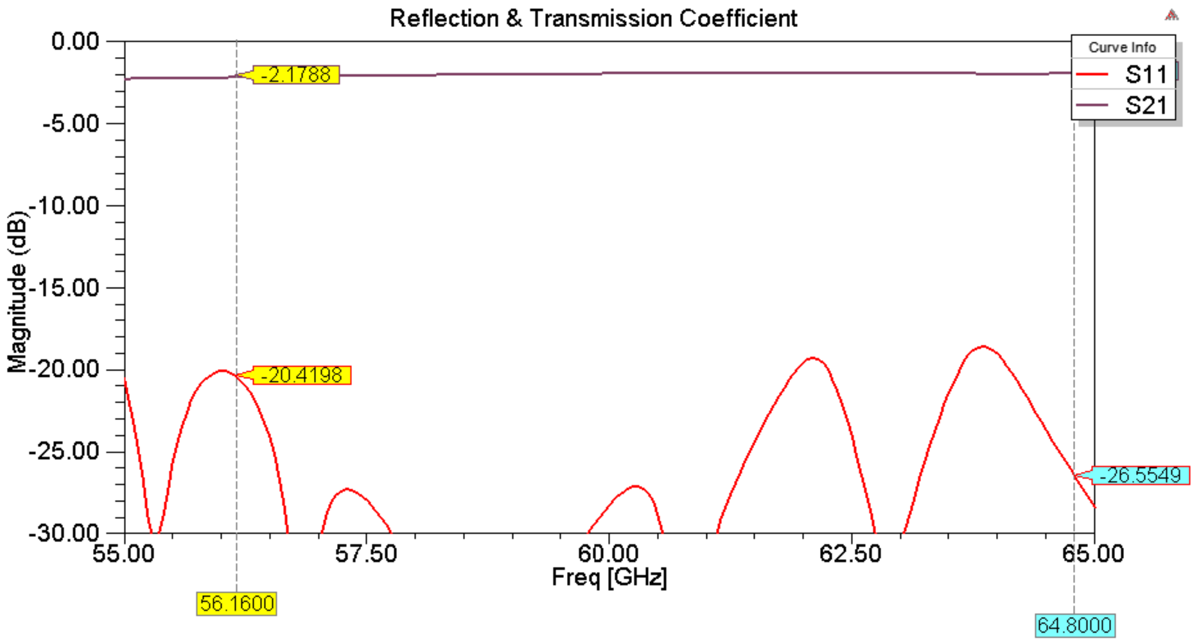


Fig. 3.4.5. Reflection and Transmission coefficients for the transition to 762 µm.

Matching the transition to the SIW means that it can be used to feed any structure that is also matched to the SIW. Both transitions successfully achieved -15 dB or less in the bandwidth of interest. The results can be seen in figures 3.4.3 and 3.4.5. The parameters for these two designs are summarized in table 3.4.1. The 762 µm transition uses a slightly wider effective waveguide width in order to match the T-Junciton described in section 3.3.3.

TABLE 3.4.1 COAXIAL TO SIW PARAMETERS

| **Parameter** | **254 µm Transition** | **762 µm Transition** |
|---|---|---|
| a | 1.5 mm | 1.6 mm |
| Rc | 1.317 mm | 0.856 mm |
| Rb | 5.270 mm | 6.849 mm |
| offset | 0.360 mm | 0.130 mm |

## 3.5 Human Body Modeling

In order to determine the antenna's viability for Body Area Network (BAN) applications, a simulation similar to the experiment carried out by [4] was created. This experiment placed an antenna on top of a skin-phantom in order to measure the antenna parameters' response. To establish a statistical significance for this result, a $2^k$ factorial design was employed. The design was a $2^k$ factorial design with 3 parameters. The parameters were: solution frequency, antenna type, and presence of skin. The solution frequency was varied in order show that the results obtained are not dependent on the frequency at which the mesh is made. Should the results be dependent on the solution frequency, this would be taken as a sign of an error in the simulation setup and the structure would have to be revised. The antenna type is changed to determine if the skin affects the single element and the array differently. If it is determined that the skin affects both types in the same way then any further modifications on the antenna need only be tested against the single element, saving on simulation time and resources. The array being used is shown in fig 3.1.3.1. The single element can be seen in fig 3.1.2.1. These two versions of the antenna were chosen because of their relative simplicity compared to the final 4x4 antenna array.

Independence to the presence of skin would be ideal because it would allow only designing the free-space design of the antenna and using it, without further modifications, for on-skin applications. We have decided to use a homogeneous skin model to model the human body. The homogeneous model was demonstrated to be enough in [2] because the strong absorption in the skin impedes interaction with the layer of fat below the dermis. In order to model the skin within HFSS a material with the appropriate properties has been defined. The properties were calculated using [29] which builds upon the work of [30 – 31] and others to determine the appropriate parameters as a function of frequency. Table 3.5.1 shows an example of 10 frequency points sampled from 50 to 70 GHz to demonstrate how the parameters change. The actual model will use more frequency points.

TABLE 3.5.1 ELECTRIC PROPERTIES OF SKIN

| Tissue name | Frequency \|GHz\| | Conductivity \|S/m\| | Relative permitivity | Loss tangent | Wavelength \|mm\| | Penetration depth \|mm\| |
|---|---|---|---|---|---|---|
| Dry Skin | 50 | 34.619 | 9.4021 | 1.3237 | 1.6959 | 5.4216 |
| | 52 | 35.04 | 9.0634 | 1.3364 | 1.6577 | 5.2692 |
| | 54 | 35.424 | 8.7544 | 1.347 | 1.6216 | 5.1305 |
| | 56 | 35.777 | 8.4718 | 1.3556 | 1.5876 | 5.0037 |
| | 58 | 36.1 | 8.2129 | 1.3623 | 1.5552 | 4.8875 |
| | 60 | 36.397 | 7.9753 | 1.3673 | 1.5245 | 4.7805 |
| | 62 | 36.671 | 7.7567 | 1.3707 | 1.4952 | 4.6817 |
| | 64 | 36.925 | 7.5554 | 1.3727 | 1.4672 | 4.5902 |
| | 66 | 37.159 | 7.3695 | 1.3733 | 1.4404 | 4.5052 |
| | 68 | 37.376 | 7.1976 | 1.3727 | 1.4148 | 4.4262 |
| | 70 | 37.577 | 7.0383 | 1.371 | 1.3902 | 4.3524 |

Figure 3.5.1 shows the skin model placed below the single element antenna. The block of skin is 5 mm thick which according to [2] is enough for almost complete power dissipation within the skin. The antenna is placed directly on top of the skin model without leaving any space in between.

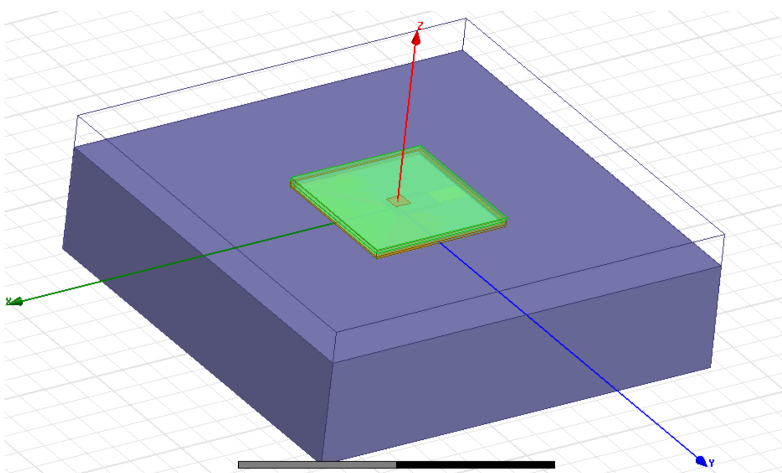


**Figure 3.5.1**. Single antenna with rectangular skin model.

The observed outputs would be: the bandwidth, the radiation pattern gain, and the front-to-back (FB) ratio. The bandwidth was determined by observing the reflection coefficient within the frequencies of interest (56.16GHz to 64.8GHz). The value for this response was capped at 8.64GHz which implies that the antenna has met the full minimum requirements for bandwidth. The antenna's Gain and FB ratio were measured at the center frequency.

## 3.6 Rotman Lens

The Rotman lenses tested where designed following the design in [22]. Figures 3.6.1 and 3.6.2 show the outline and information calculated for one of the Rotman lenses. The antenna port width is the width of the waveguide including the width of the vias that make up the SIW wall. *ETA_max*, and the normalized version *eta_max*, correspond to $\eta$ in the equations of [22]. Keeping this value small keeps the phase errors small. *Theta_max* corresponds to angle of the most off-center beam port and phi corresponds to the maximum scan angle. [22] provides a calculation for $F_{min}$, however this was only useful as an initial value. In order to accommodate the ports the size of the overall lens was increased by manually setting the value of F once the lens parameters had been determined. The wording "successful Lens Layout" implies that the ports don't overlap. *d* is the separation of the array elements in the array and is calculated using equation (3).

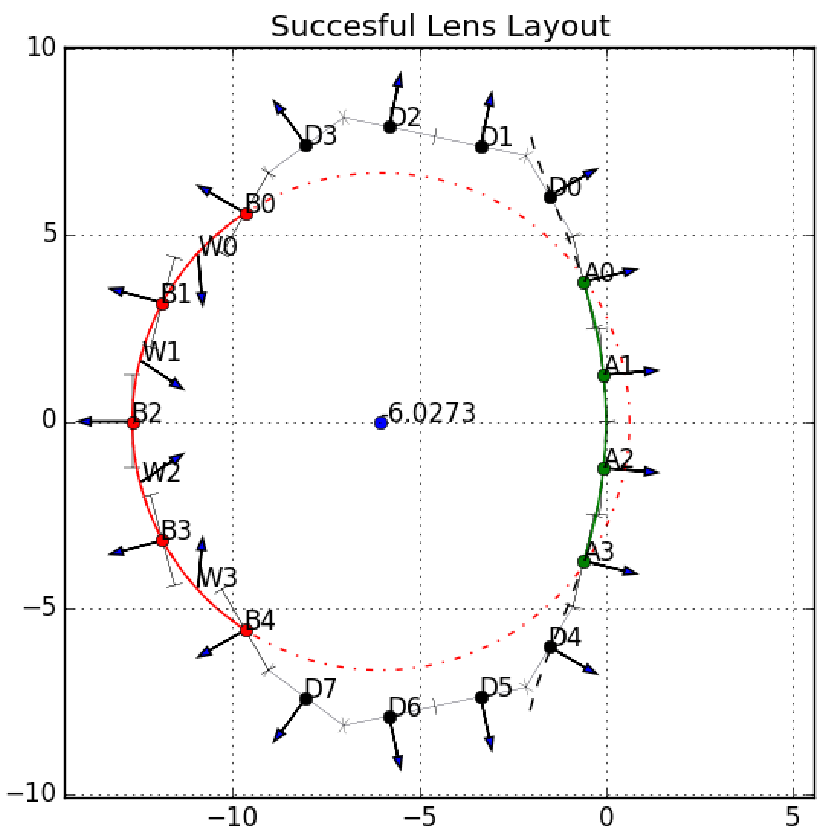


Fig. 3.6.1 Outline for the Rotman lens to be designed

```
antenna_port_width = 2.497mm
ETA_max = 5.579mm, (eta_max = 0.500)
theta_max = 30deg
phi = 40deg
Fmin = 9.240mm
F = 11.157mm
F/Fmin = 1.208
G = 12.686mm, (g = 1.137)
R = 6.659mm
d = 3.080mm
B0 = (-9.663, 5.579)mm, n(-0.866, 0.500)
B1 = (-11.876, 3.182)mm, n(-0.966, 0.259)
B2 = (-12.686, 0.000)mm, n(-1.000, 0.000)
B3 = (-11.876,-3.182)mm, n(-0.966,-0.259)
B4 = (-9.663,-5.579)mm, n(-0.866,-0.500)
A0 = (-0.598, 3.738)mm, n( 0.973, 0.230) w0 = 2.348mm
A1 = (-0.068, 1.249)mm, n( 0.997, 0.081) w1 = 2.321mm
A2 = (-0.068,-1.249)mm, n( 0.997,-0.081) w2 = 2.321mm
A3 = (-0.598,-3.738)mm, n( 0.973,-0.230) w3 = 2.348mm
D0 = (-1.510, 6.033)mm, n( 0.865, 0.501)
D1 = (-3.358, 7.370)mm, n( 0.205, 0.979)
D2 = (-5.803, 7.881)mm, n( 0.205, 0.979)
D3 = (-8.031, 7.399)mm, n(-0.592, 0.806)
D4 = (-1.510,-6.033)mm, n( 0.865,-0.501)
D5 = (-3.358,-7.370)mm, n( 0.205,-0.979)
D6 = (-5.803,-7.881)mm, n( 0.205,-0.979)
D7 = (-8.031,-7.399)mm, n(-0.592,-0.806)
```

Fig. 3.6.2 Calculated values for the Rotman lens

The beam ports, labeled B0 through to B4, reside on the focal arc that is calculated using *G, F,* and *theta_max*. This focal arc is part of a circle whose center is marked in blue in figure 3.6.1 and whose radius is *R.* The beam ports located in this focal arc are directed at the origin through which the inner lens countour crosses. The smaller arrous perpendicular to the port's width in figure 3.6.1 are simply unit normal vectors to show what direction the port would aim in.

Calculating the inner lens contour to position the antenna ports, labeled A0 to A3, requires sovling various equations found in [22]. Equation (7) in [22] is missing a term and is included here as equation (10) to demonstrate the corrected form. The unit normals for the antenna ports are calculted in such a way that the port is perpendicular to its position on the inner lens contour. Following the style in [22], the equations to calculate the inner lens contour will now be presented.

$$\eta = \frac{N}{F},\ x = \frac{X}{F},\ y = \frac{Y}{F},\ \omega = \frac{W - W_0}{F},\ g = G/F \tag{4}$$

$$a_0 = \cos(\alpha),\ b_0 = \sin(\alpha),\ a_1 = \cos(\varphi),\ b_1 = \sin(\varphi) \tag{5}$$

$$y = \frac{b_1}{b_0\sqrt{\varepsilon_r}}\eta(1-\omega) \tag{6}$$

$$x^2 + y^2 + 2gx = \omega^2 - 2g\omega \tag{7}$$

$$a\omega^2 + b\omega + c = 0 \tag{8}$$

$$a = 1 - \eta^2\left(\frac{b_1}{b_0}\right)^2 - \left(\frac{g-1}{g-a_0}\right)^2 \tag{9}$$

$$b = 2g\frac{g-1}{g-a_0} - \frac{b_1^2\eta^2(g-1)}{(g-a_0)^2\varepsilon_r} + \frac{2\eta^2}{\varepsilon_r}\left(\frac{b_1}{b_0}\right)^2 - 2g \tag{10}$$

$$c = \frac{b_1^2\eta^2 g}{(g-a_0)\varepsilon_r} - \frac{(b_1\eta)^4}{4{\varepsilon_r}^2(g-a_0)^2} - \frac{\eta^2}{\varepsilon_r}\left(\frac{b_1}{b_0}\right)^2 \tag{11}$$

Eq (4) normalizes the design parameters using the Focal length *F*. Eq (5) assigns the sine and cosine for the two design angles to variables for simpler notation. Simultaneous solutions of equations (6), (7) and (8) yield the set of x,y pairs that make up the inner lens contour. The delays $\omega$ are also calculated. These delays allow the curved wave-front to become a planar wave front in order to excite a linear array. These delays are labeled as the lowercase *w0, w1, w2,* and *w3* in figure 3.6.2 and appear next to their corresponding antenna port.

Once the antenna ports and beam ports are set the dummy ports are set. The purpose of the dummy ports is to absorb any scattering within the lens to avoid this scattering being received at a different port, causing phase and amplitude errors. Finally, via walls are place between the beam ports to close off the lens.

# CHAPTER 4

# RESULTS

## 4.1 4X4 ARRAYS

### 4.1.1 Array With 254 µm Thick Cores

The results for the reflection coefficient for the array using 254 µm cores in the feed is seen in figure 4.1.1.1. The array manages to comply with the 14.2% bandwidth as it remains below -10 dB in the bandwidth of interest. The radiation patterns can be seen in figures 4.1.1.2, 4.1.1.3 and 4.1.1.4. The results for 56.16, 60.48, and 64.8 GHz are summarized in table 4.1.1.1. The results where split into H-Plane and E-Plane due to the asymmetry of the design along each plane.

Fig 4.1.1.5 shows the result of the beam steering. The progressive phase (*delta*) between the array's ports was varied to see how the radiation pattern behaved in the H-Plane. Only the H-Plane need be examined as the array is uniformly excited along the E-Plane. The value of *delta* and how it affects the main lobe can be seen summarized in table 4.1.1.2

The array managed to meet the -10 dB bandwidth requirements and a beamwidth greater than 20° along the H-Plane, where the beam steering would occur. The array is also capable of successfully steering the main beam when fed with a progressive phase. Due to the lossy charachteristics of the substrate, the Gain fell somewhat short of the 17 dBi goal but when compared to the plots of fig. 3.1.1.1, the 15.51 dBi obtained at 56.16 still means the antenna is good to be used for 60 meters; slightly more if a higher frequency channel in the band is used. The beam steering capabilities of the array where successfully demonstrated

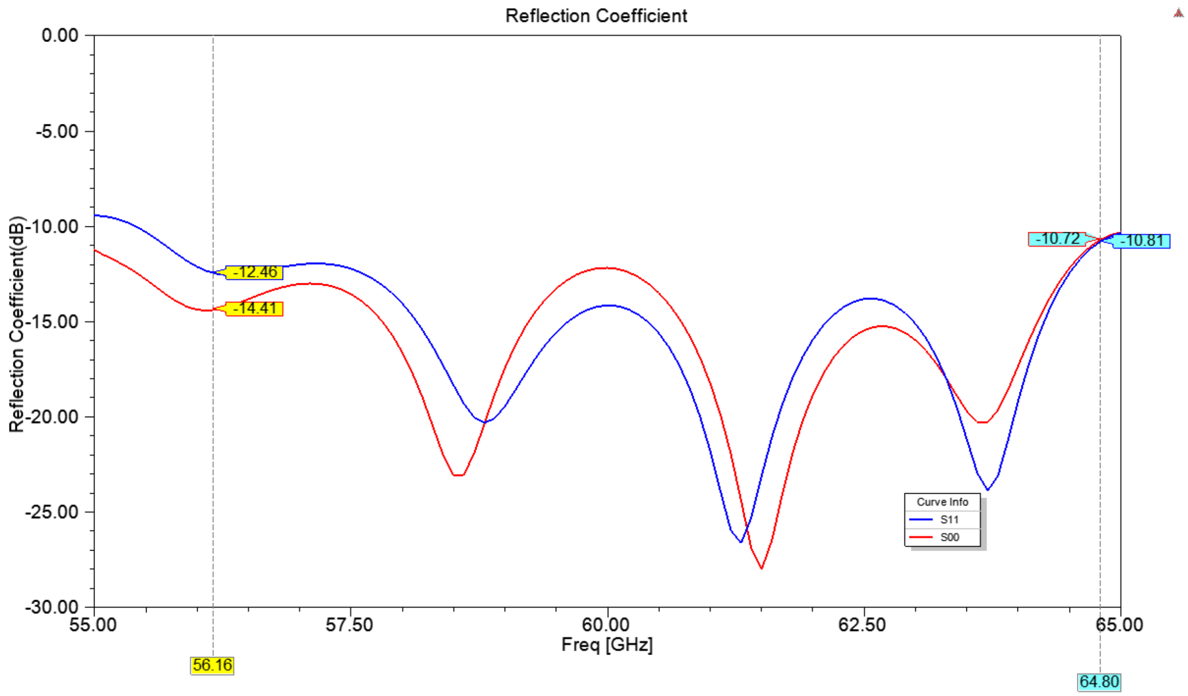


Fig. 4.1.1.1 Reflection Coefficient for the 4x4 Array using 254µm cores in the feed.

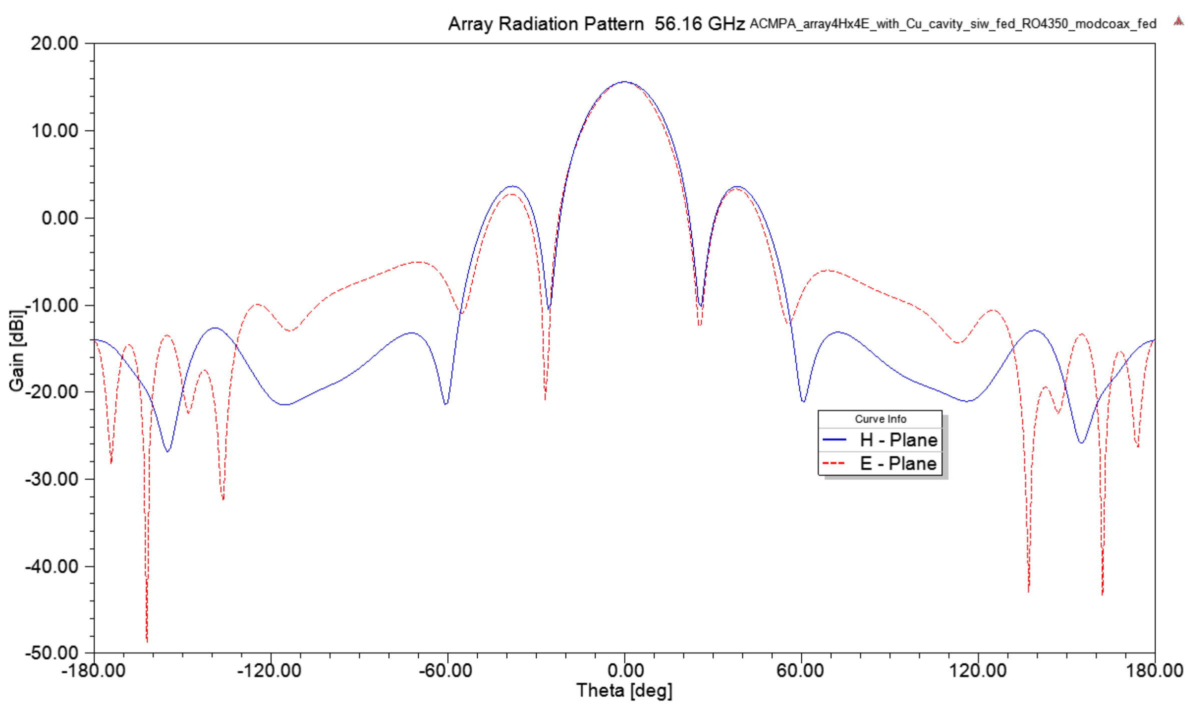


Fig. 4.1.1.2 Radiation pattern for 4x4 Array using 254 µm cores in the feed at 56.16 GHz

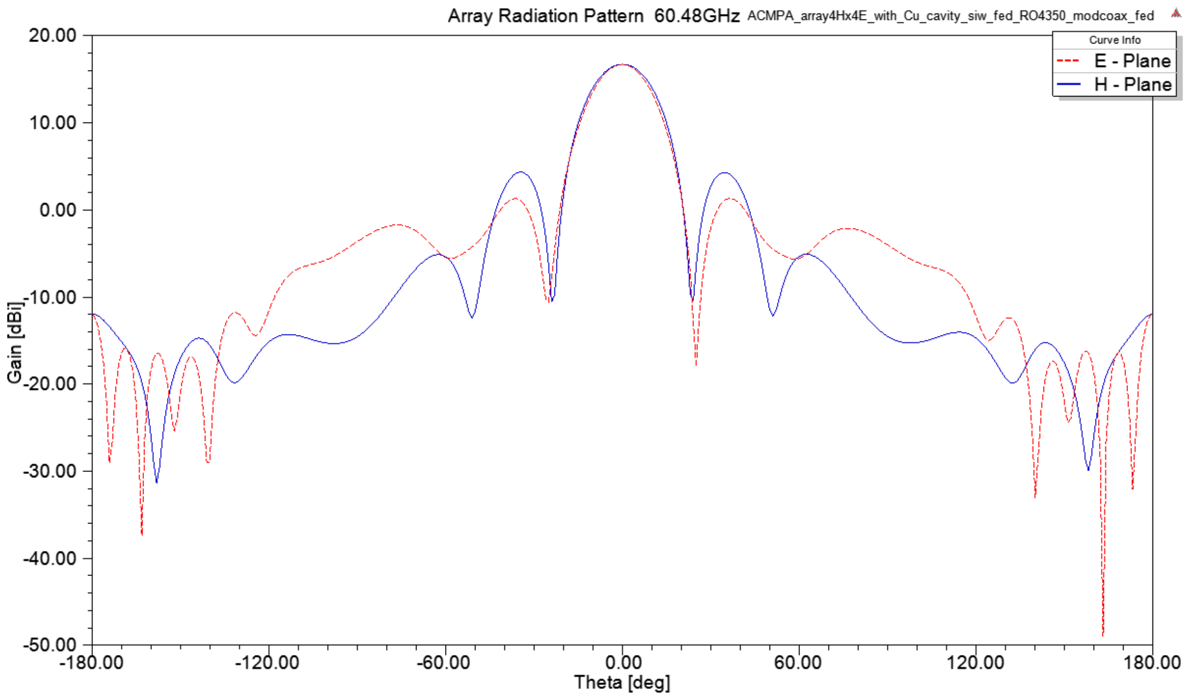


Fig.4.1.1.3. Radiation pattern for 4x4 Array using 254 µm cores in the feed at 60.48 GHz

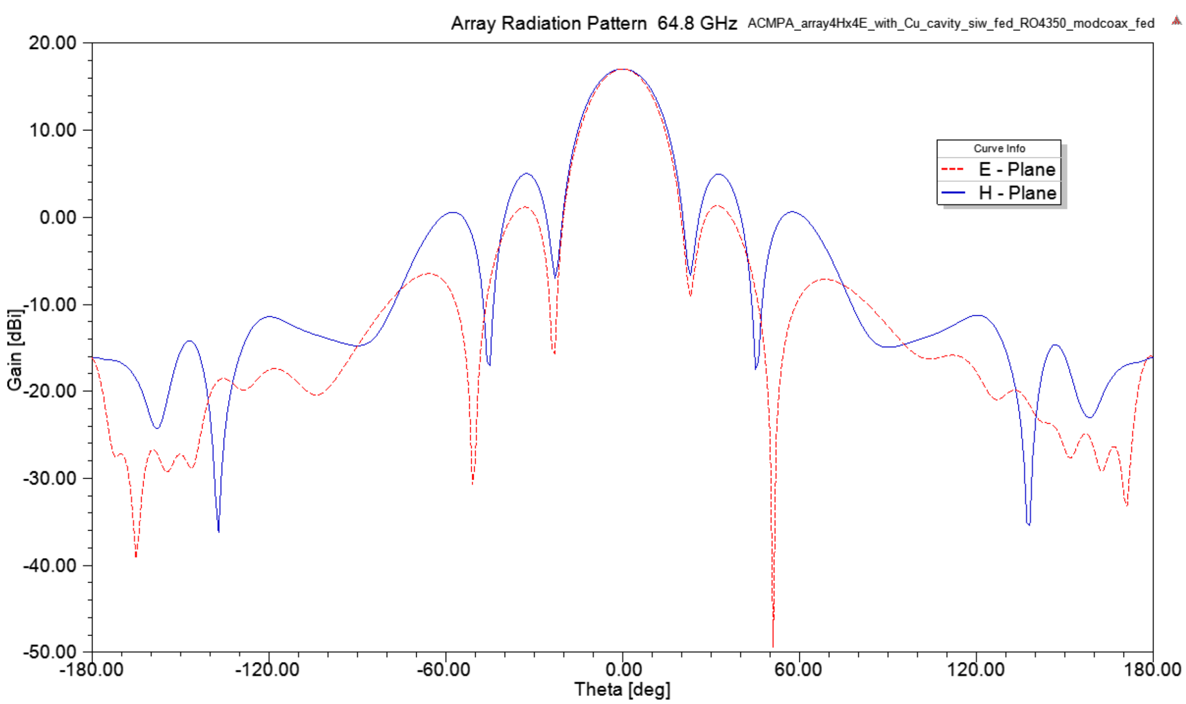


Fig. 4.1.1.4. Radiation pattern for 4x4 Array using 254 µm cores in the feed at 64.8 GHz

TABLE 4.1.1.1 SUMMARY FOR 254 ARRAY

| | | | |
|---|---|---|---|
| **Frequency (GHz)** | 56.16 | 60.48 | 64.8 |
| **Gain (dBi)** | 15.51 | 16.63 | 16.94 |
| **Directivity (dBi)** | 18.41 | 19.04 | 19.13 |
| **Efficiency (%)** | 74.83 | 78.58 | 80.33 |
| **E-Plane-3 dB Beamwidth (deg)** | 20.74 | 19.38 | 19.75 |
| **H-Plane -3 dB Beamwidth (deg)** | 22.48 | 21.05 | 21.45 |
| **E-Plane SLL (dB)** | 12.28 | 15.39 | 15.76 |
| **H-Plane SLL (dB)** | 11.95 | 12.37 | 12.03 |

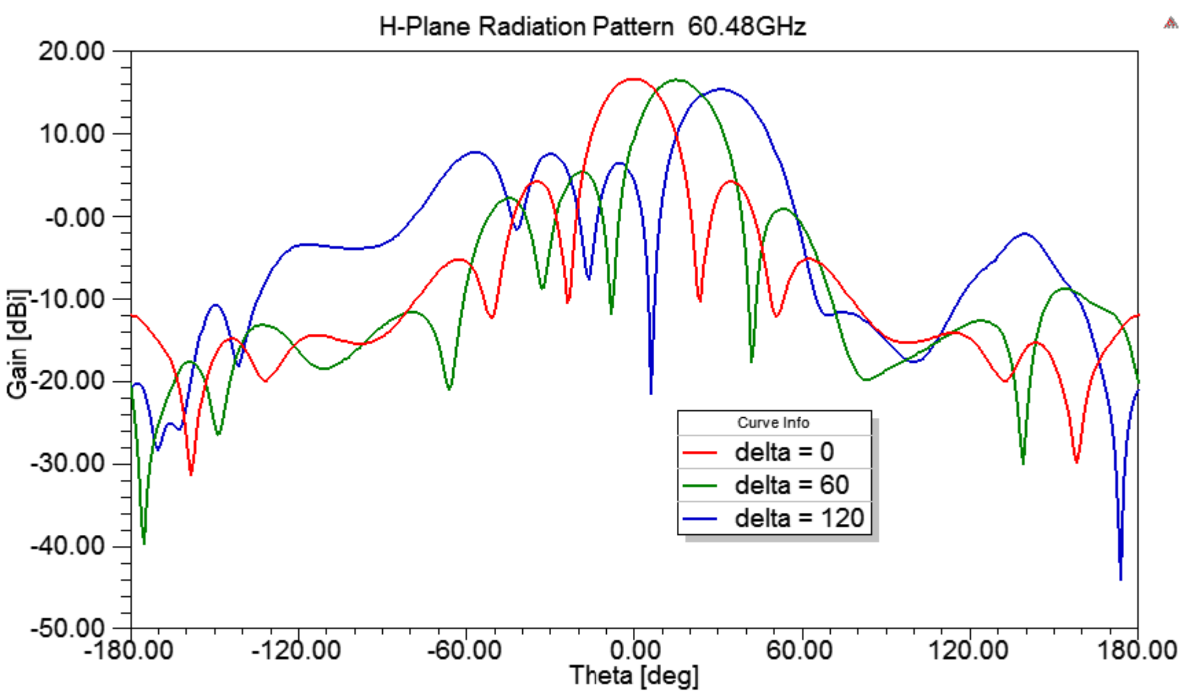


Fig. 4.1.1.5. Radiation pattern for 4x4 Array using 254 µm cores in the feed at 64.8 GHz

TABLE 4.1.1.2 SUMMARY FOR 254 ARRAY BEAM SCANNING

| Delta | Main Lobe Angle | Gain (dBi) |
|---|---|---|
| 0° | 0° | 16.63 |
| 60° | 15° | 16.51 |
| 120° | 31° | 15.37 |

### 4.1.2 Array With 508 µm and 762 µm Thick Cores

The results for the reflection coefficient for the array using 254 µm cores in the feed is seen in figure 4.1.2.1. The array manages to comply with the 14.2% bandwidth as it remains below -10 dB in the bandwidth of interest. The radiation patterns can be seen in figures 4.1.2.2, 4.1.2.3, and 4.1.2.4. The results for 56.16, 60.48, and 64.8 GHz are summarized in table 4.1.2.1. The results where split into H-Plane and E-Plane due to the asymmetry of the design along each plane.

Fig 4.1.2.5 shows the result of the beam steering. The progressive phase (*delta*) between the array's ports was varied to see how the radiation pattern behaved in the H-Plane. Only the H-Plane need be examined as the array is uniformly excited along the E-Plane. The value of *delta* and how it affects the main lobe can be seen summarized in table 4. 4.1.2.2

The array managed to meet the -10 dB bandwidth requirements and a beamwidth greater than 20° along the H-Plane, where the beam steering would occur. The array is also capable of successfully steering the main beam when fed with a progressive phase. Due to the lossy characteristics of the substrate, the Gain fell somewhat short of the 17 dBi goal but when compared to the plots of 3.1.1.1, the 14.64 dBi obtained at 56.16 still means the antenna is good to be used for 51 meters; slightly more if a higher frequency channel in the band is used. The cross polarization ratio also shows a very good linear polarization with a cross polarizion greater than 50dB in the main lobe. The beam steering capabilities of the array where successfully demonstrated

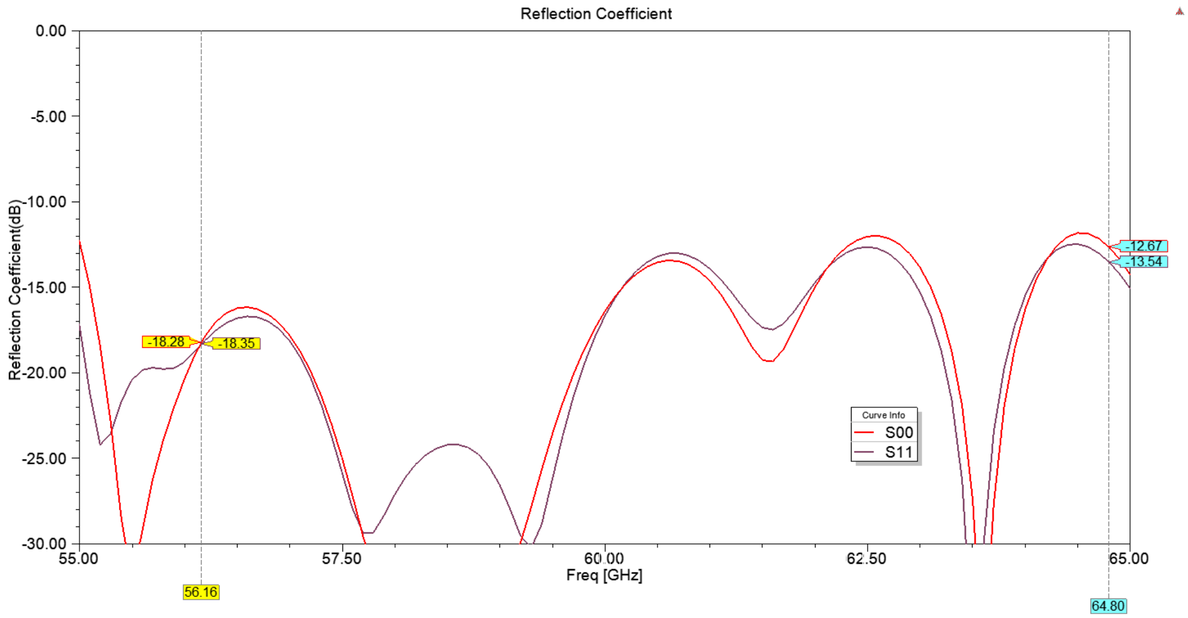


Fig. 4.1.2.1 Reflection Coefficient for the 4x4 Array using 254µm cores in the feed.

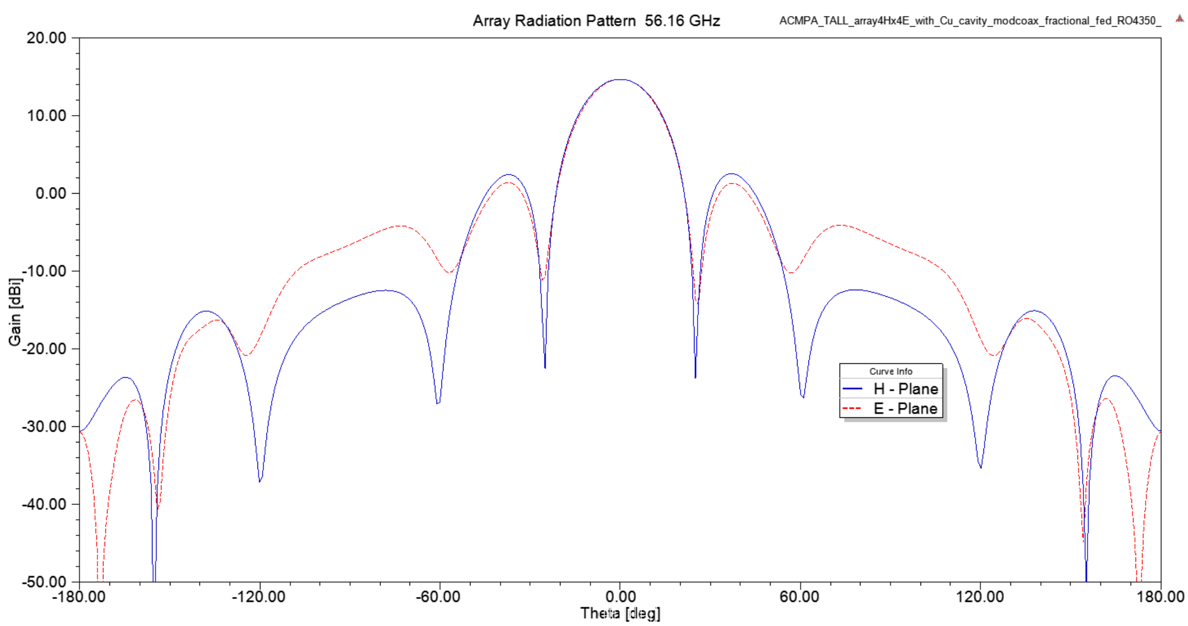


Fig. 4.1.2.2 Radiation pattern for 4x4 Array using 508 µm and 762 µm cores. in the feed at 56.16 GHz

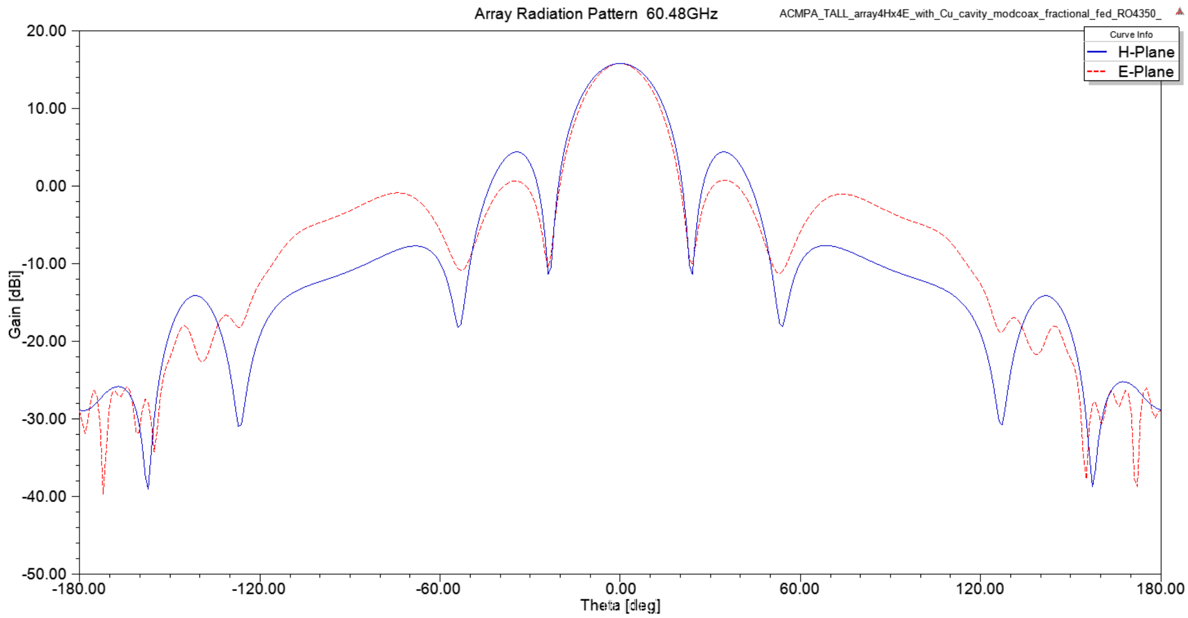


Fig.4.1.2.3 Radiation pattern for 4x4 Array using 508 µm and 762 µm cores. in the feed at 60.48 GHz

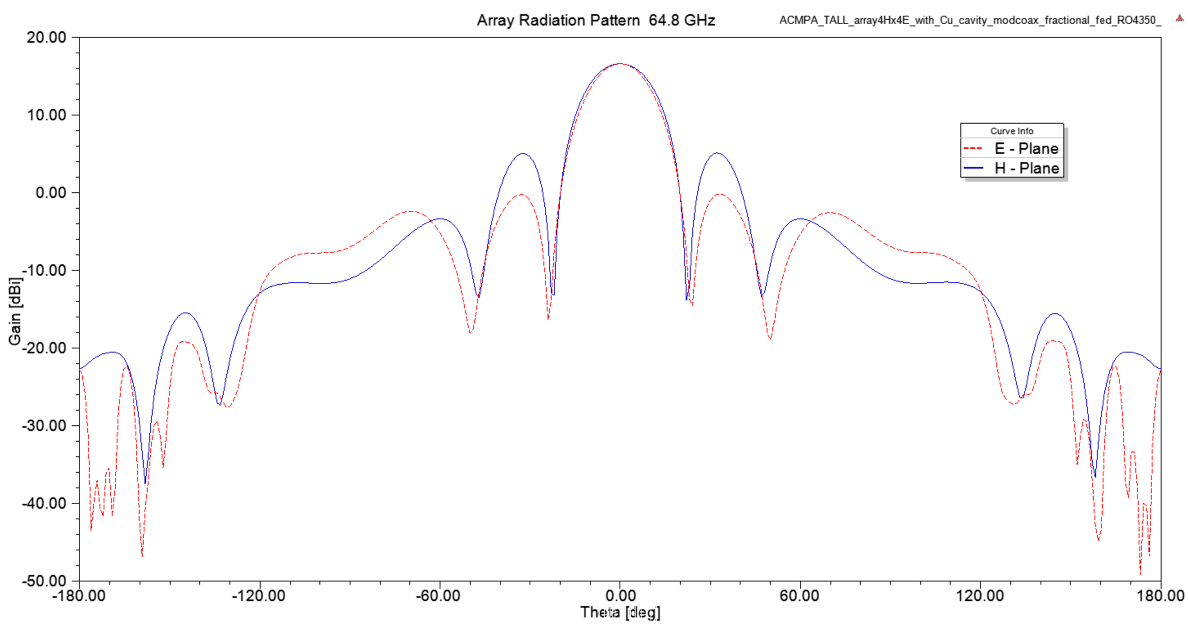


Fig. 4.1.2.4 Radiation pattern for 4x4 Array using 508 µm and 762 µm cores. in the feed at 64.8 GHz

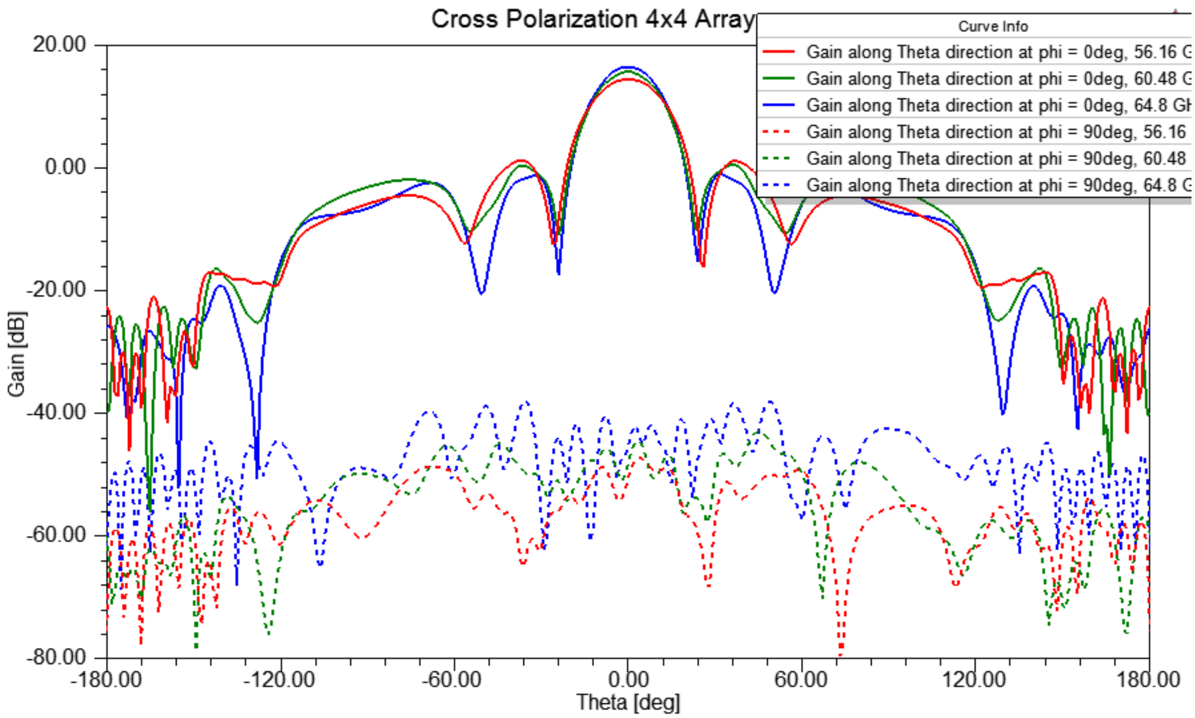


Fig. 4.1.2.5 Polarization Ratio for the 4x4 Element Array.

TABLE 4.1.2.1 SUMMARY FOR 508 AND 762 ARRAY RADIATION PATTERN.

| **Frequency (GHz)** | 56.16 | 60.48 | 64.8 |
|---|---|---|---|
| **Gain (dBi)** | 14.64 | 15.76 | 16.55 |
| **Directivity (dBi)** | 18.17 | 18.75 | 19.15 |
| **Efficiency (%)** | 70.26 | 74.16 | 77.11 |
| **E-Plane-3 dB Beamwidth (deg)** | 22.31 | 19.92 | 19.4 |
| **H-Plane -3 dB Beamwidth (deg)** | 23.01 | 22.11 | 21.41 |
| **E-Plane SLL (dB)** | 13.27 | 15.02 | 16.79 |
| **H-Plane SLL (dB)** | 12.13 | 11.41 | 11.5 |

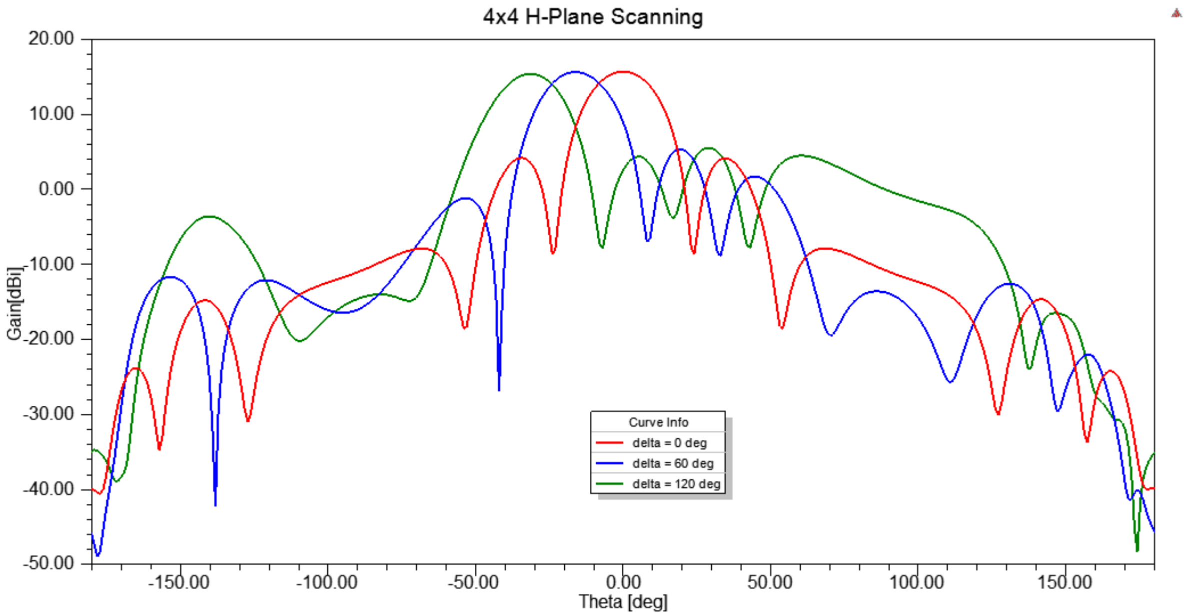


Fig. 4.1.2.6 Radiation pattern for 4x4 Array using 508 µm and 762 µm cores in the feed at 64.8 GHz

TABLE 4.1.2.2 SUMMARY FOR 508 AND 762 ARRAY BEAM SCANNING

| Delta | Main Lobe Angle | Gain (dBi) |
|---|---|---|
| 0° | 0° | 15.62 |
| 60° | -15° | 15.55 |
| 120° | -31° | 15.33 |

## 4.2 Human body

| Std | Run | Factor 1 A:Solution Fr... GHz | Factor 2 B:Antenna T... | Factor 3 C:Presence ... | Response 1 Bandwidth GHz | Response 2 Gain dB | Response 3 FB ratio dB |
|---|---|---|---|---|---|---|---|
| 1 | 2 | 60.48 | Single | No | 8.64 | 5.5835 | 15.7107 |
| 2 | 6 | 65 | Single | No | 8.64 | 5.5768 | 15.7611 |
| 3 | 5 | 60.48 | Array | No | 8.64 | 11.8806 | 17.8856 |
| 4 | 3 | 65 | Array | No | 8.64 | 11.8983 | 17.6844 |
| 5 | 1 | 60.48 | Single | Yes | 8.64 | 5.3038 | 31.0048 |
| 6 | 8 | 65 | Single | Yes | 8.64 | 5.3007 | 30.6952 |
| 7 | 4 | 60.48 | Array | Yes | 8.64 | -13.059 | 17.5559 |
| 8 | 7 | 65 | Array | Yes | 8.64 | 11.514 | 24.2702 |

**Figure 4.2.1** Response data for each case.

The analysis for bandwidth showed that, within the band of interest from 56.16GHz to 64.8GHz, the bandwidth remains unaffected by the factors analyzed. This is an excellent result which indicates that the input impedance suffers no significant change in response to the factors and no added matching network is required when using the antenna for on-skin applications. The analysis for the gain showed dependence on the Antenna Type parameter. The Gain was expected to be dependent of the Antenna type because of the quantity of elements radiating which between single and 4 elements is a rate of 1:4 of energy radiated.

The only factor that was skin dependant was the FB ratio. The Analysis for the FB ratio shows only a dependence on the presence of skin and the interaction of the presence of skin with the type of antenna. The FB ratio was expected to change significantly due to the presence of skin because the skin absorbs most of the backwards radiated energy. Fig 4.2.2 shows the half-normal plot for the FB ratio. An analysis of variance on the selected factors yields a P-value of 0.0110 for significance of the presence of skin. The interaction of the presence of skin with the type of antenna was also somewhat significant, yielding a P-value of 0.0491.

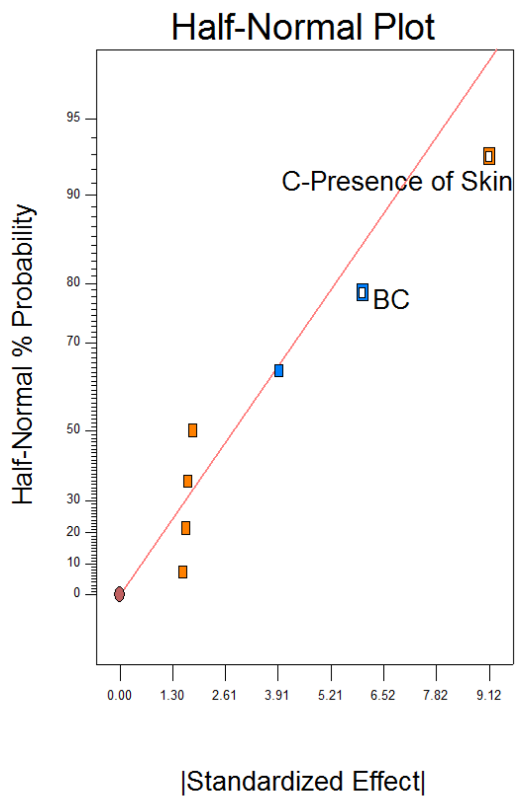


**Figure 4.2.2.** Half-Normal Plot for the response analysis of Front to Back ratio.

## 4.3 Rotman Lens

The results presented in this section are presented more as works in progress rather than finalized results. The results correspond to the lens with the more promising results however; no lens with satisfactory results was ever designed. Figure 4.3.1 shows the SIW implementation of the lens compared to the schematic outline.

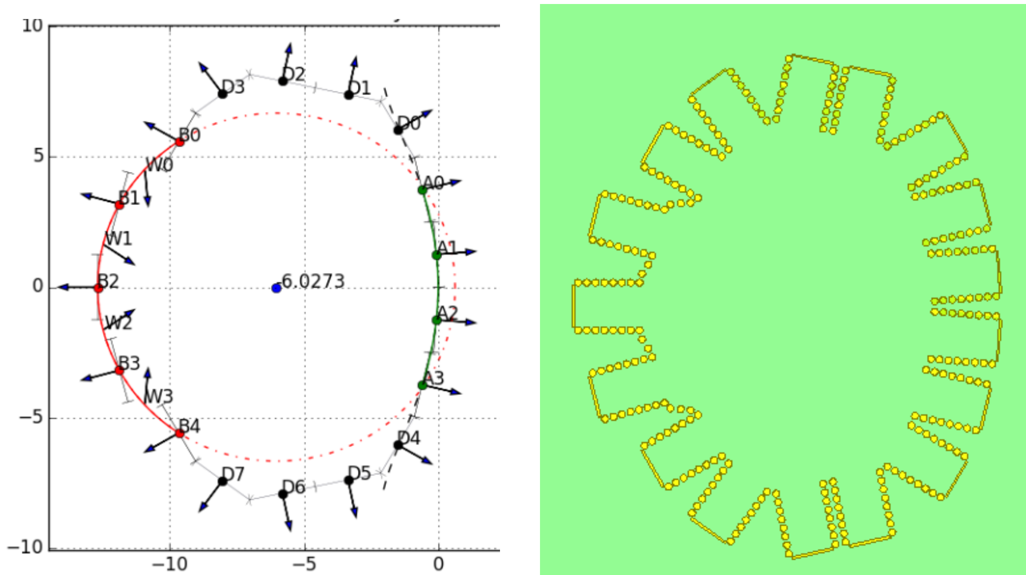

Fig. 4.3.1 Lens implemented with SIW

One of the dificulties was matching the ports throught the band of interest. No port is found below the -15dB threshold although at higher frequencies all ports match succesfully except B0 which is the port found furthest off-axis. The reflection coefficients can be seen in figure 4.3.2.

Figures 4.3.3 to 4.3.8 show the other difficulty in designing this lens. In terms of amplitude only the transmission coefficient for B2 is appropiately tapered throught the band of interest. In terms of phases, B2 and B1 achieve results close to their expected progressions. In the case of the phases for B2, seen in Fig 4.3.6, there is not much change is spacing and and there is no overlap.

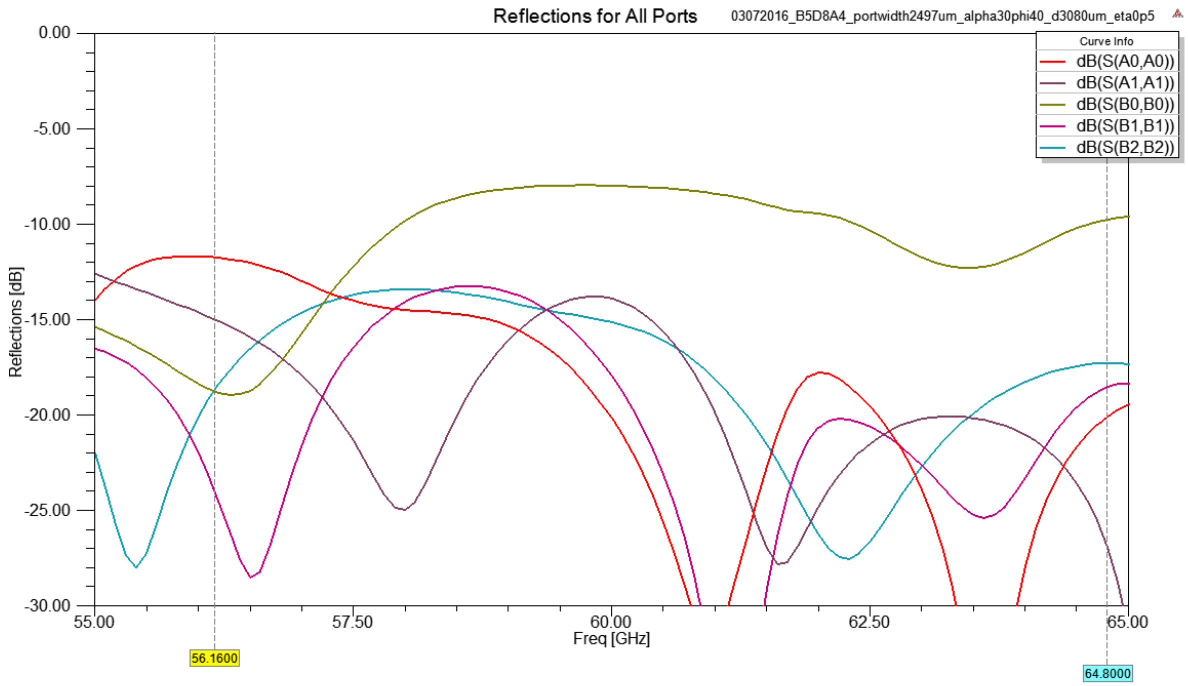


Fig. 4.3.2 Reflection coefficients for all ports.

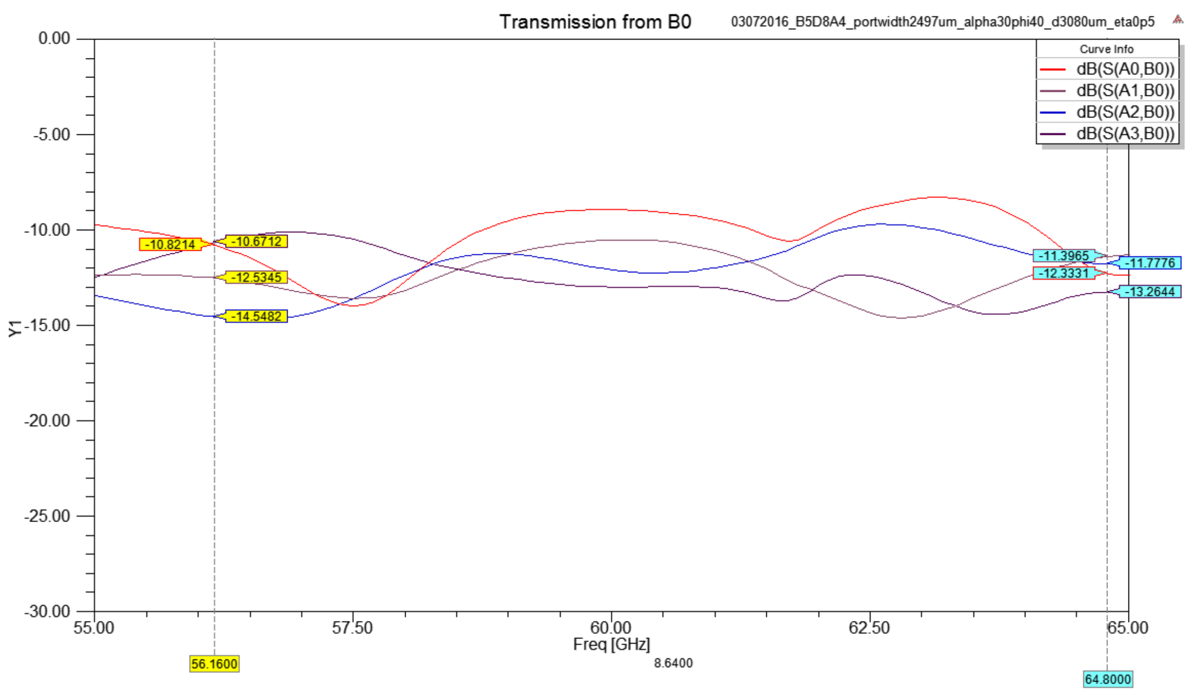


Fig. 4.3.3 Transmission from B0

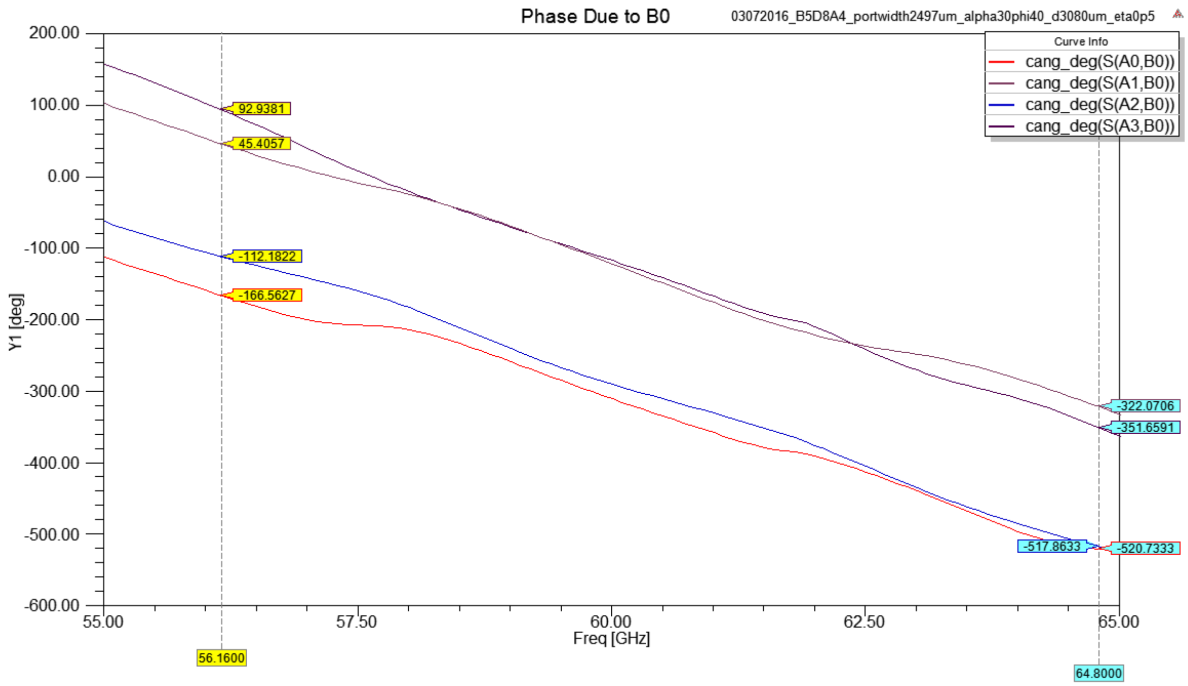


Fig. 4.3.4 Phases from B0

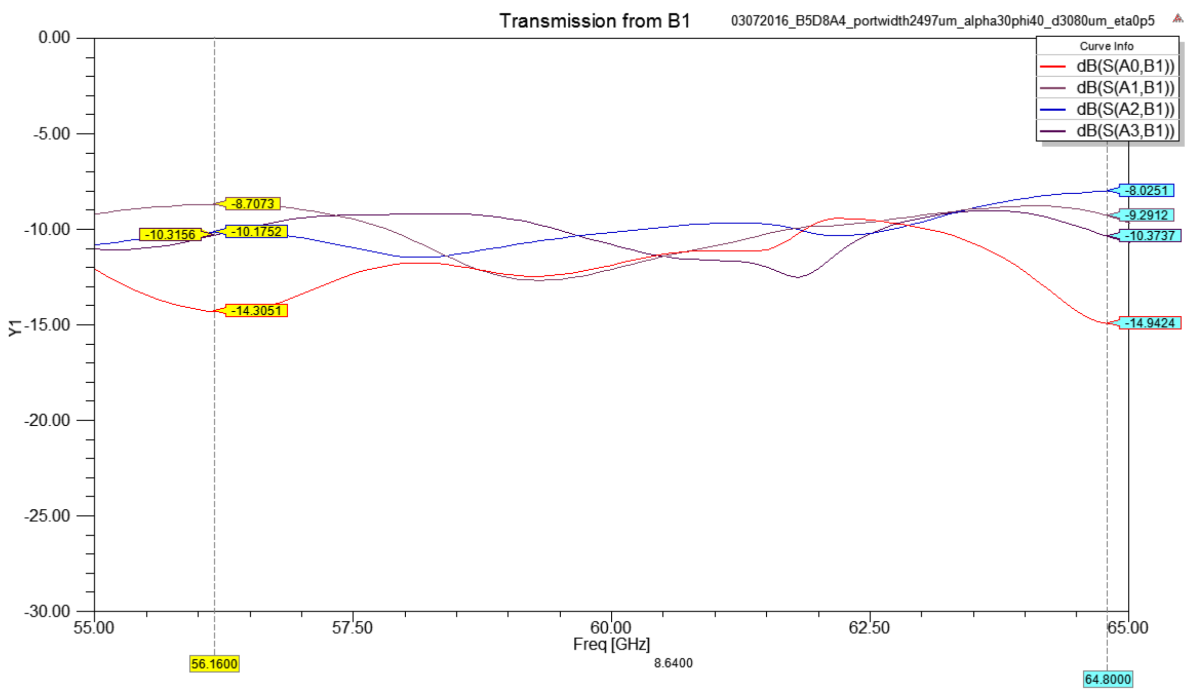


Fig. 4.3.5 Transmission from B1

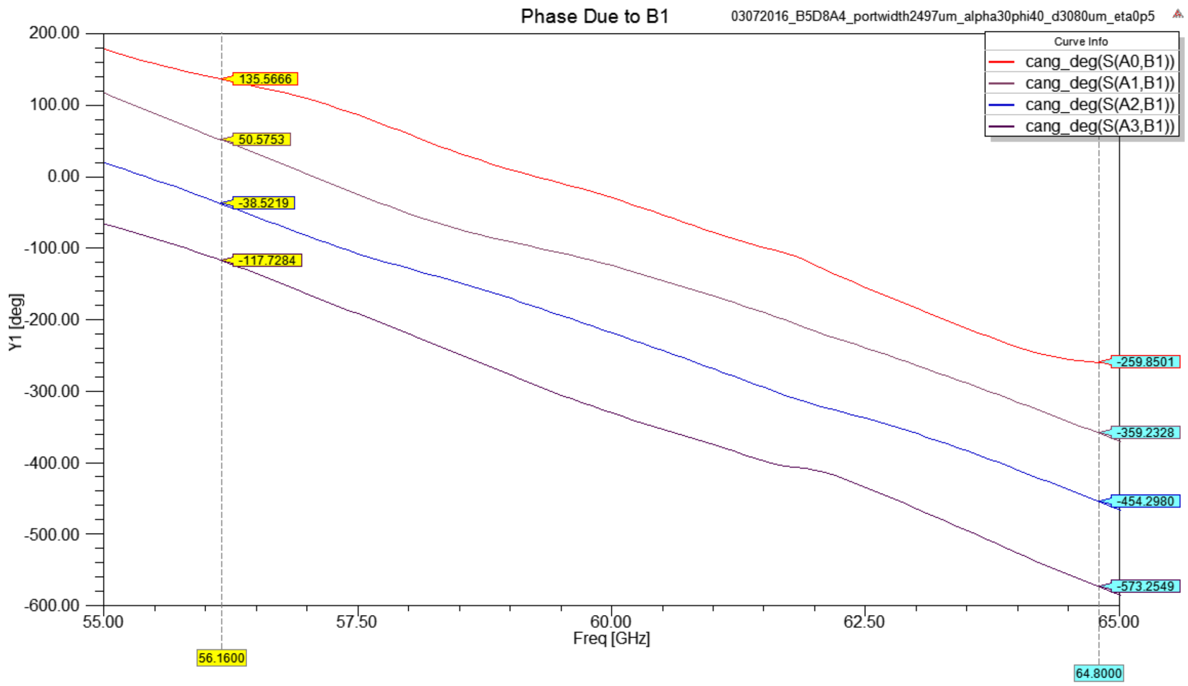


Fig. 4.3.6 Phases from B1

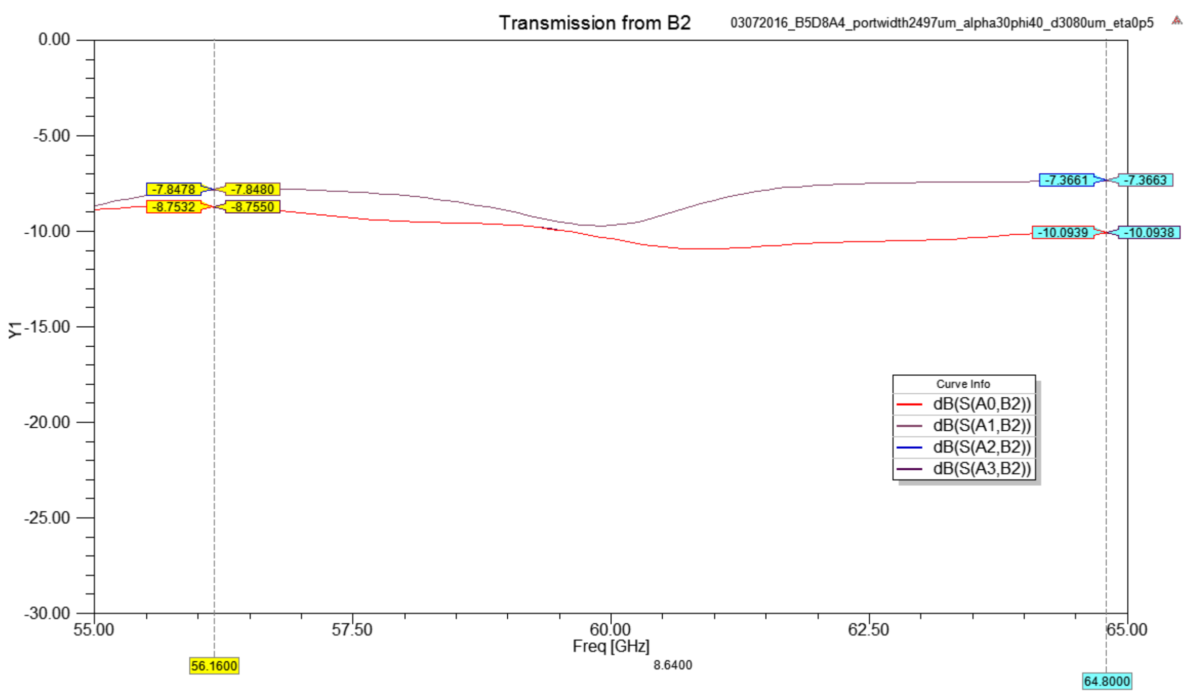


Fig. 4.3.7 Transmission from B2

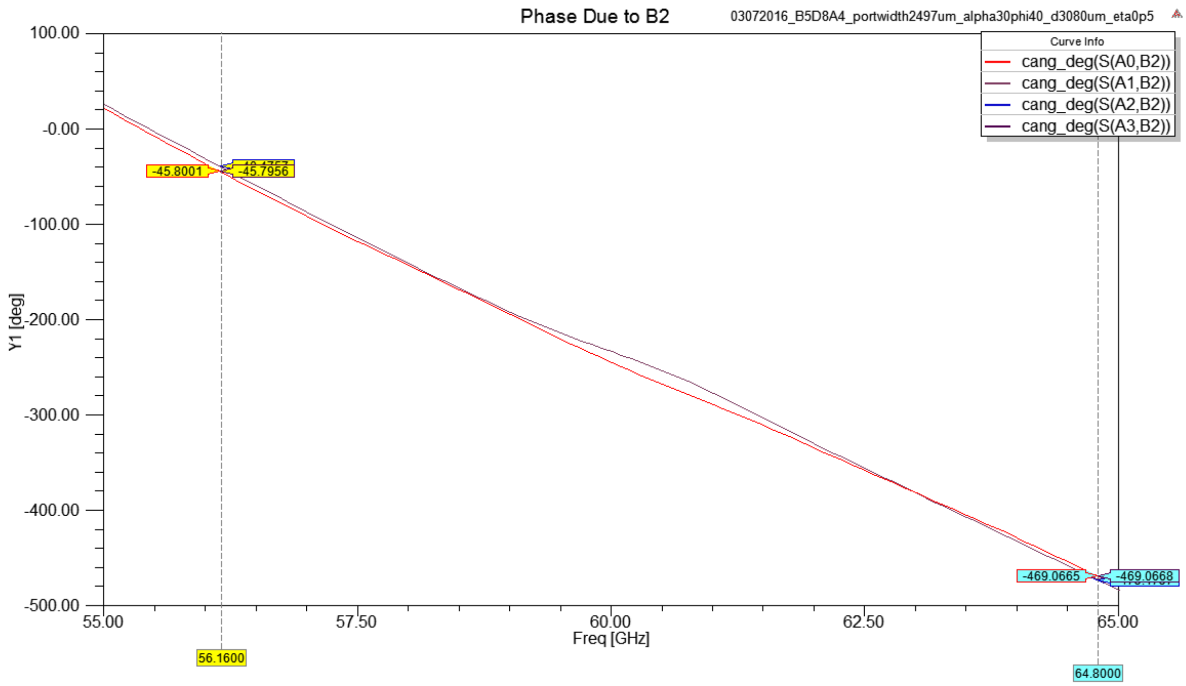


Fig. 4.3.8 Phases from B2

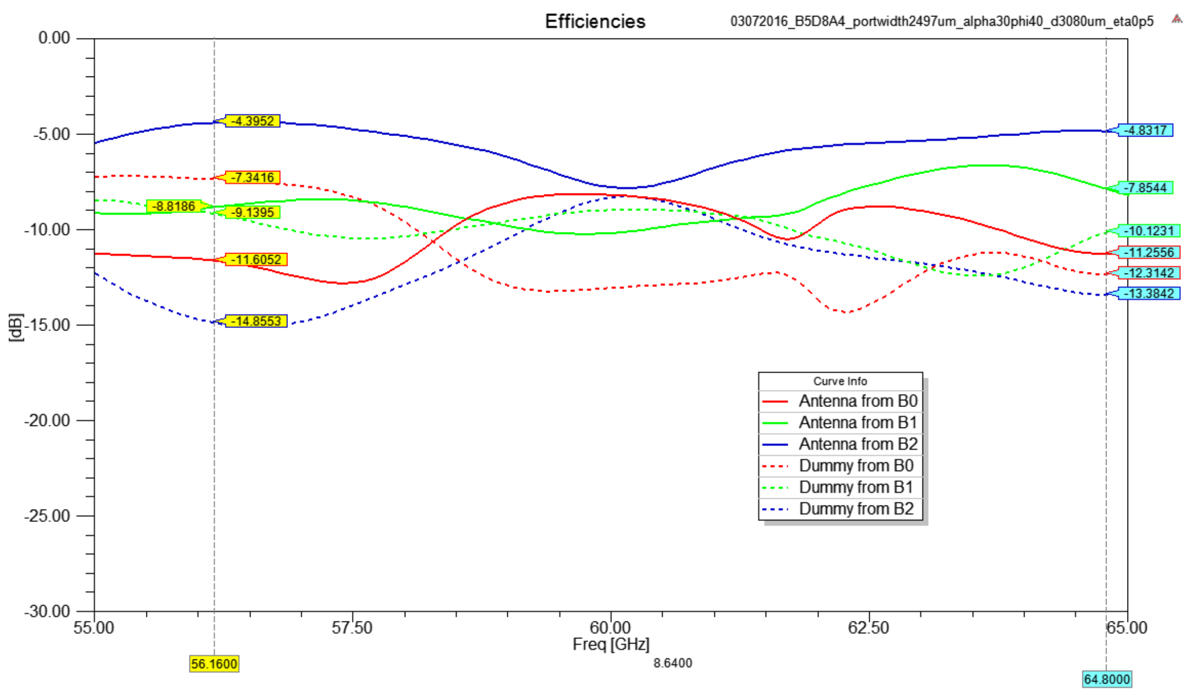


Fig. 4.3.9 Efficiencies for the Rotman Lens

Figure 4.3.9 shows the efficiencies for the lens. The highest efficiency it reaches comes from B2, achieving 36% efficiency.

# CHAPTER 5

# CONCLUSION

This work has shown the successful simulation of for two versions of an array for use in body centric wireless networks for off-body communications. The two versions of the array managed to meet the -10 dB bandwidth requirements and a beamwidth greater than 21° along the H-Plane, where the beam steering would occur. The array is also capable of successfully steering the main beam when fed with a progressive phase. Due to the lossy characteristics of the substrate, the Gain fell somewhat short of the 17 dBi goal but when compared to the plots of 3.1.1.1, the 15,51 and 14.54 dBi obtained at 56.16 still mean the antenna is good to be used for 60 and 50 meters respectively for each version of the array shown. The beam steering capabilities of the array where successfully demonstrated

In order to construct the arrays, Vertical T-Junctions were designed in order to allow designing corporate feeds, and coaxial-SIW transitions were designed for the bandwidth of interest. Future work may seek to formalize a parametric analysis on these two structures in order to develop more general design equations for other use cases.

A simple human body was developed in order to test the array's viability for use in BAN applications. The single radiating element and the H-Plane array using said radiating element demonstrated independence to the skin model in all parameters except for the FB ratio. This was an expected result. These results indicate that once fabricated, this antenna will perform without any problems when placed on the human body and used for off-body communications.

# References

[1] Pellegrini, A.; Brizzi, A.; Zhang, L.; Ali, K.; Hao, Y.; Wu, X.; Constantinou, C.C.; Nechayev, Y.; Hall, P.S.; Chahat, N.; Zhadobov, M.; Sauleau, R., "Antennas and Propagation for Body-Centric Wireless Communications at Millimeter-Wave Frequencies: A Review [Wireless Corner]," in *Antennas and Propagation Magazine, IEEE* , vol.55, no.4, pp.262-287, Aug. 2013

[2] M. Ahadobov, N. Chalhat, R. Sauleau, C. Le Quement and Y. Le Drean, “Millimeter-Wave Interactions with the Human Body: State of Knowledge and Recent Advances,” *International Journal of Microwave And Wireless Technologies,* **3,** 2, April 2011, pp. 237-247

[4] Chahat, N.; Zhadobov, M.; Le Coq, L.; Alekseev, S.I.; Sauleau, R., "Characterization of the Interactions Between a 60-GHz Antenna and the Human Body in an Off-Body Scenario," in *Antennas and Propagation, IEEE Transactions on* , vol.60, no.12, pp.5958-5965, Dec. 2012

[5] Kuo-Sheng Chin; Wen Jiang; Wenquan Che; Chih-Chun Chang; Huayan Jin, "Wideband LTCC 60-GHz Antenna Array With a Dual-Resonant Slot and Patch Structure," in *Antennas and Propagation, IEEE Transactions on* , vol.62, no.1, pp.174-182, Jan. 2014

[6] Yan Zhang; Zhi Ning Chen; Xianming Qing; Wei Hong, "Wideband Millimeter-Wave Substrate Integrated Waveguide Slotted Narrow-Wall Fed Cavity Antennas," in *Antennas and Propagation, IEEE Transactions on* , vol.59, no.5, pp.1488-1496, May 2011

[7] Yujian Li; Kwai-Man Luk, "Low-Cost High-Gain and Broadband Substrate- Integrated-Waveguide-Fed Patch Antenna Array for 60-GHz Band," in *Antennas and Propagation, IEEE Transactions on* , vol.62, no.11, pp.5531-5538, Nov. 2014

[8] Deslandes, D.; Ke Wu, "Accurate modeling, wave mechanisms, and design considerations of a substrate integrated waveguide," in *Microwave Theory and Techniques, IEEE Transactions on* , vol.54, no.6, pp.2516-2526, June 2006

[9] Ke Gong; Zhi Ning Chen; Xianming Qing; Peng Chen; Wei Hong, "Substrate Integrated Waveguide Cavity-Backed Wide Slot Antenna for 60-GHz Bands," in *Antennas and Propagation, IEEE Transactions on* , vol.60, no.12, pp.6023-6026, Dec. 2012

[10] Tian Yang Yang; Wei Hong; Yan Zhang, "Wideband Millimeter-Wave Substrate Integrated Waveguide Cavity-Backed Rectangular Patch Antenna," in *Antennas and Wireless Propagation Letters, IEEE* , vol.13, no., pp.205-208, 2014

[11] Antti E. I. Lamminen, Jussi Säily, and Antti R. Vimpari, “60-GHz Patch Antennas and Arrays on LTCC with Embedded-Cavity Substrates”, *IEEE Transactions On Antennas and Propagation, Vol. 56, NO.9,* September 2008

[12] Yue Li; Zhi Ning Chen; Xianming Qing; Zhijun Zhang; Junfeng Xu; Zhenghe Feng, "Axial Ratio Bandwidth Enhancement of 60-GHz Substrate Integrated Waveguide-Fed Circularly Polarized LTCC Antenna Array," in *Antennas and Propagation, IEEE Transactions on* , vol.60, no.10, pp.4619-4626, Oct. 2012

[13] Junfeng Xu; Zhi Ning Chen; Xianming Qing; Wei Hong, "Bandwidth Enhancement for a 60 GHz Substrate Integrated Waveguide Fed Cavity Array Antenna on LTCC," in *Antennas and Propagation, IEEE Transactions on* , vol.59, no.3, pp.826-832, March 2011

[14] Razavi, S.A.; Kildal, P.-S.; Liangliang Xiang; Alfonso Alos, E.; Haiguang Chen, "2 2-Slot Element for 60-GHz Planar Array Antenna Realized on Two Doubled-Sided PCBs Using SIW Cavity and EBG-Type Soft Surface fed by Microstrip-Ridge Gap Waveguide," in *Antennas and Propagation, IEEE Transactions on* , vol.62, no.9, pp.4564-4573, Sept. 2014

[15] Dong Gun Kam; Duixian Liu; Natarajan, A.; Reynolds, S.K.; Floyd, B.A., "Organic Packages With Embedded Phased-Array Antennas for 60-GHz Wireless Chipsets," in *Components, Packaging and Manufacturing Technology, IEEE Transactions on* , vol.1, no.11, pp.1806-1814, Nov. 2011

[16] Bing Zhang; Titz, D.; Ferrero, F.; Luxey, C.; Yue Ping Zhang, "Integration of Quadruple Linearly-Polarized Microstrip Grid Array Antennas for 60-GHz Antenna-in-Package Applications," in *Components, Packaging and Manufacturing Technology, IEEE Transactions on* , vol.3, no.8, pp.1293-1300, Aug. 2013

[17] Seki, T.; Honma, N.; Nishikawa, K.; Tsunekawa, K., "A 60-GHz multilayer parasitic microstrip array antenna on LTCC substrate for system-on-package," in *Microwave and Wireless Components Letters, IEEE* , vol.15, no.5, pp.339-341, May 2005

[18] Imbert, M.; Papio, A.; De Flaviis, F.; Jofre, L.; Romeu, J., "Design and Performance Evaluation of a Dielectric Flat Lens Antenna for Millimeter-Wave Applications," in *Antennas and Wireless Propagation Letters, IEEE* , vol.14, no., pp.342-345, 2015

[19] Rotman, W.; Turner, R., "Wide-angle microwave lens for line source applications," in *Antennas and Propagation, IEEE Transactions on* , vol.11, no.6, pp.623-632, Nov 1963

[20] In Sang Song; Jaeheung Kim; Dong Yun Jung; Ki Chan Eun; Jae Jin Lee; Seong Jun Cho; Hong Yi Kim; Jai-Hoon Bang; Inn-Yeal Oh; Chul Soon Park, "60GHz Rotman lens and new compact low loss delay line using LTCC technology," in *Radio and Wireless Symposium, 2009. RWS '09. IEEE* , vol., no., pp.663-666, 18-22 Jan. 2009

[21] Jastram, N.; Filipovic, D.S., "Design of a Wideband Millimeter Wave Micromachined Rotman Lens," in *Antennas and Propagation, IEEE Transactions on* , vol.63, no.6, pp.2790-2796, June 2015

[22] Yu Jian Cheng; Wei Hong; Ke Wu; Zhen Qi Kuai; Chen Yu; Ji Xin Chen; Zhou, J.Y.; Hong Jun Tang, "Substrate Integrated Waveguide (SIW) Rotman Lens and Its Ka-Band Multibeam Array Antenna Applications," in *Antennas and Propagation, IEEE Transactions on* , vol.56, no.8, pp.2504-2513, Aug. 2008

[23] Constantine A. Balanis, "*Antenna Theory: Analysis and Design"* 3rd Edition, Wiley 2012

[24] D. M. Pozar, "*Microwave Engineering*," 4th Edition, Wiley, 2012

[25] M. Bozzi, A. Georgiadis and K. Wu, "Review of substrate-integrated waveguide circuits and antennas," in *IET Microwaves, Antennas & Propagation*, vol. 5, no. 8, pp. 909-920, June 6 2011.

[26]'1.85mm Jack(Female) .375" Square Flange' Hasco, inc. http://www.hasco-inc.com/content/Southwest/1.85_Connectors/1812-02SF_CAD.pdf

[27] "RO4000® Series High Frequency Circuit Materials" Rogers Corporation. https://www.rogerscorp.com/documents/726/acs/RO4000-LaminatesData-sheet.pdf

[28] Constantine A. Balanis, "*Advanced Engineering Electromagnetic"s*, 2nd Edition, Wiley 2012.

[29] "An internet Resource for the Calculation of the Dielectric Properties of Body Tissues" Institute for Applied Physics, Italian National Research Council, http://niremf.ifac.cnr.it/tissprop/

[30] C.Gabriel, S.Gabriel and E.Corthout, "The dielectric properties of biological tissues: I. Literature survey", *Phys. Med. Biol*. 41 (1996), 2231-2249.

[31] S.Gabriel, R.W.Lau and C.Gabriel, "The dielectric properties of biological tissues: II. Measurements in the frequency range 10 Hz to 20 GHz", *Phys. Med. Biol*. 41 (1996), 2251-2269.

[32] S.Gabriel, R.W.Lau and C.Gabriel, "The dielectric properties of biological tissues: III. Parametric models for the dielectric spectrum of tissues", *Phys. Med. Biol.* 41 (1996), 2271-2293